

FLOW IMAGING USING MRI:
QUANTIFICATION AND ANALYSIS

A Dissertation

by

YUTTAPONG JIRARAKSOPAKUN

Submitted to the Office of Graduate Studies of
Texas A&M University
in partial fulfillment of the requirements for the degree of

DOCTOR OF PHILOSOPHY

May 2009

Major Subject: Electrical Engineering

FLOW IMAGING USING MRI:
QUANTIFICATION AND ANALYSIS

A Dissertation

by

YUTTAPONG JIRARAKSOPAKUN

Submitted to the Office of Graduate Studies of
Texas A&M University
in partial fulfillment of the requirements for the degree of

DOCTOR OF PHILOSOPHY

Approved by:

Chair of Committee,
Committee Members,

Head of Department,

Jim Ji
Andrew K. Chan
Deepa Kundur
Yoonsuck Choe
Mary P. McDougall
Costas N. Georghiades

May 2009

Major Subject: Electrical Engineering

ABSTRACT

Flow Imaging Using MRI: Quantification and Analysis. (May 2009)

Yuttapong Jiraraksopakun, B.E., Chulalongkorn University;

M.Eng., Texas A&M University

Chair of Advisory Committee: Dr. Jim Ji

A complex and challenging problem in flow study is to obtain quantitative flow information in opaque systems, for example, blood flow in biological systems and flow channels in chemical reactors. In this regard, MRI is superior to the conventional optical flow imaging or ultrasonic Doppler imaging. However, for high speed flows, complex flow behaviors and turbulences make it difficult to image and analyze the flows.

In MR flow imaging, MR tagging technique has demonstrated its ability to simultaneously visualize motion in a sequence of images. Moreover, a quantification method, namely HARMonic Phase (HARP) analysis, can extract a dense velocity field from tagged MR image sequence with minimal manual intervention. In this work, we developed and validated two new MRI methods for quantification of very rapid flows. First, HARP was integrated with a fast MRI imaging method called SEA (Single Echo Acquisition) to image and analyze high velocity flows. Second, an improved HARP method was developed to deal with tag fading and data noise in the raw MRI data. Specifically, a regularization method that incorporates the law of flow dynamics in the HARP analysis was developed. Finally, the methods were validated using results from

the computational fluid dynamics (CFD) and the conventional optimal flow imaging based on particle image velocimetry (PIV). The results demonstrated the improvement from the quantification using solely the conventional HARP method.

To My Family

ACKNOWLEDGEMENTS

I would like to thank to Dr. Jim Ji, the Chair of my Ph.D. committee, for serving and advising me throughout my Ph.D. study. I would like to thank to all my committee members – Dr. Andrew K. Chan, Dr. Deepa Kundur, Dr. Yoonsuck Choe, and Dr. Mary P. McDougall – who provided lots of useful comments and suggestions for my flow quantification research.

Besides my Ph.D. committee members, I would also like to thank to Dr. Steven M. Wright who involved and helped me on my MR flow experiments. I would like to thank to Dr. Debjyoti Banerjee who allowed me to initiate the PIV experiments in his flow laboratory and also provided useful and practical comments on the PIV and particle settings. Finally, I would like to thank to Dr. Victor M. Ugaz who also allowed me to collect a useful PIV data for my PIV study.

I would like to thank to all of my past and current research colleagues in the Magnetic Resonance System Laboratory (MRSL) – Ke Feng, John Bosshard, Gregory Whitehead, Yinan Liu, Jong Bum Son, Ching-Hua Chang, Chieh-Wei Chang, etc. – who provided good suggestions during the regular research meetings and even helped me fix research problems, especially Ke and John who helped me build the flow phantom for my research and spent their precious time helping me on the MR imaging experiments.

I would like to thank to all of my Thai friends and one Taiwanese, Fangling Tsai, who shared parts of their lives in College Station with me. Some provided help on my

research work, some provided delicious foods for me to survive from the junk foods, and some provided entertainment during the hard time of my study.

Last but not least, I would like to thank to my family and my alter ego, Pattama Wongsawan, who always supported and encouraged me throughout my graduate studies from my home country. Without all of you, this achievement would not have been fulfilled.

TABLE OF CONTENTS

	Page
ABSTRACT	iii
DEDICATION	v
ACKNOWLEDGEMENTS	vi
TABLE OF CONTENTS	viii
LIST OF FIGURES.....	x
LIST OF TABLES	xiii
CHAPTER	
I INTRODUCTION.....	1
A. Objectives and Rationale.....	1
B. Problem Statements	4
C. Contributions	4
II LITERATURE REVIEW.....	6
A. General Review on Flow Quantification.....	7
B. Flow Quantification by Magnetic Resonance Imaging	8
C. Flow Quantification by Optical Imaging.....	24
III MRI AND MR FLOW IMAGING	37
A. MRI Basic Principles.....	37
B. MR Image Formation	40
C. Fast MR Imaging.....	47
D. MR Flow Imaging	50
IV A FLOW QUANTIFICATION ANALYSIS USING SEA IMAGING	64
A. Rationale of the Work	64

CHAPTER		Page
	B. Methods	65
	C. Results	70
	D. Conclusion and Discussions	74
V	A FLUID REGULARIZATION METHOD FOR THE MR FLOW QUANTIFICATION.....	76
	A. Rationale of the Work	76
	B. Methods	77
	C. Results	94
	D. Conclusion and Discussions	117
VI	A VALIDATION OF THE HARP METHOD FOR THE MR FLOW QUANTIFICATION.....	119
	A. Rationale of the Work	119
	B. Methods	120
	C. Results	125
	D. Conclusion and Discussions	136
VII	CONCLUSIONS	138
	A. Future Research Directions	139
	REFERENCES.....	143
	VITA	186

LIST OF FIGURES

FIGURE	Page
1 An example of the MR data acquisition procedure and its associated pulse sequence	48
2 Imaging procedure for Single Echo Acquisition (SEA) MRI	50
3 An imaging pulse sequence for phase contrast MRI (PCMRI).....	55
4 A 1-1 SPAtial Modulation of Magnetization (SPAMM) pulse sequence.....	58
5 Example of a 1-1 SPAMM MR tagging image and its k-space data	58
6 The principle of HARP: harmonic phase is a material property	59
7 Summary of the HARP algorithm.....	63
8 A separate channel flow phantom used in the flow experiment with SEA imaging and a sample of MR tagging images from the phantom with the 64 channel SEA coil array located as a red box	67
9 A 2D tagging pulse sequence with a recalled gradient echo pulse used in the SEA imaging.....	68
10 The elliptic bandpass filter used in the HARP analysis	69
11 Velocity fields at different times in the tagged image sequence and the zoomed velocity field of (a) at (e) the outlet, (f) the inlet, and (g) the channel separation of the phantom indicated by the green boxes	72
12 The design of the flow phantom used in both the flow simulation and the real MR flow experiment.....	82
13 A sketch of flow experiment setups	83
14 A volume coil for the MR flow experiment.....	83
15 A 1-1 SPAMM tagging pulse sequence with a spin-echo data acquisition used in the flow experiment	85

FIGURE	Page
16 A flow chart of the Genetic Algorithm/ Evolutionary Programming (GA/EP).....	95
17 Simulated MR images using the 1-1 SPAMM tagging pulse with the velocity field obtained from the CFD simulation.....	98
18 The Fourier transform of the vertical tagging and horizontal tagging in Fig. 17	99
19 A ground truth velocity field from the CFD simulation.....	100
20 A velocity field from the HARP analysis from the tagging images in Fig. 17	100
21 A regularized velocity field from the velocity field in Fig. 20.....	100
22 A magnitude plot of the CFD velocity field in Fig. 19	104
23 A magnitude plot of the original HARP velocity field in Fig. 20.....	104
24 A magnitude plot of the regularized HARP velocity field in Fig. 21	104
25 A velocity field comparison at the separation channel among the CFD simulation, the original HARP, and the HARP-GA.	105
26 A velocity field comparison at the outlet among the CFD simulation, the original HARP, and the HARP-GA.....	106
27 A velocity field comparison at the inlet among the CFD simulation, the original HARP, and the HARP-GA.....	107
28 Two orthogonal tagging orientation images (1 average) acquired with 100 msec and 300 msec tag evolution delay	111
29 The velocity field and its magnitude plot from the original HARP analysis on the real MR data.....	112
30 The regularized velocity field and its magnitude plot from the original HARP analysis on the real MR data	113

FIGURE	Page
31 A velocity field comparison among the CFD simulation, the original HARP, and the regularized HARP.....	114
32 Magnitude plots of the velocity fields among the CFD simulation, the original HARP, and the regularized HARP.....	115
33 A flow phantom for PIV and MRI experiments.....	122
34 An example of a PIV image.	127
35 Extracted velocity fields from the correlation method (PIV) at the separation channel of the phantom	129
36 A velocity field and its magnitude plot on the original coordinates of the original HARP analysis	131
37 A velocity field comparison among CFD, PIV, and HARP.....	132
38 A velocity magnitude comparison among CFD, PIV, and HARP	133

LIST OF TABLES

TABLE		Page
1	The mean absolute error comparison between the original HARP and the regularized method	109
2	Affine transformation coefficients from the minimum square error optimization	130
3	The mean absolute error (MAE) from the PIV and HARP methods compared with the CFD as a ground truth	135

CHAPTER I

INTRODUCTION

A. Objectives and Rationale

This dissertation aims to develop, improve, and validate a flow analysis and quantification method with a regularization framework for magnetic resonance imaging (MRI). Specifically, it deals with the 2D complex flows acquired using high-speed MRI such as single-echo-acquisition (SEA) method. A previous work from SEA imaging was proven to be useful only for the qualitative study of flow using tagged MR images. No quantitative analysis has been performed because the results were only compared with visualization. Furthermore, no true ground truth has been achieved for validation. This motivated a research to implement, analyze, and validate a quantitative flow algorithm for SEA-MRI based on the tagged images.

A study of flows at high speeds in an opaque channel is complex and challenging. In fluid study, one of the most important dimensionless numbers that characterize a flow according to its speed and flowing channel geometry is called Reynolds number. The flows at a low Reynolds number are typically laminar and provide defined flow characteristics that can be used to aid a flow analysis. However, even a study of laminar flows in complicated channel geometry can be difficult and cause complex flow behaviors. Furthermore, those with a high Reynolds number introduce turbulence and

This dissertation follows the style of *IEEE Transactions on Medical Imaging*.

are even more difficult to be quantified inside the flow geometry. However, it is demanding for various industries to be able to study such a flow in the opaque system.

One common approach to quantify a flow is through optical imaging. This can be done by imaging the flow with features such as bubbles or dyeing particles that can move along with the flow of study. However, one of the main disadvantages of the optical imaging is that it requires an optically transparent cross-section of the settings being imaged. This can be impractical for some biological systems in which the flows occur in an opaque flow geometry. Furthermore, an introduction of bubbles or dyeing particles suspending in the flows might not be achievable in biological flow studies since it can be dangerous or harmful to such the biological systems. For this reason, MRI is a perfect tool to study these kinds of flows. It allows different subjects of interest to be imaged in an opaque media without extra features, hence easily overcome such those difficulties encountered in optical imaging.

One major drawback of the MRI is that it usually takes a long imaging time to complete data acquisition procedure for a single image. To be useful for a flow study, MRI requires a good imaging speed that can sufficiently capture the flow characteristics occurring within the duration of the study. Even though a cardiac motion can be considered as a type of periodic flows, flows are usually non-periodic and can be turbulent even at low Reynolds numbers providing the flow geometry is complex. Therefore, rapid imaging is always desired to completely record complex flow phenomena. This can also help reduce the complexity of the flow quantification even in high-speed flows when the imaging time between the snapshots is short enough.

Up to the current MRI development, an MR image can be acquired within a single shot by a total parallel imaging method named Single Echo Acquisition Magnetic Resonance Imaging (SEA-MRI) [1-3]. The technique greatly reduces imaging time, thus improving temporal resolution of an image dataset. SEA-MRI has demonstrated its ability to acquire an image with the frame rate up to 200 fps, which is much faster than the temporal resolution of a typical MRI that could be in minutes for one image. Therefore, the method offers an opportunity to capture transient response of a complex flow study as demonstrated in [4, 5]. Even though the conventional MR flow method based on phase contrast has been widely used for MR flow quantification, it has been demonstrated that the method is difficult to use for fluid flows in SEA imaging [5]. For this reason, MR tagging has been used and proved to be more useful to visualize flow pattern with SEA [4].

Not only does MR tagging provide clear flow visualization from its tag deformation, but it also opens a possibility to quantitatively analyze the flow field of the complex flows. The technique called HARmonic Phase (HARP) analysis [6-8] was proposed to extract a distribution of two-dimensional motion field from tagged images in a rapid fashion. In this thesis, HARP algorithm for two-dimensional flow quantification is then implemented to analyze fluid flows. To the best knowledge, HARP has been applied and validated only on the motion analysis of myocardium, which is assumingly periodic motion, whereas its analysis on non-periodic flows has never been performed. However, there is no periodicity assumption imposed on HARP analysis; therefore, it is justified to apply HARP on non-periodic flows like fluid flows in this study.

B. Problem Statements

The preliminary results from HARP show that it is a promising method to the complex flow study, even though there are issues to be addressed. Initially, HARP analysis obtains the motion field solely based on the image constraint (specifically phase invariance). This is not guaranteed that the flow field will be consistent with fluid dynamics theory. Also, other non-flow factors such as tag fading or noises in the MR data can degrade the HARP analysis. Therefore, a regularization method to improve HARP analysis is required. In addition, it is difficult to find the real ground truth to assure the results from the imaging method. For such reason, experimental validation is carried out by comparing with different quantitative flow methods. Therefore, it is required this thesis research: 1) to develop the fluid-dynamic regularized flow field extraction algorithm; 2) to validate the new method using the conventional optical imaging method.

C. Contributions

In this dissertation, two new MRI methods for quantification of very rapid flows has been developed and validated. First, HARP was integrated with a fast MRI imaging method called SEA to image and to analyze high velocity flows. Second, an improved HARP method was developed to deal with tag fading and data noise in the raw MRI data. Specifically, a regularization method that incorporates the law of fluid dynamics in the HARP analysis was developed. Finally, the methods were validated using results

from the computational fluid dynamics (CFD) and the conventional optimal flow imaging based on particle image velocimetry (PIV). The results demonstrated the improvement from the quantification using solely the conventional HARP method.

CHAPTER II

LITERATURE REVIEW

Flow quantification becomes a useful and important tool for growing numbers of biomedical applications. It can be used to non-invasively quantify blood flows and cardiac tissue motion, leading to the development of diagnostic tools for quantifying diseases or physiological flow modeling. For example, quantification of the left ventricle (LV) function during a cardiac motion cycle can determine healthy or ischemia subjects [9, 10]. Furthermore, its quantification derivatives, such as strain and ejection fraction (EF), can describe the global cardiac function [11], the effects from surgical procedures [12, 13] and the effects from drugs treatments [14]. Blood flow quantification can be used to characterize blood flows in coronary arteries from patients who had aortic valve replacements [15]. It can also be used to quantify stenotic flows in arteries where atherosclerosis can possibly develop [16]. Furthermore, the flow quantification potentially allows turbulent flow analysis [17], flow analysis in microfluidic lab-on-a-chip devices for mixing efficiency [18, 19], or an analysis of millisecond kinetics in chemical reactions [20].

Many existing methods to measure a flow have been reported (conferred to the flow measurement review [21]). Based on their different principles, they can quantify flows providing the suitability of their methodologies. In this review, flow quantification methods are categorized by a type of devices, such as acoustics, optics, MR, and mechanical devices. A general review of flow quantification for acoustic and mechanical

devices is firstly given. More emphasis on the quantification using optical imaging or MRI will be presented in details since the latter two are the imaging modalities related to this research.

A. General Review on Flow Quantification

One quick and simple way to measure a flow is to use a mechanical device or a flow meter. These devices are known as a venturi meter, an orifice plate, and a pitot tube. In principle, these devices have a specific geometry that causes differential pressure and use the differential pressure to measure the flow velocity of a fluid measured pressure by Bernoulli's principle. Quantifying flow with a mechanical device is easy relative to the other methods and provides the flow information directly from the real fluid. However, the flow quantification by this method is only one dimensional. That is, the device only measures a volumetric flow in one direction. Furthermore, it is very difficult to obtain dense measurements of a velocity field from a single mechanical device. Its extension to measure two or three-dimensional flow is simply a use of more devices to measure the flow in different directions that provides only sparse data of the whole area or volume of interest.

Flows can also be measured non-intrusively by acoustic signals. The method is generally called Doppler Ultrasound; and devices that measure velocities in a fluid flow with the acoustic signals are Acoustic Doppler Velocimeter (ADV) and Laser Doppler Velocimeter (LDV). Basically, they utilize the Doppler phenomena to quantify a flow

velocity. An acoustic or light beam is emitted from a transducer and incident on particles moving with the flow. A reflected beam is measured for its shift in wavelengths, which is related to the velocity in the same direction of the beam. Doppler ultrasound can be extended to two and three-dimension, which is referred to the vector Doppler technique. The technique combines Doppler frequencies from two independent beam directions [22-25] or three directions [26] for measuring multiple velocity components for a planar flow or a true velocity respectively. The vector Doppler technique can be used together with the color flow imaging to quantitatively visualize a flow by Ultrasound. Applications of flow quantification using Doppler Ultrasound can be found in blood flow measurement and tissue motion in medical imaging or flow measurement in fluids [27-29].

B. Flow Quantification by Magnetic Resonance Imaging

Estimating motion using Magnetic Resonance Imaging (MRI) is motivated from two major purposes: the quantitative measurement of blood flow and the analysis of heart and other tissue motion since MRI is an ideal imaging modality to these biomedical researches [30]. In addition, motion estimation using MRI is useful for MR elastography imaging [31] and MR diffusion imaging [32]. MR signals are complex quantities generated from magnetization, and the phase of the magnetization can infer to displacement or velocity information. Therefore, flow-MRI techniques quantify motion from manipulating phase of the MR signals such as displacement encoding, velocity

encoding, or magnetization saturation to produce temporary magnetic tags. This can be referred to as the magnetic resonance velocimetry (MRV).

The following review will be focus to specific MR techniques that have been used for biomedical studies. These techniques are mainly categorized as phase contrast MRI (PC-MRI), tagged MRI (tMRI), harmonic phase imaging (HARP), and displacement encoding with stimulated echo (DENSE). Among these imaging techniques, DENSE is a relatively new technique that shares its similarity to both PC-MRI and HARP. Therefore, the organization of the MRV review will be grouped into three major methods: PC-MRI, tagged MRI (and HARP), and DENSE. For extensive details of these techniques, interested readers on MRV for fluid motion or tissue motion are also referred to [30, 33-35].

Tagged Magnetic Resonance Imaging

Tagged magnetic resonance imaging (tMRI) was originally motivated from a measurement of the cardiac motion. It produces an MR image with a spatially periodic modulation pattern of magnetization, or so called magnetic tags. The tag pattern is created within and move along with the tissues when imaged, hence reflecting the motion of underlying tissues. This method can be achieved by application of a spatially selective excitation technique before a normal MR imaging pulse sequence. This tagging presaturation essentially excites multiple planes of magnetization by the combination of RF pulses and gradients. Different tagging approaches have been proposed initially to assess the motion of a human heart [36-40]. Two most common tagging procedures that

provide regularly spaced parallel grids are obtained using the frequency selective DANTE RF pulse [36, 37, 41] or the SPATial Modulation of Magnetization (SPAMM) tagging procedure [38-40].

The DANTE pulse scheme comprises a train of short RF pulses with simultaneous application of spatial gradients, which can be mathematically modeled as

$$f_{DANTE}(t) = m(t)(\delta_{\Delta t} * p)(t)$$

where $\delta_{\Delta t} = \sum_{n=-\infty}^{\infty} \delta(t - n\Delta t)$ denotes the comb function of RF pulses, $p(t)$ is the shape of a single RF pulse and $m(t)$ is the amplitude envelope of the comb [30]. From the Fourier theory, the shape and the width of the tags is determined by $m(t)$ and its support. The support of $p(t)$ is limited to be shorter than the comb spacing Δt . Therefore, the comb of RF pulses produces a comb of Fourier spectrum with spacing $\Delta f_{RFcomb} = 1/\Delta t$ of which the amplitude of the comb is weighted by the Fourier transform of $p(t)$ (cf. to [42]). Hence, the frequency selective RF pulses $(\delta_{\Delta t} * p)(t)$ and the spatial gradients can be used to control the tag spacing. Tagging using relatively short, high-amplitude RF pulses is suitable for small imaging systems, however the method is limited for large, or whole body systems.

Consequently, the modification for the whole body system leads to a new tagging procedure based on binomial, non-selective RF pulses [39], which can avoid excessive modulation from short RF pulses. In this tagging procedure, the tagging gradient is

quickly turned on and off (blipped) between each successive RF pulse in the comb; the reciprocal of the time integral of each blip determines the tagging spacing. A two-dimensional tagging grid can be produced by following the first SPAMM with the second RF pulse set, also with the gradient blips in a different spatial orientation than the first gradient blips. Effective composite flip angle of 90° phase shift for the two RF pulse sequences can be utilized to avoid the artifacts produced from stimulated echoes [39]. An optional spoiler gradient can be used in a direction orthogonal to the tags to dephase the remaining transverse magnetization that is undesired for the subsequent imaging pulse.

The tags produced from these conventional methods have a serious problem of tag degradation due to longitudinal (T_1) relaxation. Even though the longitudinal relaxation of myocardium is long enough to potentially preserve the tag contrast throughout a cardiac cycle, this tag fading is further speeded up by a function of a flip angle from each successive imaging pulse sequence TR. Furthermore, the signal at untagged locations is re-grown from longitudinal relaxation, hence complicating the detection of the tags. For this reason, the complementary SPAMM (CSPAMM) was motivated to improve the tag contrast and to reliably identify the tags for motion assessment [43]. Two measurements of conventional two-dimensional 1-1 SPAMM are used to produce a positive and negative tagging grid. The negative tagging grid can be obtained by phase inversion of one of the four RF pulses in the conventional two-dimensional SPAMM. Subtraction of these two tagged images yields the magnetization component with only tagging information.

In addition, the method is able to provide the ‘gratis’ anatomical image, free of tags, that is useful to determine the boundary of the tissues in motion, e.g. epicardium or endocardium [43]. A scheme of ramped imaging flip angles tuned to the longitudinal relaxation of the tissue was also used with CSPAMM to provide a constant tag contrast throughout the cardiac cycle [44]. However, the short RF pulse in the tagging sequence excites a fixed image slice; and therefore the tagged image acquired at different time might not represent the same image slice. Slice following CSPAMM (SF-CSPAMM) was proposed to track true motion from tMRI by only tagging the desired image slice using slice selective RF pulse [45]. Furthermore, a new reconstruction method based on magnitude image CSPAMM (MICSR) was used to improve contrast and tag persistence. The method helps get rid of handling the complex data because only the magnitude images are used to produce a final tagged image. The tags from MICSR still preserve zero mean, sinusoidal profiles that can be used for HARP processing [46]. Recently, CSPAMM has been demonstrated its feasibility to be employed in a clinical system [47]. A measurement of tag deformation provides a motion component in the direction of the tag orientation. In order to obtain a two-dimensional or full three-dimensional tracking of a point through time, measurement from different tagging orientation sets are required to be combined and interpolated in both space and time. The classical motion analysis of tMRI is performed in an image registration framework. The tags from tMRI provide a unique feature for a feature-based matching. A matching algorithm usually contains three major steps: interactive or semi-automatic segmentation of tissue in motion [48-50]; identification of tag points and its orientation [49]; and motion fitting by three (or

two for two-dimensional motion analysis) orthogonal one-dimensional displacement from all tag detected points [51]. Most of these motion analyses has been developed extensively to visualize or to assess cardiac motion.

In analysis of heart motion, the myocardial contours at left ventricle (LV) are detected and tag lines are tracked using different approaches [49, 50, 52-56], e.g. pattern matching, snakes, spline modeling, and finite element-based modeling. Most of these methods differ mainly because of the underlying deformation models utilized for the analysis. Some of them are based on the LV geometry and a specific coordinate system, such as prolate spheroidal [57] or planispheric coordinates [58]. On the other hand, the other techniques approximate the LV using finite element models to generate a continuous deformation, e.g. volumic superquadric with parametric offsets [59], volumic deformable superquadric [60], and 16-element cubic polynomials [55]. The other completely different method determines the LV deformation by decomposing the myocardial wall into a finely spaced mesh and reconstructing a displacement field via finite difference analysis and a smoothness constraint, so called the discrete model free algorithm (DMF) [61, 62]. The method is used to provide unsupervised 3D strain reconstruction of the LV [63].

With various choices of deformation models, an interpolation scheme has to be defined for computation of spatial derivatives. The interpolation is needed mainly due to the sparsity of information of the tag pattern. For example, cosine series was used for the fitting in the spatio-temporal displacement field model [64]. Legendre polynomials was used to determine the displacement filed in the prolate spheroidal coordinate-based

model for tag strain (E) analysis (TEA) [57]. B-spline-based methods have also been widely employed to describe the deformed tag due to the attractive properties of the B-spline function [65]. The B-spline-based motion analysis of the LV from tMRI are such as tagged tissue tracker [66] and four-D tag strain (E) analysis (FTEA) [58, 67]. In addition, the detailed comparison of TEA, DMF, TTT, and FTEA for tMRI was quantified and concluded that all of these methods can characterize myocardial function with great precision; the choice of a model depends on the application requirements for noise sensitivity and spatial resolution [56].

Upon cardiac motion analysis, tMRI also demonstrates the usefulness for both quantitative [68] and qualitative bulk flow measurement [34, 35], which can also be referred as time-of-flight (TOF) techniques. In the early era of flow visualization, TOF techniques employ a pre-saturation (or a tag) on an imaging slice and image unsaturated spins flowing into the slice. These techniques together with flow compensation or background suppression are applied for MR angiography (MRA) to enhance flow contrast for improved image quality [35, 69]. Later, two-dimensional spin tagging is also utilized to provide evolution of flow patterns for flows. This is useful to studies of turbulent flows or flows in complex geometries [4, 68] in which an instantaneous two-dimensional motion information is necessary to be observed simultaneously.

In flow quantification, velocity information is computed from the mean displacement of tag deformation between the tagging and imaging time [70]. This Eulerian measurement of tag displacement was reported with inaccuracies due to higher-order motions, and therefore can be improved by the first-order (acceleration) correction [70].

An automatic method based on the image brightness optical flow computation by [71] was also utilized to provide a to extract displacement fields from tag deformation [72]. Flow quantification using spin-tagging MRI has demonstrated its advantage over that using the phase contrast MRI, which is more sensitive to magnetic susceptibility gradients, higher-order motion terms, and limited dynamic range [72]. In addition, magnitude tagging can be used to measure the motion and velocity spectra of a flow, which can be used to remove the signal from static tissues and improve the blood-displacement measurement [73].

Another promising quantitative tool for tMRI is based on the phase of the complex tagged image in k-space. The technique, so called HARmonic Phase (HARP) imaging, has been developed to rapidly derive the tag displacement information from SPAMM-tagged images. It has demonstrated the potential of real-time, minimal manual intervention processing for monitoring cardiac function [6, 7, 74, 75], or measuring tissue motion [76]. In HARP method, a tagged image is produced from the 1-1 SPAMM pulse sequence. The image consists of several spectral peaks in k-space due to its sinusoidal tag profile. The motion information in a specific orientation is computed from one of the noncentral spectral peaks. In HARP algorithm, a spectral peak is band-pass filtered from its original data and is inversed Fourier transform. The phase contours of the complex image (a HARP image) deform in the same manner as the tag pattern, which also tracks the underlying tissue motion. Hence, phase difference between two consecutive HARP images contains the displacement information during the time of which the two images are acquired.

With the technique, the left ventricle can be automatically segmented; tag lines can be quickly detected; cardiac in-plane motion and strain rate can be rapidly quantified from MR tagged images. However, in cardiac motion the tag lines might not be completed due to their disappearance or re-appearance throughout the cardiac cycle. The HARP technique originally cannot address this issue, which can lead to systematic errors in strain results [9]. This coverage of myocardium problem can be improved by extended HARP tracking proposed by [77].

Since the HARP algorithm do not have to work on a full k-space domain to derive the displacement field, the fast acquisition method for HARP has been proposed to only acquire the small region of k-space data rather than acquiring the full k-space data [78, 79]. The method is called the fastHARP technique and essentially employs the stimulated echo pulse field gradient approach similarly to displacement encoding with stimulated echoes (DENSE) [80]. This is achieved by applying an offset gradient to center the acquisition on the tagging spectral peak. Echo planar imaging (EPI) pulse sequence is used to speed up the acquisition within a single shot. FastHARP and region-of-interest reconstruction enables real time continuous monitoring of cardiac strain for the early detection and quantification of ischemia during MR stress tests [81]. However, multiple spectral peaks can also be combined to eliminate phase errors in HARP due to the field inhomogeneity. This peak combination method helps HARP improve the reproducibility of motion parameters [82].

Three-dimensional HARP for motion analysis can be extended based on three-dimensional tagging MRI (3D-tMRI). Three-dimensional tagging using CSPAMM (3D-

CSPAMM) has been proposed to produce a true 3D-CSPAMM tagged dataset; and extraction of three spectral peaks in 3D k-space allows point tracking throughout the volume of interest by HARP [83]. An FEM approach to track the sparse collection of points within the LV wall based on HARP was later proposed [84-86]. In the FEM approach, the points within the LV wall deform based on phase invariance condition of HARP to guarantee the proper deformation [85]. Automatic 3D tracking of the points at the intersections between the short-axis (SA) and the long-axis (LA) planes are later proposed [87].

Furthermore, it was shown that HARP can be extended to measure longitudinal strain even from only short-axis images [8]. Later, a tagging method has been proposed to encode and to automatically track both in-plane and through-plane displacements in three dimensions from a single image plane using a modified SF-CSPAMM [88]. Based on thin slice thickness and phase invariance conditions, the method (zHARP) can directly track the three-dimensional displacement of every point within the image plane throughout an entire image sequence with no increase in imaging time [88]. This has its advantage over the three-dimensional tracking in [85, 87] since the collection of points from 3D dataset is usually sparse; and only the intersection points between the two orthogonal planes (SA and LA planes in cardiac tagged images) provide the true 3D displacement.

Phase Contrast Magnetic Resonance Imaging

Phase Contrast Magnetic Resonance Imaging (PC-MRI) is a method to quantify the motion, specifically the velocity, based on the sensitivity of the phase of the MR signal. The technique provides pixel-by-pixel velocity value of the underlying tissue. It has been used initially for blood flow measurements in medical imaging, and has been expanded to study flows in other disciplines such as gas flows, turbulence and diffusion in stenosis vessels or complex geometries, and multiphase flows. Also, it can be extended to derive displacement field for strain measurements of the myocardium as with the same case of tMRI. This can be achieved through an integration of velocity maps over an imaging time interval, which can lead to motion tracking or velocity-based trajectory computation using PC-MRI [89, 90]. However, the displacement field from PC-MRI is sensitive to an offset in the velocity data and prone to errors from gradient imperfections.

In PC-MRI, bipolar gradients are used to produce velocity-induced phase shift for the MR signal. Bipolar velocity encoding gradients impart phase shifts to moving protons, but not to stationary protons. Two measurements with two different velocity encoding gradients but otherwise identical acquisition parameters allow motion encoding of flow in one direction. With the velocity constant assumption during the acquisitions, phase subtraction of the two measurement images therefore yields a velocity map at each volume pixel. A design of the PC-MRI pulse sequence usually prescribes the velocity sensitivity (or v_{enc}) along with an imaging pulse sequence, e.g. the gradient echo or spin echo pulse sequences. The velocity sensitivity is the maximum velocity that produces a phase shift of π radians. This parameter is important, for it defines the range of velocities

that can be uniquely identified in the phase map to avoid velocity aliasing, i.e. the velocities of which their phase values range from $-\pi$ to π radians. It also determines the profile of the encoding bipolar gradient, e.g. gradient strength and its duration. In practice pulse sequence, the velocity sensitivity can be prescribed by the velocity slightly larger from the largest velocities under study. However, it can be variable in order to tailor to different maximum velocities of the flows that vary significantly at each phase of the motion [91]. The mathematics of this motion encoding technique will be presented in the background section.

One of advantages of PC-MRI over tMRI is that it can be intuitively extended to higher dimension imaging for real flows. That is, three-dimensional flow data can be easily acquired from PC-MRI by repeating the imaging pulse sequence with a flow encoding gradient in each direction. Since a velocity map is obtained by subtraction, there are at least three measurements required for a two-dimensional dataset, and four measurements for a three-dimensional dataset [92]. In the other words, a non-flow-encoding measurement is required for the subtraction to each direction of the flow encoding measurements in 2D and 3D PC-MRI. A reference scan might be also acquired to get rid of the phase offsets due to many other processes such as the magnetic field inhomogeneity, pulse sequence tuning, RF coil phase, and motion in directions other than the one of interest [93].

PC-MRI finds its applications in various areas [33]. In physiologic blood flow, three-dimensional PC-MRI data that is acquired with a trigger signal such as the ECG signal provides the time-resolved three-dimensional PC-MRI, i.e. four-dimensional flow

imaging. Data at different flow encoding directions can be interleaved during acquisition and re-arranged for a complete dataset of all motion phase within a cardiac cycle. The temporal resolution of the image data depends on the repetition time of the pulse sequence and the interleaving procedure [94, 95], but can also be improved by combination with parallel imaging [96]. The technique is also called “cine” PC-MRI and can be used to quantify many types of blood flows: arterial and venous blood flow [97], pulmonary blood flows [98, 99], renal blood flows [100, 101], flows in cerebral blood vessels [102-104], cardiovascular flows [105-108], and portal flows [109, 110]. A velocity map of vascular blood flows from PC-MRI demonstrates the potential of clinical blood flow quantification for preoperative diagnosis, planning, and postoperative monitoring for vascular diseases [111].

In flow-in-geometry measurements, PC-MRI can be utilized to measure mean velocities of laminar and turbulent steady flows. Most of the early PC-MRI flow studies were conducted by measuring a pipe flow with turbulence [112] or various types of stenosis, i.e. flows in a partially obstructed channel [17, 70, 113]. Later, it is exploited its capabilities to capture full three-dimensional velocity fields of high Reynolds number flows in highly complicated geometries [114-116]. PC-MRI can provide detailed measurements up to approximately 1 mm resolution [114] that possibly allows a point-by-point validation of their results with a data from laser Doppler anemometry (LDA), tMRI, PIV, or computational fluid dynamics (CFD) [70, 114, 117-119]. However, it is challenging for PC-MRI to acquire real instantaneous MR velocity measurements in turbulent flows due to the limitation of imaging pulse sequence duration. To address this,

ultrafast imaging pulse sequences have been proposed to allow PC-MRI to visualize and to quantify the nearly instantaneous velocity fields, possibly within 5 – 50 ms for a two-dimensional image [120-127]. They are also useful to efficiently quantify turbulent effects, such as diffusion coefficient and velocity variance, during image acquisition [128, 129].

PC-MRI is also well suited to multiphase flow studies, flows with different chemical constituents and state properties, because it exploits the ability to separate the combination of signals from solids, liquids, and gases in the flows. A number of MR experiments on the multiphase flows include studies of the sedimentation of solid particles in liquids [130], water-oil emulsion [131] or liquid mixtures [132], flow of gas-liquid combinations [133], and three phase solid-liquid-gas flows in chemical and bio reactors [134]. More complete reviews on MRI multiphase flows are referred to [34, 135].

Displacement Encoding with Stimulated Echoes

Recently, an idea to combine the advantages of both tMRI and PC-MRI yields a method that measures large displacements over a long period while maintaining high spatial resolution [136]. The method was motivated from the framework of magnetic resonance elastography of which the spin phase in a stimulated echo imaging experiment exhibits the modulation according to the position rather than the velocity [137]. The motion encoding scheme employs a pair of pulsed field gradients (PFGs) that provide a direct measurement of displacements. Two PFGs are usually with the same profile, but

logically opposite in the amplitude sign. Since each PFG encodes the spin position, the net phase accumulation at the acquisition is the displacement during the time evolution between the two PFGs.

PC-MRI can be also considered as a PFG mechanism in which the uniform velocity during the encoding time is assumed [30, 138]. Therefore, displacement encoding sequence design issues on phase ambiguity from aliasing or spurious phases from additional sources also need to be avoided similarly in PC-MRI. Even though a bipolar encoding pulse sequence has been widely used PC-MRI, it is not well-suited to encode displacements over a long period of time. In displacement encoding, it is desired to encode the displacement on the magnetization and store the magnetization along the static magnetic field direction to reduce the effect of T_2^* signal decay. To achieve this, the pulse gradient stimulated echo sequence is employed to allow motion encoding over a time order of T_1 [139]. This hence leads to a displacement encoding technique with the use of a stimulated echo acquisition mode (STEAM).

Therefore, a family of displacement encoding with stimulated echo (DENSE) methods has been proposed for highly sensitive motion-encoding schemes [136, 140-142]. The original proposal provides an implementation of the pulse sequence with the respiratory triggering for three-dimensional displacement encoding by four-point measurements. Subsequently, a multi-shot segmented k-space EPI was employed with DENSE for an efficient sampling scheme. The method, called fast-DENSE, is able to collect a single slice of two-dimensional data in 24 heartbeats within one breath-hold [140]. At the present, DENSE has been found most of its applications on cardiac motion

analysis [143-145], but it can be applied to track the motion of brain and spinal cord as well [146]. As a comparison to HARP for cardiac motion analysis, the method provides strain measurements at high precision and higher resolution for monitoring the cardiac function [140].

Even though DENSE and HARP arose from different frameworks and are regarded as different MR techniques, they have demonstrated many similarities. The pulse sequences of spin tagging (SPAMM) and DENSE are very similar. A decoding gradient is placed before the readout in DENSE while there is no explicit decoding gradient in HARP. Only imaging gradient at the readout is used in HARP and is referred as a decoding gradient. However, it can be subsequently realized that the two pulse sequences are actually identical especially for fastHARP and DENSE [80] since a “decoding” gradient is also used before the readout in order to only sampling the tagging peak in fastHARP.

Furthermore, the distribution of the signals over k-space in DENSE acquisition demonstrates the similarity to that of HARP. It comprises three spectral peaks: the stimulated echo signal (STE), the free induction decay (FID), and the stimulated anti-echo (STAE). These are in fact identical to the spectral peaks of SPAMM-HARP with a shift of its k-space center. Therefore, suppression of unwanted signals of these two methods can be performed in different approaches [80, 141, 147]. In DENSE, an optimization method called meta-DENSE suppresses the FID signal out of the sampling window of the acquired data by using an inversion pulse [141]. In HARP, this is done by simply applying a band-pass filter as a post-processing step. Hence, there is no

fundamental difference between these two techniques on their data generation aspect [80]. Only practical implementations for their acquisition and reconstruction are different.

C. Flow Quantification by Optical Imaging

Optical imaging measurement does not directly measure velocity of a flow. It involves imaging a moving target or flow and post-processing those images to obtain its velocity information. One key device is therefore the imaging unit like a CCD camera. To enable a flow study, the camera needs to adequately capture transient characteristics of a flow. Even though flow quantification from images is essentially a two dimensional problem, one dimensional flows can also be quantified from this method. It is a special case of two dimensional flow problems. In this review, optics flow methods are presented into two main techniques: Optical Flow (OF) and Particle Image Velocimetry (PIV). Briefly, the former analyzes the flow in an image sequence by imposing a consistency assumption among the images whereas the latter analyzes the particle motion that is assumed to well represent the flow in which the particles are suspended. In fact, PIV is considered as one of optical flow methods. It is presented as a separated review since it will be served as the optical flow method used in this research.

Optical Flow

The optical flow is a method to produce a dense displacement field between from a sequence of images. The displacement field or velocity field produced from this method is interchangeably called as the optical flow field. The optical flow method is usually based on a hypothesis that the brightness of a moving target in the image sequence is invariant. In practice, the assumption is hardly achievable and is relaxed to be approximately constant under motion for at least a short duration. Therefore, the optical flow only estimates image motion.

The most intuitive approach to understand is to find a displacement field from matching the same feature among an image sequence, a feature-based approach. Conceptually for this approach, the interested features of which their brightness is assumed to be unchanged is identified and tracked to quantify their motions. Therefore, algorithms using the feature-based approach involve both feature detection and segmentation as pre-processing for motion estimation. Edge detection is among the most common feature detectors due to its well-advanced theory. Most edge detection methods are obtained from the first image derivative [148] or zero-crossings in the Laplacian of a Gaussian of the image [149], and the image motion at the edges is measured from the brightness constraint. The approach has advantages of reducing the work load to be processed from unimportant parts whereas other approaches attempt to find flow everywhere which is poorly conditioned in some situations. Additional constraints are typically imposed on the measured image motion for a flow field with smooth variation. The works related to this approach are referred to [150-155]. In addition, the flow field

can be used for motion tracking [156-162]. However, the disadvantage of this approach is that a flow field is sparsely measured at which the edges are detected. It is well suitable to track a rigid object or multiple rigid objects from a sequence of images, but is relatively difficult for fluid flows unless sufficient features are introduced along with the flow in the image sequence.

The second class of optical flow methods is to determine an optical flow from the spatial and temporal derivatives of the image brightness. This is also called the gradient-based method and is probably most well-known by [163]. To demonstrate this, let $I(\mathbf{x}, t)$ is an image intensity function depending on \mathbf{x} , the coordinates for spatial location, and t , the time being imaged, then according to the assumption of the optical flow

$$I(\mathbf{x}, t) \approx I(\mathbf{x} + \delta\mathbf{x}, t + \delta t)$$

where $\delta\mathbf{x}$ is the displacement of the moving target at (\mathbf{x}, t) after time δt . Expanding the equation with Taylor series at (\mathbf{x}, t) and neglecting the second and higher order terms, the equation becomes:

$$\nabla I \cdot \mathbf{v} + I_t = 0$$

where ∇I is the spatial intensity gradient; I_t is the temporal intensity gradient; and \mathbf{v} is the velocity vector at (\mathbf{x}, t) . The equation is known as the optical flow constraint, or the brightness invariance constraint. Even though it is easy to understand that the constraint

represents as a two-dimensional problem, its mathematical description is actually generalized for higher dimension. Therefore, two- and three-dimensional flow, or a planar and actual flow, problems can be obtained from the optical flow constraint. However, it was shown that only the optical flow constraint might not be sufficient to be solved for velocity components due to the aperture problem [164-167]. Also, it is readily seen that the optical flow only yields the velocity perpendicular to the optical flow constraint equation. Hence, there are also conditions for optical flow to be exactly image motion [164, 168].

The optical flow methods that determine a flow field from the optical flow constraint are also referred to the differential method. The differential method is usually used additional regularization to overcome the aperture problem. Slowly varying optical flow constraint was first used by [163] and became the common smoothness constraint. The method finds \mathbf{v} that minimizes an error function:

$$\int_D \left((\nabla I \cdot \mathbf{v} + I_t)^2 + \lambda^2 \text{tr}((\nabla \mathbf{v})^T (\nabla \mathbf{v})) \right) d\mathbf{x}$$

where D is the region of interest. The size of the region in the optimization determines whether the optical flow method is global or local. In the global method, additional constraints are motivated to make the optical flow applicable to more realistic time-varying imagery. These are such as continuity equation from fluid dynamics [169], a constraint based on the geometry properties of the 3D scenes [170], a constraint to model a linear transformation of the image intensity [171], the variable brightness optical flow

equation for MR image sequences [172], a constraint for diffuse and specular lighting effects for a moving object in a scene with one light source [173], and quadratic or non-quadratic constraints for smoothing a flow field [166, 167, 174].

In the local method, a single flow pattern is assumed to find velocity in the local area. Therefore, the optical flow constraint can be solved for the local constant velocity by the weighted least square method [175-180]. The aperture problem may be analytically resolved by differentiating the optical flow constraint to obtain equations involving second-order intensity derivatives [164, 181-185]. A need to estimate intensity derivatives for the optical flow constraint can be avoided by using the Gaussian divergence theorem [186], which can also overcome the aperture problem if a sufficient size of neighborhoods is used. In addition, optical flow estimation based on spatiotemporal filters has been reported [187, 188]. Higher-order spatiotemporal derivative filters were used to achieve more robust estimation [188].

Optical flow estimation using statistical approach has also been reported [189-193]. The method forms the optical flow with constraints in the state-space equation and uses iterative filtering procedure, specifically the Kalman filtering, to obtain local flow estimates. Linear or non-linear constraints can be incorporated in the state-space equation for a realistic motion analysis [194]. The state-space equation can address both spatiotemporal coherence and noise, hence providing a robust optical flow estimation framework. Since Kalman filtering is based on many observations in an entire image sequence, the method can be used in motion tracking to compute trajectories of different individual objects in the image sequence [195]. However, a good assumption on the

uncertainty estimates is usually required for the observation model of Kalman filtering approach. This might be a major drawback of this filtering approach since such the assumption is difficult or perhaps impossible to hold when nonlinear constraints are required [196]. In addition to Kalman filters, other filters such as \mathcal{H}_∞ or Weiner filters can be used for motion estimation [194, 197].

Hierarchical processing can also be applied with the optical flow constraint to measure large image motions. When measuring large image motions, the optical flow constraint might not be appropriate to be solved at one resolution due to undersampling and aliasing effects. Initial estimates are obtained at the coarsest level and projected onto the finer level. The estimates are refined until the finest level is reached. This makes the optical flow constraint applicable for large image motions [198]. Furthermore, not only is hierarchical processing applicable to most optical flow methods [199-203], but it also improves computational efficiency to handle fast motions [204].

Furthermore in the Fourier domain, the optical flow can be extracted from a series of motion images based on spatiotemporal filters, referred to the frequency-based method. From the translating intensity image $I(\mathbf{x} + \delta\mathbf{x}, t + \delta t)$, its Fourier transform is

$$\hat{I}(\mathbf{k}, \omega) = \hat{I}_0(\mathbf{k})\delta(\mathbf{v}^T \cdot \mathbf{k} + \omega)$$

where $\hat{I}_0(\mathbf{k})$ is the Fourier transform of $I(\mathbf{x}, 0)$, δ is a Dirac delta function, and (\mathbf{k}, ω) is spatiotemporal frequency. The Fourier transform of a moving image suggests a relationship with that of the static image in the spatiotemporal frequency domain. With

the image brightness consistency assumption, this provides the optical flow constraint equation in the frequency space:

$$\mathbf{v}^T \cdot \mathbf{k} + \omega = 0$$

Therefore, the image motion forms an oblique plane through the origin of the spatiotemporal Fourier space [164]. The speed and direction of motion can be detected from the orientation of the plane [205] using velocity-tuned filters. Gabor filtering is commonly used to decompose spatiotemporal energy of the motion image, and then the integration of the responses from Gabor filters with several orientations provides an estimation of local image velocity [202, 206, 207]. For more robust methods, the outputs from band-pass velocity-tuned Gabor filters can be modeled as complex-valued. The phase part of the outputs provides the velocity in the normal direction to the level phase contours [206]. This is more robust than either intensity derivatives or energy-based filter in the case of varying scene illumination since the amplitude change has little effect on the phase part of the signal [164].

Another class of the optical flow methods finds the image motion by correlation matching between two contiguous time-varying image regions, so-called correlation-based matching methods. The correlation matching is similar to differential methods, but the cost function for optimization problem is changed to a correlation function between the two images.

$$\int_D f(\mathbf{x} + \delta\mathbf{x})g(\mathbf{x})d\mathbf{x}$$

The displacement is defined as the shift $\delta\mathbf{x}$ that maximizes the correlation integral between the two images within a correlation window size D . The matching methods do not rely on the presence of image features; therefore, they have an advantage over the differential and frequency-based methods when numerical differentiation is impractical due to small temporal support or poor signal-to-noise ratio [208, 209]. In this review, the correlation-based optical flow methods will be emphasized in the next section on the particle image velocimetry for fluid flows.

Particle Image Velocimetry

Particle image velocimetry (PIV) is a technique which allows the velocity of a fluid to be simultaneously measured throughout a region illuminated by a two-dimensional light sheet [210]. It has also recently been accepted as a reliable quantitative flow visualization technique [211]. (application referred)

The technique introduces particles into the flow and estimates the local fluid kinematics from the particle motion. The particle motion is captured at known temporal resolution by a camera gating with a mechanical or electronic shutter along with an illumination of either a pulsed or continuous light source. When a seeding density in a resolution, or a source density, is high ($N_s \gg 1$), a group of particles scatter lights and form a characteristic of high-lights pattern, or a ‘speckle’ pattern, which will follow any movement of the flow. Particle images can be obtained when the source density is low ($N_s \ll 1$), and the flow estimation is referred to as particle image velcometry. The average number of particle images in an interrogation cell N_I will define the image

density of the PIV images. To achieve the fluid flow estimation, the particles should be near neutrally buoyant and efficiently scatter light [210, 212]. That is, the particles do not change the fluid flow characteristic and can be clearly imaged with light.

The flow estimation from the particle images for high image density PIV initially adopted an image analysis for a speckle pattern that is called Young's fringe method of interrogation. Young's fringes are formed by the image pairs acted as interfering point sources with the transmitted light, and the amplitude and orientation of the fringe spacing was analyzed for the image displacements [210, 212-215].

A Fourier transformation of the fringe pattern results in the spatial autocorrelation of a single-frame double-exposure particle image.

$$R(\mathbf{x}) = \int_D I(\mathbf{x})I(\mathbf{x} + \delta\mathbf{x})d\mathbf{x}$$

It should be reminded from the right-hand side of the equation that the PIV is actually one of the correlation-based optical flow methods even though its idea originated from the speckle metrology. The correlation function can be decomposed into different components, but the displacement component is used to compute the mean displacement within the interrogation window. The volume average velocity is then obtained by measuring the distance between the centroids of the zero-order and the two first-order peaks [210, 212, 216]. The other components can contribute to a biased or erroneous displacement measurement [217].

As the early implementation of PIV, a fully analogue processing to form the autocorrelation by transform lens (or the optical correlator) was developed [218-220]. Furthermore, spatial filtering techniques to select equal velocity regions from the

diffraction pattern can be applied to produce contours of equal velocity being observed in the image space [221, 222]. These conventional PIV implementations can provide accurate results with high spatial resolution. However, the processing time is the bottleneck for the analogue transformation and hinders the application of PIV to study the dynamics of turbulent flows [223]. The birth of digital recording has eased particle image velocimetry eliminates the photographic stage and makes multi-frame and ensemble measurement easier with a cost of spatial resolution [210, 224, 225]. With its advantages, digital particle image velocimetry (DPIV) has been developed based on analysis of multi-frame, single-exposure PIV images. In such this situation, the spatial autocorrelation in the PIV analysis becomes the cross-correlation [217, 226]. In fact, the cross-correlation can be used to analyze single-frame, double- or multiple-exposure PIV images if the images can be separated or identified for each exposure [217, 227-229]. Decomposition of the cross-correlation results in similar components as those of the autocorrelation function, except for the pedestal and negative displacement components [228]. In [230], quantification for sources of errors in two-dimensional DPIV and a method to reduce those errors were also proposed. Furthermore, an adaptive sampling and windowing interrogation method was recently proposed for the PIV analysis to address the loss of robustness or measurement precision due to inhomogeneous particle seeding [231].

Numerous applications of DPIV have been investigated. In experimental fluid mechanics, quantities other than velocity such as vorticity, acceleration, pressure field, and temperature, can be calculated using PIV data to aid in design of structures, wave

studies, modeling of turbulence, and investigations of thermally driven flows [232-237]. In aerodynamics, PIV has been used to investigate turbine systems for cost-effective, reliable energy conversion systems [238, 239], better flow conditions for gas-liquid mixing reaction in stirred vessels using a pitched-blade turbine [240], or turbulent flow study in a vessel stirred by a Rushton turbine [241]. In jet industry, many types of jets have been investigated using PIV [242-245]. For example, the application of proper orthogonal decomposition (POD) to PIV results helps understand the recirculation zone of an annular jet [242]. The dual-plane stereoscopic PIV was applied on a lobed jet mixing flow to reveal various vortex structures quantitatively and instantaneously [243]. PIV measurements demonstrated the potential to utilize the confined twin-jet geometry to enhance mixing for a wide range of applications [244]. In aircraft industry, DPIV system was used to provide real-time, detailed information of the flowfield near the body and aft of the wing [246]. Stereoscopic DPIV was utilized to measure the velocity field near the apex region of moderately swept delta wings for combat or supersonic aircrafts according to the angles of attack [247]. A high resolution dual-frame digital camera was applied in the study of helicopter rotor aerodynamics and wake vortex measurements of an airplane model [248].

Recently, a micron-resolution PIV (micro-PIV) system has been developed to measure a velocity field with order 1- μm spatial resolution [249-253]. An algorithm for estimating time-averaged velocity fields can be applied to the situations that signal strength is insufficient and that instantaneous velocity field is not necessary for many of the low Reynolds number flows [217]. High-resolution PIV was later developed, and the

method has been widely utilized to measure, characterize, or visualize fluid flows in miniature structures such as microfluidics [254, 255] and micromixers [256]. Furthermore, high-speed micro-PIV has been developed to capture the transient flow in microfluidic devices [257]. The instantaneous flow structure obtained from micro-PIV allows many applications for microfluidic devices such as microchannel geometry design [258], flow control in microchannels [259, 260], mixing in microchannels [20, 261]. In biomedical areas, the high-resolution PIV is used to measure a red blood cell (RBC) velocity field in microvessels [262]. Such those hemodynamic analyses are typically carried out in-vitro, but recently there was a combined technique between X-ray and PIV (X-ray PIV) to extract the quantitative velocity information from blood flowing inside an opaque microchannel [211]. The technique does not require either particle tracers in the blood flow or transparency of imaging materials; therefore, this allows the technique to be possibly carried out the hemodynamic analyses in-vivo.

An extension to three-dimensional PIV has been raised from a flow study for inhomogeneous fluids. No universal scheme for three velocity component measurements has so far been adopted [210]. Many three-dimensional PIV (3D-PIV) approaches have been reported, including stereographic [263-267], holographic [268-273], multi-plane [274-276], color-coding [277-279], or combinations of these approaches [280, 281]. In summary, 3D-PIV is extended from two or more 2D-PIV images at different viewpoints in stereoscopic methods, or beam sources in holographic methods. For multiple-sheet methods, it can be considered as a quasi-three-dimensional PIV technique since velocity fields are only obtained from a series of images taken in parallel planes distributed along

the third axis. Contributions of these 3D-PIV studies are found in various areas such as blood flow characterization in the microcirculation [275], fluid dynamical characteristics of mechanical and biological cardiac prostheses [282], flow behavior for design and fabrication of microdevices [283], turbulent flow measurement and visualization of 3D vertical structures [265], etc.

CHAPTER III

MRI AND MR FLOW IMAGING

A. MRI Basic Principles

MRI is an imaging technique that is primarily used in biomedical applications to non-invasively visualize the structure and function inside a living body. It is the only imaging modality that has the potential of combining anatomical, functional, and perfusion information in a single scanning session. MR signals are produced by the interaction of nuclear spins with an external magnetic field. Generally, atoms with odd number of protons and/or neutrons can produce MR signals. However, ^1H proton imaging is a common type of MRI due to its abundance of hydrogen within biological tissues.

With presence of a static external magnetic field \mathbf{B}_0 , the proton spins will be aligned either parallel or anti-parallel to the magnetic field with a slightly greater number in the parallel position. This results in the net magnetization vector with the same direction of \mathbf{B}_0 , e.g. conventionally in the longitudinal axis/plane. This bulk magnetization precesses clockwise around the external magnetic field with its precession angular frequency (also called the natural frequency or the Larmor frequency):

$$\omega_0 = \gamma B_0$$

where γ is a physical constant called the gyromagnetic ratio. It is dependent on the type of the nucleus, e.g. $\gamma = 2.675 \times 10^8$ rad/s/T or 42.58 MHz/T for ^1H . At equilibrium, the magnitude of the bulk magnetization is constant and dependent on the static magnetic field strength B_0 .

$$M_0 = \frac{\gamma^2 \hbar^2 N_s}{4KT_s} B_0$$

where \hbar is Planck's constant (6.6×10^{-34} J-s), N_s is the total number of spins, K is the Boltzmann constant (1.38×10^{-23} J/K), and T_s is the absolute temperature of the spin system. With a sufficient static magnetic field strength, the bulk signal at equilibrium can be measured. This signal later turns out to be useful to reveal NMR effects of the substance under the magnetic field.

In order to pick up the nuclear magnetic resonance (NMR) signal, another important phenomenon called Resonance needs to be conducted. The resonance occurs when a radio frequency (RF) pulse at the frequency close to the Larmor frequency is transmitted into the substance under the static magnetic field. This RF pulse can be described as a time-varying magnetic field \mathbf{B}_1 that has its magnitude much lower than the static magnetic field. Its direction is typically perpendicular to \mathbf{B}_0 , i.e. in the transverse plane. This will cause small perturbation (or excitation) to the bulk magnetization to move out of the alignment away from \mathbf{B}_0 onto the transverse plane at a certain angle. The angle at which the bulk magnetization moves out from the alignment is called flip angle. This flip angle α depends on the pulse strength and its duration τ_p by:

$$\alpha = \int_0^{\tau_p} \gamma B_1(t) dt$$

and the transverse magnetization after this RF pulse is:

$$M_{xy} = M_0 \sin \alpha$$

This transverse magnetization is also moving in the Larmor frequency framework. If a receiver coil is placed through which this time-varying magnetic flux passes, it will induce the electromagnetic flux at the same rate of the change in magnetic flux according to the Faraday's law. The induced signal from the resonance perturbation is called Nuclear Magnetic Resonance (NMR) signal. It is easy to see that the strongest possible signal occurs when the flip angle is 90° . In other words, all the magnetization is flipped into the transverse plane. Because the amount of ^1H atoms is different for particular materials, they are used to form and to differentiate multiple components in an MR image.

After the excitation, the perturbed magnetization will be relaxed back to its equilibrium. This phenomenon is important to the acquisition of MR images since it determines the duration that the transverse magnetization cannot be detected for imaging. The first relaxation process is a recovery of the longitudinal magnetization – called longitudinal, or spin-lattice, relaxation. It is the process of the net magnetization recovered to the same direction of the static magnetic field at equilibrium. The other

relaxation process is the destruction of the transverse magnetization – called transverse, or spin-spin, relaxation. This relaxation is due to the out-of-phase interactions among the spins in the excited region. Both processes are described by exponential relaxation as:

$$\begin{aligned} M_{xy}(t) &= M_{xy}(0_+)e^{-t/T_2} \\ M_z(t) &= M_z^0(1 - e^{-t/T_1}) + M_z(0_+)e^{-t/T_1} \end{aligned}$$

where $M_{xy}(0_+)$ and $M_z(0_+)$ are the magnetization on the transverse plane and along the longitudinal axis immediately after an RF pulse, and M_z^0 is the longitudinal magnetization at the equilibrium, i.e. $M_z^0 = M_0$. Therefore, both relaxation processes are characterized by the relaxation time constant T_1 and T_2 , which are called the spin-lattice relaxation time and the spin-spin relaxation time respectively. Note that T_1 is always longer than T_2 for a given spin system. Also, these relaxation times are dependent on material properties. We will find these two relaxation parameters are used to form an MR image in the following section.

B. MR Image Formation

Since the relaxation parameters are material-dependent, it is possible to form an object image weighted by its relaxations if the source of the object signals is localizable. We can achieve this by exciting an imaging sample with linearly-varying spatial gradients along the same direction of the static magnetic field. By using a receiver coil,

the transverse magnetization is detected by the induced current. The received signal is the integral of the magnetization over the entire excitation volume.

$$S(t) = \int_{\mathbf{r} \in V} M_{xy}(\mathbf{r}, t) e^{-i\phi(\mathbf{r}, t)} dV$$

where $\phi(\mathbf{r}, t)$ is the phase accumulation caused by the main magnetic field and the linear spatial gradients, i.e.

$$\begin{aligned} \phi(\mathbf{r}, t) &= \int_0^t \gamma [B_0 + \mathbf{G}(\tau) \cdot \mathbf{r}] d\tau \\ &= \gamma B_0 t + \int_0^t \gamma \mathbf{G}(\tau) \cdot \mathbf{r} d\tau \\ &= \omega_0 t + \int_0^t \gamma \mathbf{G}(\tau) \cdot \mathbf{r} d\tau \end{aligned}$$

The gradients result in a linear frequency shift from the Larmor frequency as a function of space. In the other words, spins that experience an increased magnetic field due to the gradient precess with higher frequency than the Larmor frequency, and vice versa. This acts as spatial encoding that makes it possible to localize the signal sources from each spatial location in an imaging volume. In order to complete the spatial encoding for the imaging volume, three gradients along three axes (X, Y, Z) have to be utilized. Without loss of generality, the gradient on Z axis determines the thickness of an imaging slice (slice selection). The gradients along X and Y axis determine the frequency and phase shifts from the center or Larmor frequency in the imaging slice (frequency encoding and phase encoding respectively). Assume three constant gradients are used along the three axes, we can rewritten the phase accumulation in term of frequency encoding $\omega_{fe}(\mathbf{r})$, phase encoding $\varphi_{pe}(\mathbf{r}, t)$, and slice selection $\omega_{ss}(\mathbf{r})$ as:

$$\phi(\mathbf{r}, t) \equiv \omega(\mathbf{r})t = \omega_0 t + \omega_{fe}(\mathbf{r})t + \varphi_{pe}(\mathbf{r}, t) + \omega_{ss}(\mathbf{r})t$$

Slice Selection

Slice selection is performed by applying an RF pulse in conjunction with the constant gradient G_z on Z axis. Consider only the contribution from the linear Z gradient, the frequency offset now depends on Z direction:

$$\begin{aligned} \omega(z) &= \omega_0 + \omega_{ss}(z) \\ &= \omega_0 + \gamma G_z z \end{aligned}$$

When an RF pulse of a bandwidth $\Delta\omega_{ss}$, a slice of thickness Δz whose the resonance frequency is within the RF bandwidth is then excited as:

$$\Delta\omega_{ss} = \gamma G_z \Delta z$$

From the slice selection relationship, the slice thickness can be controlled by both the gradient strength and the bandwidth of the RF pulse. Increase in the gradient strength, or decrease in the RF bandwidth, results in a thin slice, and vice versa. An optimized selection of these parameters depends on the power limitation on the gradient coil and the imaging time limit. The power limitation on the gradient coil will determine the maximum gradient allowed, and an RF pulse with a narrow bandwidth can finally result in a long RF pulse, hence increasing the imaging time.

Frequency Encoding

With the same analogy as the slice selection, frequency encoding is performed with the constant gradient G_x on X axis. The offset frequency is related to the position on X axis as:

$$\omega_{fe}(x) = \gamma G_x x$$

The frequency encoding direction is also called as a readout direction, which refers to the direction that the receiver coil acquires an echo signal by sampling. Typically, the field-of-view FOV_{fe} and the number of sampled data points N_{fe} need to be determined for the frequency spacing $\Delta\omega_{fe}$ during the sampling along the frequency encoding as:

$$\Delta\omega_{fe} = \gamma G_x \Delta x$$

$$\Delta x = \frac{FOV_{fe}}{N_{fe}}$$

Therefore, the frequency spacing actually determines the required receiver bandwidth

$BW_{receiver}$ by:

$$BW_{receiver} = N_{fe} \cdot \Delta\omega_{fe} = \gamma G_x FOV_{fe}$$

Phase Encoding

The phase encoding modulates additional phase along the Y axis on the received signal such that the signal is differentiable on the direction. It is performed by applying a constant gradient G_y on a duration of τ_{pe} . This causes the phase variation along the Y axis as:

$$\varphi_{pe}(\mathbf{r}, t) = \gamma G_y y \tau_{pe}$$

The phase remains after the gradient is turned off. Even though the phase variation can be adjusted by either the gradient strength or the gradient duration, it is preferred to change the phase by adjusting the gradient strength than the gradient duration since it will not affect the imaging time for the adjustment.

K-space Interpretation

Let us define the spatial frequency as:

$$\mathbf{k}(t) = \frac{\gamma}{2\pi} \int_0^t \mathbf{G}(\tau) d\tau$$

Then, the integral of signals over the entire imaging volume can be re-written as:

$$S(\mathbf{k}) = \int_{\mathbf{r} \in V} M_{xy}(\mathbf{r}, t) e^{-i2\pi\mathbf{k} \cdot \mathbf{r}} e^{-i\omega_0 t} dV$$

The complex modulation from the Larmor frequency can be omitted since it is typically demodulated to baseband signals at the receiver. Therefore, the final integral becomes

$$S(\mathbf{k}) = \int_{\mathbf{r} \in V} M_{xy}(\mathbf{r}, t) e^{-i2\pi\mathbf{k} \cdot \mathbf{r}} d\mathbf{r}$$

The received signals are essentially a Fourier transform of the transverse magnetization at the time. Therefore, under the linear encoding gradient assumption, a snapshot of the transverse magnetization at time t can be recovered by the inverse Fourier transform

$$M_{xy}(\mathbf{r}, t) = \int_{\mathbf{k} \in \mathbb{N}} S(\mathbf{k}) e^{i2\pi\mathbf{k} \cdot \mathbf{r}} d\mathbf{k}$$

Fig. 1 illustrates the 2D MR data acquisition procedure. A desired imaging volume is first excited by an RF pulse. Different frequency and phase gradients are used to iteratively measure their corresponding signals that sufficiently cover the spatial frequency space, or k-space (k_x, k_y) . Assume the Cartesian sampling pattern is used; the frequency encoding direction denotes the x -axis direction; and the phase encoding denotes the y -axis direction. With a fixed phase encoding gradient step, a data in a single phase encoding is sampled. The procedure is repeated until sufficient data in the k-space are filled for the inverse Fourier transform. The complete description of the MR data acquisition is typically associated with the image pulse sequence as also illustrated in the bottom of Fig. 1.

There are many considerations for proper MR imaging design. The details on these considerations can be found in [33, 284]. The most common and important factors for a basic MR imaging that will be presented here are sufficient data sampling and image resolution.

The acquired data in the k-space has to be sampled according to the Nyquist sampling theorem in order to prevent the aliasing problem. With the desired field-of-view (*FOV*), the Nyquist condition requires the sampling interval in k-space Δk in the corresponding direction as:

$$\Delta k = \frac{1}{FOV}$$

In the other words, the frequency spacing needs to be chosen such that the reconstructed image does not suffer from a wrapping problem, i.e. the image is not fold over on itself within the desired field-of-view. This can be adjusted by the number of sampling points and the gradient strength along the sampling direction.

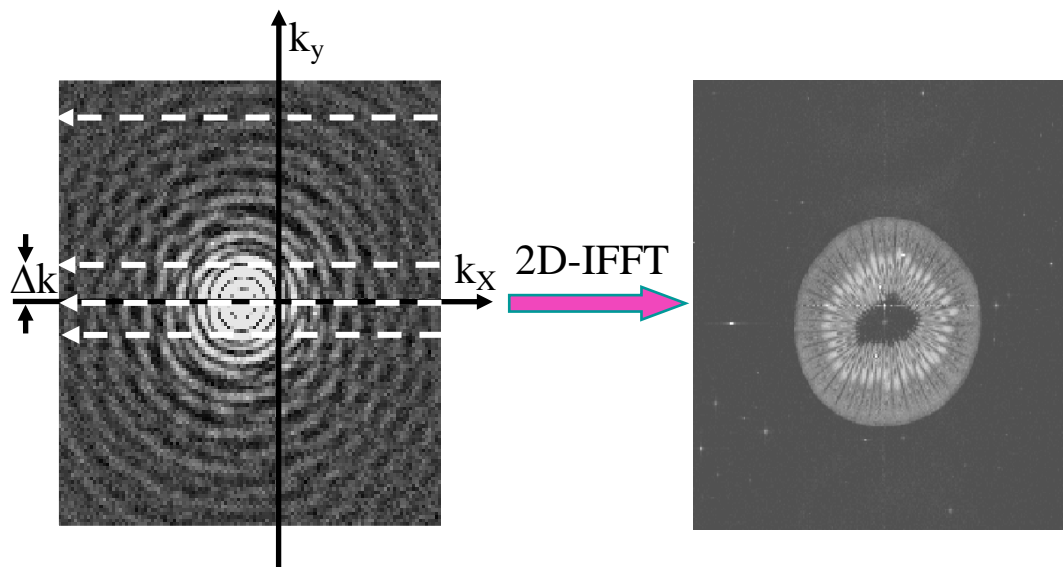
The k-space sampling coverage also determines an image resolution, which is defined as the field-of-view over the number of sampling points:

$$\Delta x = \frac{FOV}{N}$$

At the fixed number of data sampling points, a narrower FOV is desired for the better image resolution. If the field-of-view is increased, the spatial resolution will be reduced. Therefore, number of sampled data points is typically required for a large imaging plane.

C. Fast MR Imaging

One major concern for MRI is that it requires a long imaging time. Normally, typical pulse sequence spends TR seconds to acquire a single echo line. For one good image reconstruction, it might require collecting up to 256 echo lines, hence limiting temporal resolution for image acquisition to some extent. This requires $N_{pe} \times TR = 256TR$ seconds to acquire only a single MR image. In flow imaging, an image data needs to be acquired with good temporal resolution in order to sufficiently capture the characteristic of the flows. This seeks a method to rapidly image on an MR scanner.



$$\text{Scan Time} = N_{\text{PE}} \times \text{TR}$$

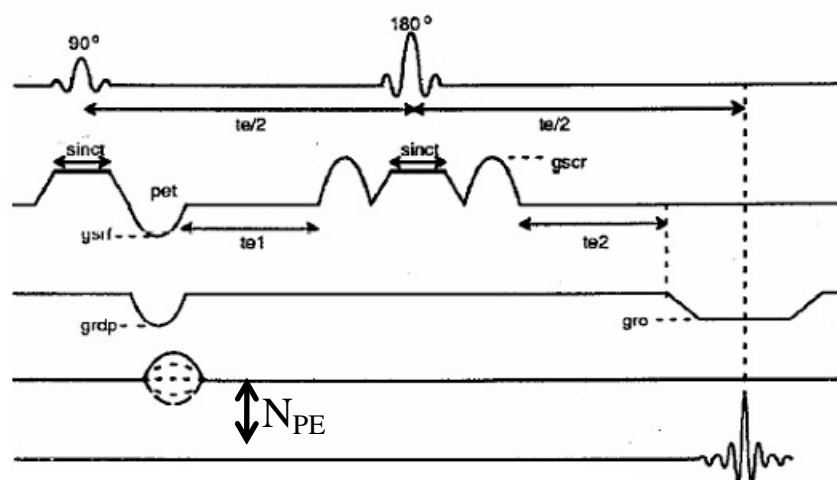


Fig. 1. An example of the MR data acquisition procedure and its associated pulse sequence.

(image excerpt from [285])

The temporal resolution of the image dataset can be simply improved by reducing the repetition time, but this is not helpful when a large number of images are required. Reducing the number of phase encoding lines also penalizes the image resolution in the phase encoding direction. Therefore, a parallel imaging technique that can acquire an image within a short repetition time is desired to address to the temporal resolution issue in MRI. The idea of acquiring multiple data simultaneously within one pulse sequence was developed at the Magnetic Resonance Systems Laboratory (MRSL) Texas A&M University, namely Single Echo Acquisition (SEA) MRI [1-3, 286]. The technique uses a large array of parallel localized coils that is spatially localized to the imaging positions to simultaneously acquire multiple echoes in the Fourier space of a single 2D image. Since the echoes are also spatially localized, each echo produces an image strip by the inverse Fourier transform. The final image is obtained from stacking all the image strips from each coil. This significantly reduces the acquisition time of a single image by the number of coils used. If the number of coils is sufficient, an image can be reconstructed within a *single shot* or one repetition time TR of the pulse sequence. Currently with this imaging method, a sequence of MR images can be acquired at the frame rate as high as 200 frames per second. This has never been achieved by any other MR imaging method. Transient characteristics of complex flows are possibly visualized and/or quantitatively analyzed. Fig. 2 illustrates the image acquisition procedure for SEA-MRI as comparison to the conventional MRI formation.

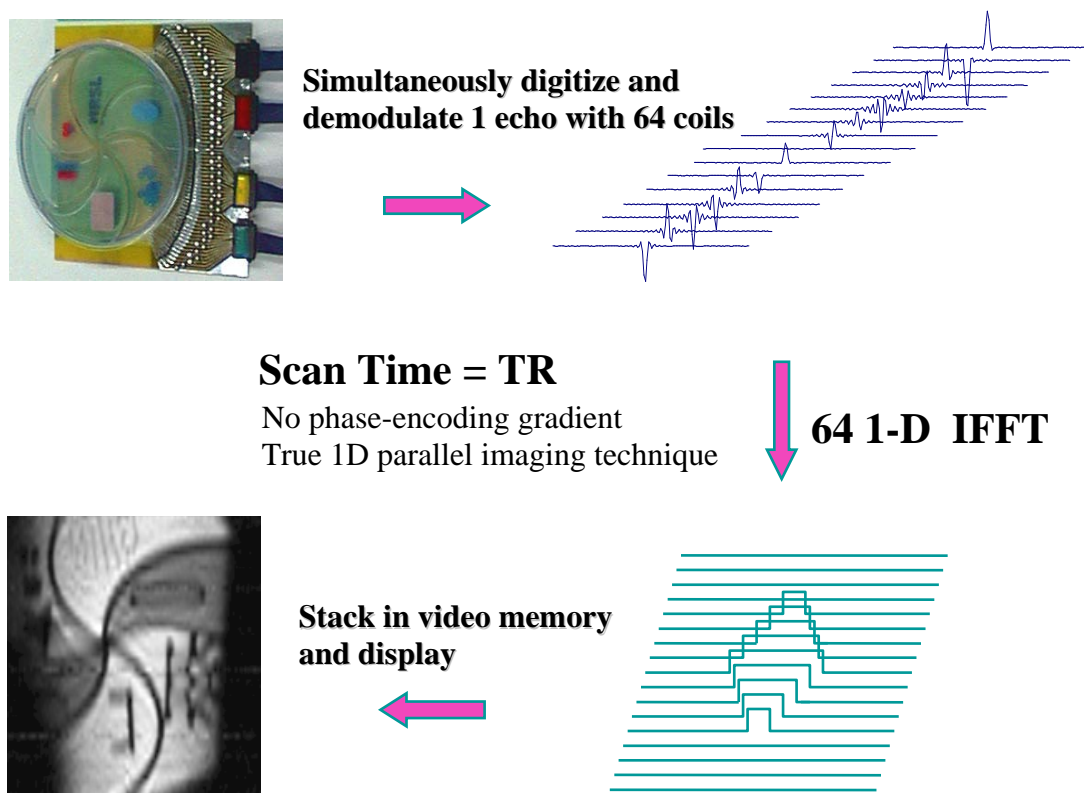


Fig. 2. Imaging procedure for Single Echo Acquisition (SEA) MRI.
(image excerpt from [3])

D. MR Flow Imaging

From the MR image formation, complex MR signals can be used to non-invasively measure flows. Based on the Fourier transform, object motion or flows would result in the phase modulation in the MR signals. Therefore, the phase of a complex MR image provides velocity or displacement information for flows of interest. This allows MRI to be utilized as a flow quantification tool that is referred to as Magnetic Resonance Velocimetry (MRV) [33]. There are two major types of Magnetic Resonance

Velocimetry that use the phase of its complex images to quantify the flows or materials in motion: phase contrast (PCMRI) and tagging MRI (tMRI). The phase contrast method can provide an instantaneous velocity field whereas the tagging method usually provides a displacement field or an average velocity field within the duration that two tagged images are acquired. In this chapter, the principles of flow quantification using both methods are provided.

Phase Contrast MRI (PCMRI)

In the phase contrast method, spatial gradients along the desired flow direction are applied to encode the velocity information on the phase of the moving spins. Let define the time-dependent position of each spin in the excited volume as:

$$\mathbf{r}(t) = \mathbf{r}_0 + \mathbf{v}_0 t + \frac{1}{2} \mathbf{a}_0 t^2 + \dots$$

Apply to the phase of MR signals in a presence of the gradient $\mathbf{G}(t)$ as:

$$\begin{aligned} \phi(\mathbf{r}, t) &= \int_0^t \gamma [B_0 + \mathbf{G}(\tau) \cdot \mathbf{r}] d\tau \\ &= \phi_0(\mathbf{r}, t) + \gamma \int_0^t \mathbf{G}(\tau) \cdot \mathbf{r} d\tau \\ &= \phi_0(\mathbf{r}, t) + \mathbf{r}_0 \cdot \gamma \int_0^t \mathbf{G}(\tau) d\tau + \mathbf{v}_0 \cdot \gamma \int_0^t \tau \mathbf{G}(\tau) d\tau + \frac{1}{2} \mathbf{a}_0 \cdot \gamma \int_0^t \tau^2 \mathbf{G}(\tau) d\tau + \dots \end{aligned}$$

where $\phi_0(\mathbf{r}, t)$ is the initial phase of each spatial location in the excited volume. Let also define the gradient moment \mathbf{M}_i for a gradient $\mathbf{G}(t)$ as:

$$\mathbf{M}_i = \int_0^t \tau^i \mathbf{G}(\tau) d\tau$$

Then, the phase of the MR signals can be re-written as:

$$\phi(\mathbf{r}, t) = \phi_0(\mathbf{r}) + \mathbf{r}_0 \cdot \gamma \mathbf{M}_0 + \mathbf{v}_0 \cdot \gamma \mathbf{M}_1 + \frac{1}{2} \mathbf{a}_0 \cdot \gamma \mathbf{M}_2 + \dots$$

Hence, velocity encoding in a specific direction can be performed by a set of applied gradients that is designed to minimize all the gradient moment terms, but the first gradient moment \mathbf{M}_1 . However, it is difficult to achieve such a gradient set. An additional assumption is required to relax the condition of the gradient set. Assume the imaging can be performed in a small time interval so that acceleration and all other higher motion terms are negligible. Then, the phase of the MR signals can be related to the velocity if the gradients are designed to have a net area of zero (referred to as a bipolar gradient).

$$\phi(\mathbf{r}, t) \approx \phi_0(\mathbf{r}) + \mathbf{v}_0 \cdot \gamma \mathbf{M}_1$$

The initial phase is voxel-dependent and can be due to many sources such as B_0 inhomogeneity, RF inhomogeneity, susceptibility differences, eddy currents, and off-resonance effects [287]. Therefore, two acquisitions with the opposite gradient moment \mathbf{M}_1 are at least required to resolve the flow in one direction. Let define ϕ_1, ϕ_2 as the phase

images of the phase contrast acquisitions with the opposite gradient moments. An apparent velocity can be finally computed from the magnitude of the bipolar first gradient moment as:

$$v = \frac{\Delta\phi}{\gamma\Delta M_1}$$

where $\Delta\phi = \phi_2 - \phi_1$ is the phase difference between the two acquisitions; and $\Delta M = M_2 - M_1$ is the magnitude difference of the bipolar first gradient moment. Fig. 3 illustrates an example of the imaging pulse sequence for PCMRI. A bipolar motion encoding gradient (grey) is typically added between the slice excitation and the data acquisition. It can be added to frequency encoding direction (or read-out: RO), phase encoding direction (PE), or slice selection direction (SS). The phase rewinder gradients are usually utilized for the PCMRI to remove the undesired residual signals.

Since the phase of a phase contrast image is defined in the range of $[-\pi, \pi]$, one important parameter in the design of PCMRI experiments is the maximum velocity encoding value v_{enc} that will produce the phase shift of π radians. The parameter is defined as:

$$v_{enc} = \frac{\pi}{\gamma M_1}$$

Therefore, unambiguous velocity values within the range of $\pm v_{enc}$ can be resolved since the phase shift is hold in between $\pm \pi$. In the velocity measurement, v_{enc} should be set to be larger than the highest velocity under the flow study. In turbulent flow, the flow velocities can, however, vary significantly during the imaging. The v_{enc} must be chosen with this velocity fluctuation in mind [33]. Furthermore, typical 2D or 3D images require many seconds or even up to minutes to complete the full k-space data. In such a case, the phase measures an inaccurate average of aliased and non-aliased samples [33].

It can be shown that the variance σ_ϕ^2 of the phase image from PCMRI is related to the v_{enc} as:

$$\sigma_\phi^2 = \frac{\sigma^2 v_{enc}^2}{|\pi \mathcal{S}|^2}$$

where σ^2 is the variance of the uncorrelated noise in each measurement and $|\mathcal{S}|$ is the magnitude of the signal in a voxel [33]. This needs to be put into consideration for a proper design of v_{enc} for a flow study. In the other words, the optimal v_{enc} should be chosen high enough to prevent the phase aliasing for phase contrast measurements, but cannot be so large that it drastically increases the phase noise.

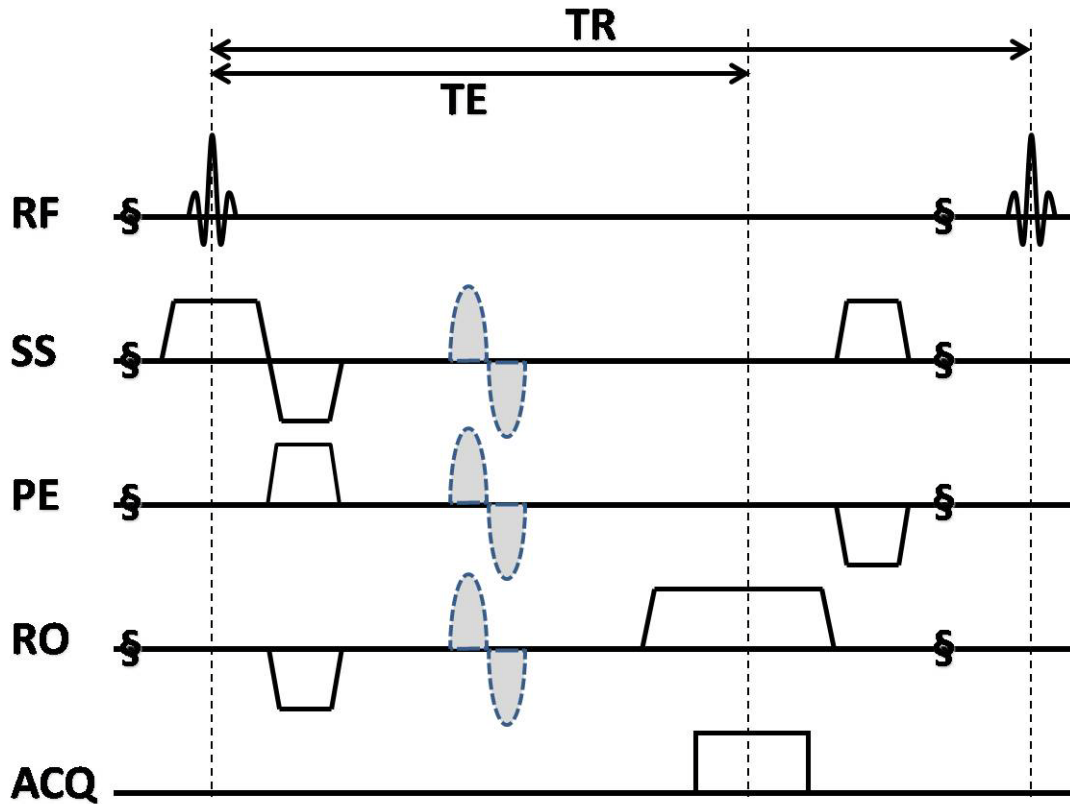


Fig. 3. An imaging pulse sequence for phase contrast MRI (PCMRI).

Tagging MRI (tMRI)

Fig. 4 illustrates the 1-1 SPAMM pulse that is used to produce a tagged image. The first RF pulse with the 90° tip angle is used to tip all the longitudinal magnetization onto the transverse plane. The spatial gradients then are applied to create a spatial excitation pattern of the saturation bands. Then, the second RF pulse with the same 90° tip angle is utilized to store the magnetization with the excitation pattern in the longitudinal axis. The tag pattern for the 1-1 SPAMM tag pulse sequence is given by:

$$f(\mathbf{x};\mathbf{g}) = \frac{1}{2} + \frac{1}{2}\cos(\mathbf{g} \cdot \mathbf{x})$$

where $\mathbf{g} = \gamma \int_0^T \mathbf{G}(t) dt$ is the tag frequency (rad/cm) depending on the encoding spatial gradients. The tag frequency also determines the SPAMM tag orientation. Assuming a constant one-dimensional gradient G with a duration T is used for the 1-1 SPAMM tag preparation pulse. The frequency k of the tag (cm^{-1}) is given by:

$$2\pi k = \gamma GT$$

It is easy to see that the 1-1 SPAMM pulse can be extended to produce 2D tagging by simply re-applying the pulse sequence with a different tag orientation. The extension is done during the preparation pulse, so this will not affect the total acquisition time for the tagged images.

Even though there have been several methods that can quantitatively measure the tag deformation, this section focuses on a promising tool that rapidly quantify tag motion from the phase image of the tag images analogously to the PCMRI analysis. The method is called HARmonic Phase (HARP) imaging. In HARP, it can be shown that the phase image of the complex MR tagging signals encodes the position of tag spins in motion [6, 7]. The phase change from the tag images taken at different times then refers to the tag deformation. Since the deformation of the tag also follows the underlying flows in the

images, the flow quantification can be achieved by the measurement of the phase change from the tag deformation.

Harmonic Phase (HARP) Analysis

HARP analysis is a method to quantify displacements of tag lines from the phase of tagged data in the Fourier space. Fig. 5 illustrates the example of a tagged image produced by the 1-1 SPAMM pulse sequence. Its Fourier transform is shown in the right hand of Fig. 5, which consists of several harmonic spectral peaks of the original untagged Fourier data. In fact, a tagged image can be considered as the convolution of the untagged Fourier data with a train of impulse responses. At a given time t , the tagged image $I(\mathbf{x}, t)$ can be mathematically written as:

$$I(\mathbf{x}, t) = \sum_{l=-L}^L I_l(\mathbf{x}, t)$$

where $I_l(\mathbf{x}, t)$ denotes the l^{th} complex harmonic image. In the other words, the tagged image is resulted from a summation of these several complex harmonic images. The harmonic image is mathematically written by:

$$I_l(\mathbf{x}, t) = D_l(\mathbf{x}, t) e^{-j\phi_l(\mathbf{x}, t)}$$

where $D_l(\mathbf{x}, t)$ denotes a harmonic magnitude image; and $\phi_l(\mathbf{x}, t)$ denotes a harmonic phase image. In two-dimensional case, $\phi_l(\mathbf{x}, t)$ is called the apparent reference map. The harmonic magnitude image D_l is a real-valued image similar to the untagged MR image.

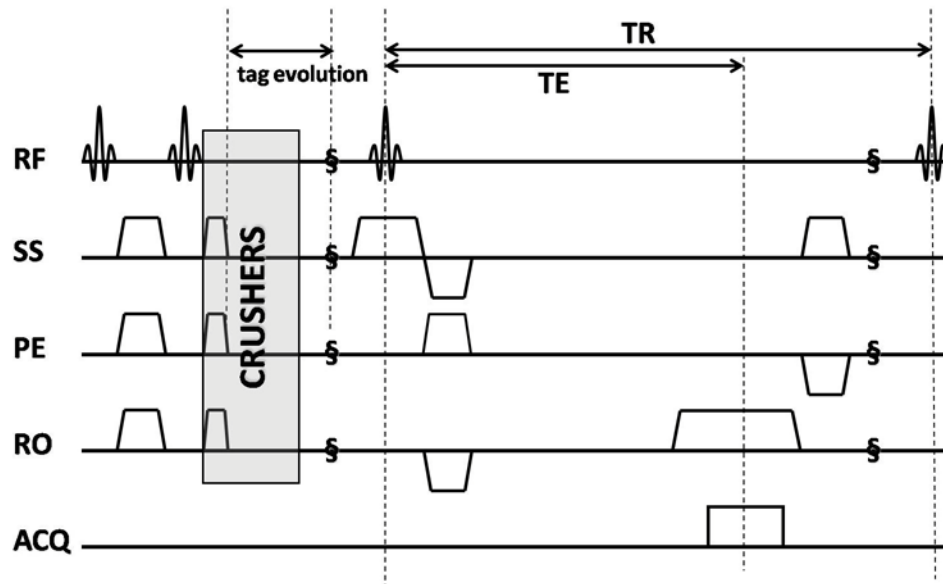


Fig. 4. A 1-1 SPAtial Modulation of Magnetization (SPAMM) pulse sequence.

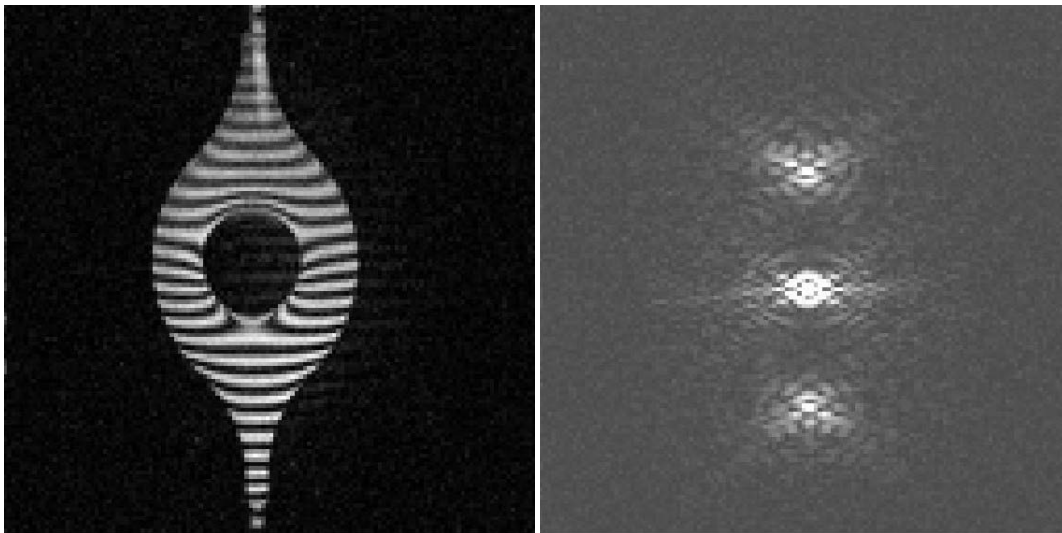


Fig. 5. Example of a 1-1 SPAMM MR tagging image and its k-space data.

It is readily seen that the harmonic phases can be obtained from any of these spectral peaks, except for the central peak. Furthermore, these harmonic phases are closely related to the displacement in the images. It can be demonstrated that the harmonic phase value is a material property of a material point being imaged [7]. Fig. 6 illustrates the 1D example for the material point property of the harmonic phase that moves along with the changing tag pattern at different times. Then, HARP utilizes this phase shift to compute the corresponding tag displacement. Therefore, the principle of HARP relies on the time-invariant of these phase values.

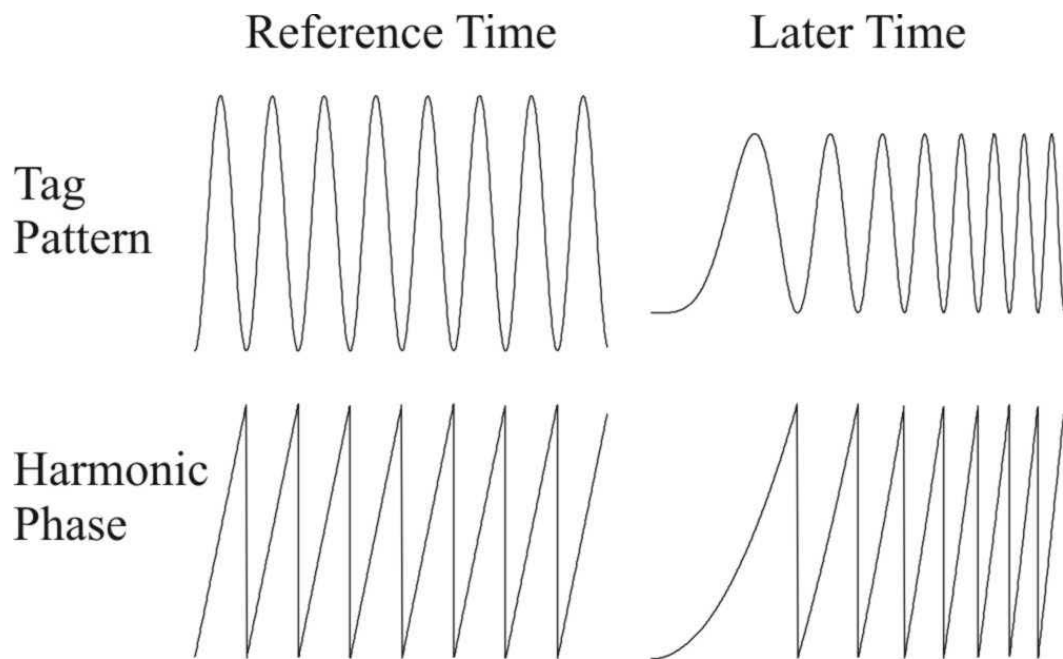


Fig. 6. The principle of HARP: harmonic phase is a material property.

(image excerpt from [85])

Let $\boldsymbol{\varphi}(\mathbf{x}, t)$ be a vector consisting of m harmonic phase values $\phi_l(\mathbf{x}, t), l = 1, \dots, m$ where m is the number of tag orientations. The phase invariance condition of the HARP algorithm can be written in mathematical description as follow:

$$\frac{d\boldsymbol{\varphi}(\mathbf{x}, t)}{dt} = 0 \text{ or } \boldsymbol{\varphi}(\mathbf{x}_{n+1}, t_{n+1}) = \boldsymbol{\varphi}(\mathbf{x}_n, t_n)$$

Note that the left hand definition suggests that the HARP analysis can be considered as one of the optical flow technique as well. Applying the chain rule on the left hand definition, it can be rewritten as:

$$\nabla \boldsymbol{\varphi}(\mathbf{x}, t) \mathbf{v}(\mathbf{x}, t) + \frac{\partial \boldsymbol{\varphi}(\mathbf{x}, t)}{\partial t} = 0$$

where ∇ denotes the spatial gradient; and $\mathbf{v}(\mathbf{x}, t)$ denotes the velocity field at time t .

The velocity field can be solved from the equation by:

$$\mathbf{v}(\mathbf{x}, t) = -[\nabla \boldsymbol{\varphi}(\mathbf{x}, t)]^{-1} \frac{\partial \boldsymbol{\varphi}(\mathbf{x}, t)}{\partial t}$$

However, it is very difficult to compute the velocity field from the derivative of the true harmonic phase since the actual harmonic phase is non-trivial to be estimated. The

HARP algorithm then computes the velocity field above using the wrapped harmonic phase image $a_i(\mathbf{x}, t)$ defined as:

$$a_i(\mathbf{x}, t) = W(\phi_i(\mathbf{x}, t))$$

where W is a wrapping function given by:

$$W(\phi) = \text{mod}(\phi + \pi, 2\pi) - \pi$$

Similarly, the spatial derivation of the wrapped harmonic phase is used instead of that of the true harmonic phase. It can be shown that the spatial derivation of wrapped harmonic phase values $\nabla^* \mathbf{a}$ is equivalent to that of the real phase values under a small motion condition: $|\phi(\mathbf{x}, t_{n+1}) - \phi(\mathbf{x}, t_n)| < \pi$ [74]. Considering the two-dimensional case, the spatial derivation of harmonic phase values can be computed as follow:

$$\nabla \boldsymbol{\phi} \cong \nabla^* \mathbf{a} \equiv \begin{bmatrix} \nabla^* a_1 \\ \nabla^* a_2 \end{bmatrix},$$

where

$$\nabla^* a_i = \begin{cases} \nabla a_i & \|\nabla a_i\| \leq \|\nabla W(a_i + \pi)\| \\ \nabla W(a_i + \pi) & \text{otherwise} \end{cases}$$

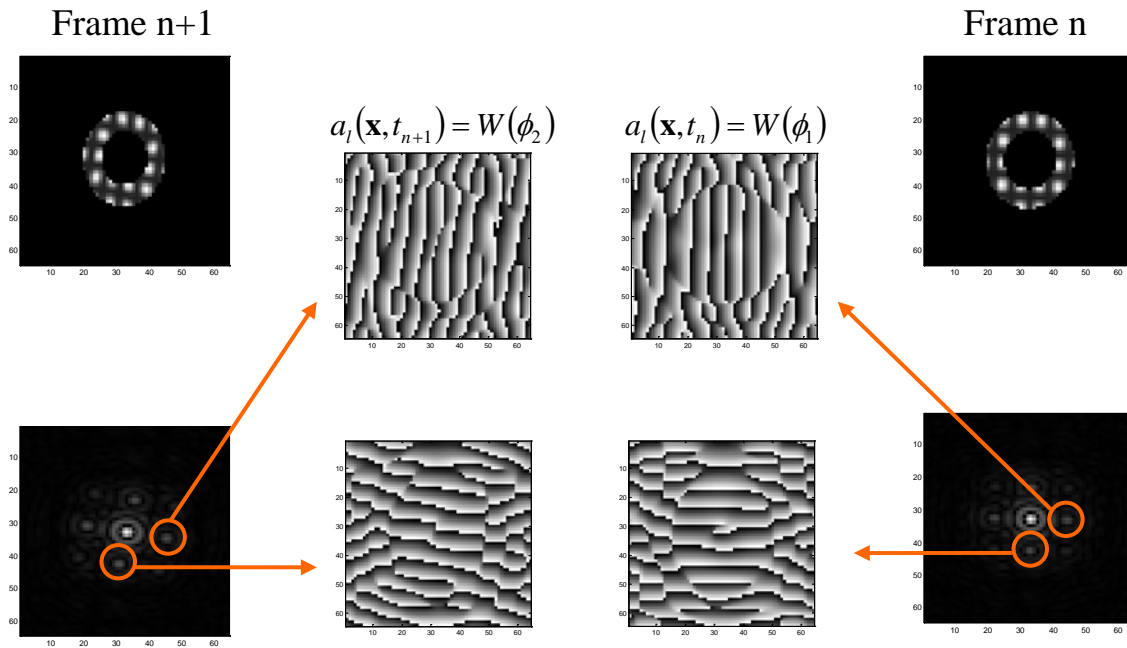
The time derivative of ϕ is approximated from finite differences of \mathbf{a} between two successive tagged frames.

$$\frac{\partial\phi(\mathbf{x},t)}{\partial t} \approx \frac{1}{\Delta t} W[\mathbf{a}(\mathbf{x},t_{n+1}) - \mathbf{a}(\mathbf{x},t_n)]$$

Hence, the velocity profiles can be finally computed from:

$$\mathbf{v}(\mathbf{x},t_n) = -\frac{1}{\Delta t} \nabla^* \mathbf{a}^{-1}(\mathbf{x},t_{n+1}) W[\mathbf{a}(\mathbf{x},t_{n+1}) - \mathbf{a}(\mathbf{x},t_n)]$$

where Δt is the time difference between the image pair. Fig. 7 summarizes the HARP algorithm as described in this section. The two tagged images taken from different imaging times are Fourier transformed into the k-space domain. Two harmonic phase images of each tagged image are extracted by bandpass filters (orange circles) to refer the 2D encoded position of the tagged spins. The change of the phase in two distinct orientations is then used to calculate the velocity field during the time the two images are taken. This velocity field is, in fact, an average of the velocity of moving tag spins rather than the instantaneous velocity.



$$\mathbf{v}(\mathbf{x}, t_n) = -\frac{1}{\Delta t} \nabla^* \mathbf{a}^{-1}(\mathbf{x}, t_{n+1}) W[\mathbf{a}(\mathbf{x}, t_{n+1}) - \mathbf{a}(\mathbf{x}, t_n)]$$

$$W(\phi) = \text{mod}(\phi + \pi, 2\pi) - \pi$$

$$\nabla^* a_i = \begin{cases} \nabla a_i & \|\nabla a_i\| \leq \|\nabla W(a_i + \pi)\| \\ \nabla W(a_i + \pi) & \text{otherwise} \end{cases}$$

$$\text{Small motion condition: } |\phi(\mathbf{x}, t_{n+1}) - \phi(\mathbf{x}, t_n)| < \pi$$

Fig. 7. Summary of the HARP algorithm.

CHAPTER IV

A FLOW QUANTIFICATION ANALYSIS USING SEA IMAGING

A. Rationale of the Work

Single-Echo Acquisition (SEA) imaging is a true parallel imaging method that can be used to image a rapid motion. The imaging method provides an opportunity for MRI to image fluid flows with a good image temporal resolution. A previous work from the SEA imaging can visualize turbulent flows at frame rates as high as 200 frames per second using MR tagging [4]. However, the quantification of the flow work was only performed by a displacement calculation from the manual markers. Even though MR tagging was quite useful to provide visual markers for quantification, such the quantification method possibly induces human errors from marker selection. It is therefore motivated to have a systematic quantification method with less manual intervention that can analyze and provide a dense flow field throughout the phantom geometry.

HARP imaging analysis was proposed for MR tagging to track a 2D apparent flow of the tagged images in a rapid fashion with minimal manual intervention. Even though the analysis was only applied and validated on the analysis of a myocardium motion, its theory is not restricted to a periodic motion. In this chapter, HARP is used to demonstrate its usefulness to analyze fluid flows. Specifically, the HARP algorithm was used to quantify velocity fields from the SEA data acquired with the MR tagging pulse.

B. Methods

Flow Phantom and Experiment Procedure

A flow phantom with separate channels as illustrated in Fig. 8 was used to acquire and visualize the flow data. The phantom has its physical size of $130 \times 80 \text{ mm}^2$. The flow input was limited by the 3/16" tube connected at the phantom's inlet, but the flow rate inside the phantom can be varied depending on the mass flow volume through the phantom. Different flow rates were provided by a Cole-Parmer Masterflex peristaltic pump. In the experiment, distilled waters were used in order to provide a slow decay of the tags.

SEA Imaging with MR Tagging

Tagged images from the turbulent flow phantom were acquired using SEA imaging with a highly localized 64-channel receiver. SEA imaging was performed at 200 frames per second with a spin-tagging preparation pulse using the modified DANTE RF pulse trains and a modified spoiled gradient echo sequence acquisition as illustrated in Fig. 9 [4]. In SEA imaging, the frequency encoding is defined on the long axis of the array elements and the slice selection is on the coronal plane [4]. The phase encoding is eliminated in SEA imaging and was replaced with the N_p spatially-localized array coil. Therefore, the phase encoding gradient was also replaced with a compensation gradient. A final image from SEA imaging is stacked from the 1D FFT of 64 localized images. The SEA image typically can have an unequal matrix size depending on the number of

sampling points along the frequency encoding direction N_f , but it can be interpolated into an equal data matrix by zero padding.

In the tagging preparation procedure, a tag orientation were achieved by applying the spatial encoding gradients along with the RF pulse trains [288]. The tag width and tag separation can be chosen from the RF pulse width and its shape. The 2D tag orientation was obtained by applying two successive DANTE RF pulses. The delay (DLY) was used to allow the tag evolution before sampling out the tag data. The tag profile used in the experiment is 2 mm wide with a 6 mm separation [4]. Due to the lower resolution in the frequency encoding (the flow direction), the diagonal tag orientations were chosen for imaging.

The acquisition pulse was successively applied for 64 acquisitions after the tagging preparation procedure, with $TR = 5$ ms.; $TE = 3$ ms.; $FOV = 14 \times 14$ cm²; matrix size ($N_p \times N_f$) 64×128 . Final images were interpolated to 256×256 . Different flow velocities were then imaged successively with 3 second delay to allow tag-spin decay. Flow velocity was increased during the delay.

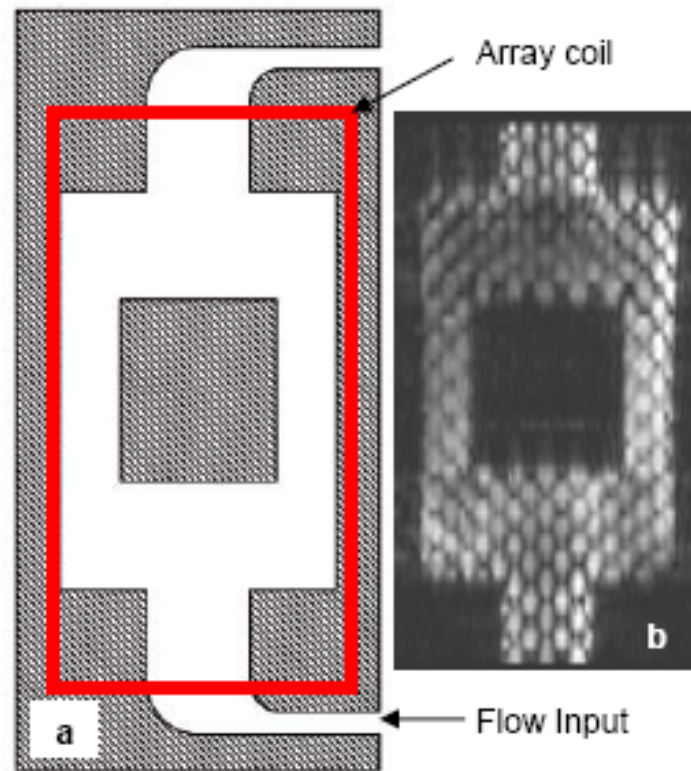


Fig. 8. (a) A separate channel flow phantom used in the flow experiment with SEA imaging and (b) a sample of MR tagging images from the phantom with the 64 channel SEA coil array located as a red box.

(image excerpted from [4])

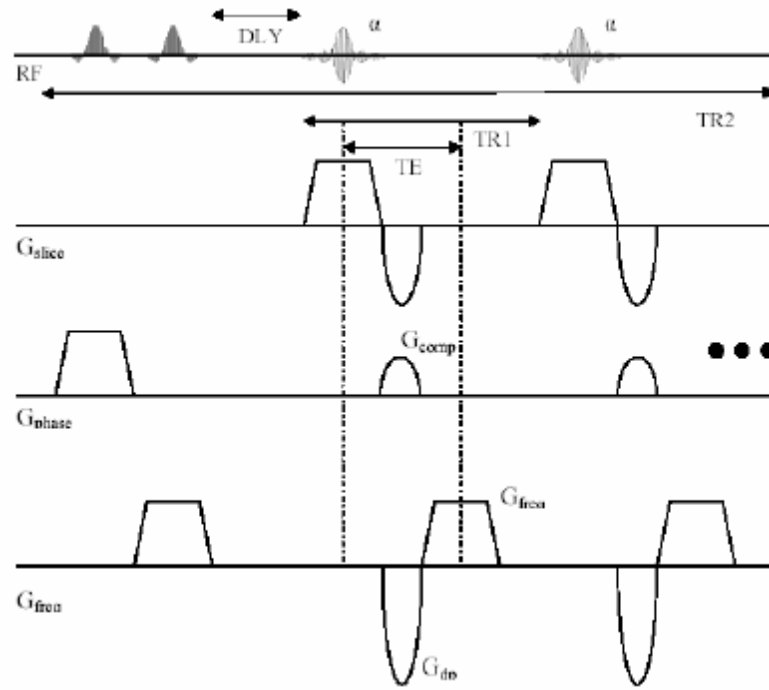


Fig. 9. A 2D tagging pulse sequence with a recalled gradient echo pulse used in the SEA imaging.

HARP Analysis

HARP algorithm described in the background [7] was implemented. In order to sufficiently quantify the 2D apparent motion, at least two harmonic phase images must be extracted from a tagged image. In this work, an elliptic bandpass filter [74] $F_k(\mathbf{k})$ was used for the harmonic peak extraction. The filter can be mathematically written in Fourier domain as:

$$F_k(\mathbf{k}) = \begin{cases} 1, & s_k(\mathbf{k}) \leq 1 \\ e^{-(s_k(\mathbf{k})-1)^2/(2\sigma^2)}, & s_k(\mathbf{k}) > 1 \end{cases}$$

where σ is a standard deviation in a unitless dimension and

$$s_k(\mathbf{k}) = \left\| (R_k S)^{-1} (\mathbf{k} - \mathbf{H}^T \mathbf{w}_k) \right\|$$

Here, $\mathbf{w}_k = [w_1, w_2, w_3]^T$ is a 3D vector for the center frequency of the desired harmonic peak; $\mathbf{H} = [\mathbf{h}_1, \mathbf{h}_2]^T$ and $\mathbf{h}_i = [h_1, h_2, h_3]^T$ is a 3D unit vector for coordinate orientation.

Therefore, $\mathbf{H}^T \mathbf{w}_k$ is the 2D vector of the center frequency of the harmonic peak.

$S = \text{diag}[r_A, r_B]$, where r_A, r_B is the major and minor radii of the elliptic region with the same unit as the center frequency $\mathbf{H}^T \mathbf{w}_k$. R is a rotation matrix corresponding to $\mathbf{H}^T \mathbf{w}_k$.

Fig. 10 illustrates the elliptical bandpass filter used in this work. This filter keeps all the original Fourier data inside the filter, and it reduces the ringing artifacts by a Gaussian decay on the edge.

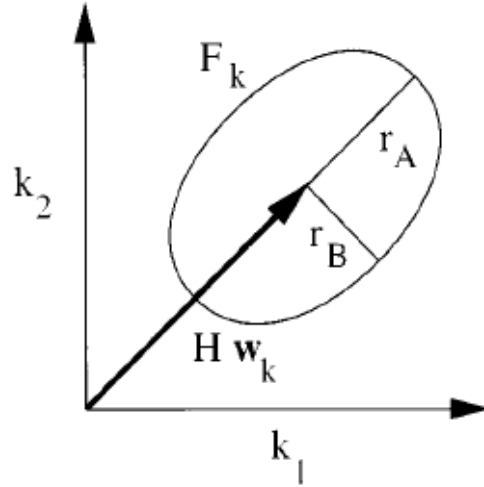


Fig. 10. The elliptical bandpass filter used in the HARP analysis.

(image excerpted from [74])

C. Results

Results from the HARP Analysis

The HARP analysis was initially verified with cardiac simulator data sets [289]. Then, it was applied on the tagged images to analyze the fluid motion. Due to diagonal tag alignment, the central frequencies of the bandpass filters were set to the two first-order harmonic peaks at $\pm 45^\circ$. The elliptic bandpass filter was used to obtain the HARP images, with $r_A = 1.35$ rad/cm, $r_B = 2.24$ rad/cm, $\sigma = 0.2$. This filter was used throughout the analysis. It is reasonable for using a fixed bandpass filter for this study since the phantom structure is fixed. Only the fluids inside the phantom moved, unlike the cardiac motion that the whole object of interest can possibly move.

Fig. 11a-d shows 2D velocity fields from the SEA-tagged images. The velocity fields were computed from the sequence of the tagged images with an equal time interval. To clearly visualize the motion field, the 5th to 95th percentile magnitude truncation was applied on magnitude histogram of motion vectors, and their vector lengths were scaled accordingly. The velocity field in Fig. 11a is zoomed-in and displayed in Fig. 11e-g for different regions at the phantom's outlet, inlet, and channel separation respectively. The results demonstrate a number of interesting characteristics. At the inlet, retrograde flow is observed on the right. The eddy flow is clearly seen on the lower left of Fig. 11g. And the flow is minimal at the shadow region immediately above the center boundary. These are consistent with the flow behaviors reported in [4]. However, velocity errors from the HARP analysis were observed in Fig. 11 a-d. The errors were such as the flows toward the channel boundaries, an abrupt change in the flow directions, and a totally reverse

flow at the inlet of the phantom images, etc. The velocity errors were mainly due to the corruption in the harmonic phase values. The phase corruption could be resulted from the image noises, the field inhomogeneity between the water and the phantom materials, and/or the signal losses from the turbulence of the flows, etc. For example, unrealistic velocity vectors at the phantom's inlet might be due to the signal loss from untagged spins that were newly entered. The third dimension effect from turbulence flows that causes the tag destruction or blurring at the later times also possibly aggravates the signal loss problem. These errors were evident in Fig. 11 b-d when the images at later times were used. The abrupt change in the velocity fields also suggested that there was acceleration from the flows that can cause the maximum displacement exceeds the small condition limit imposed in the HARP analysis.

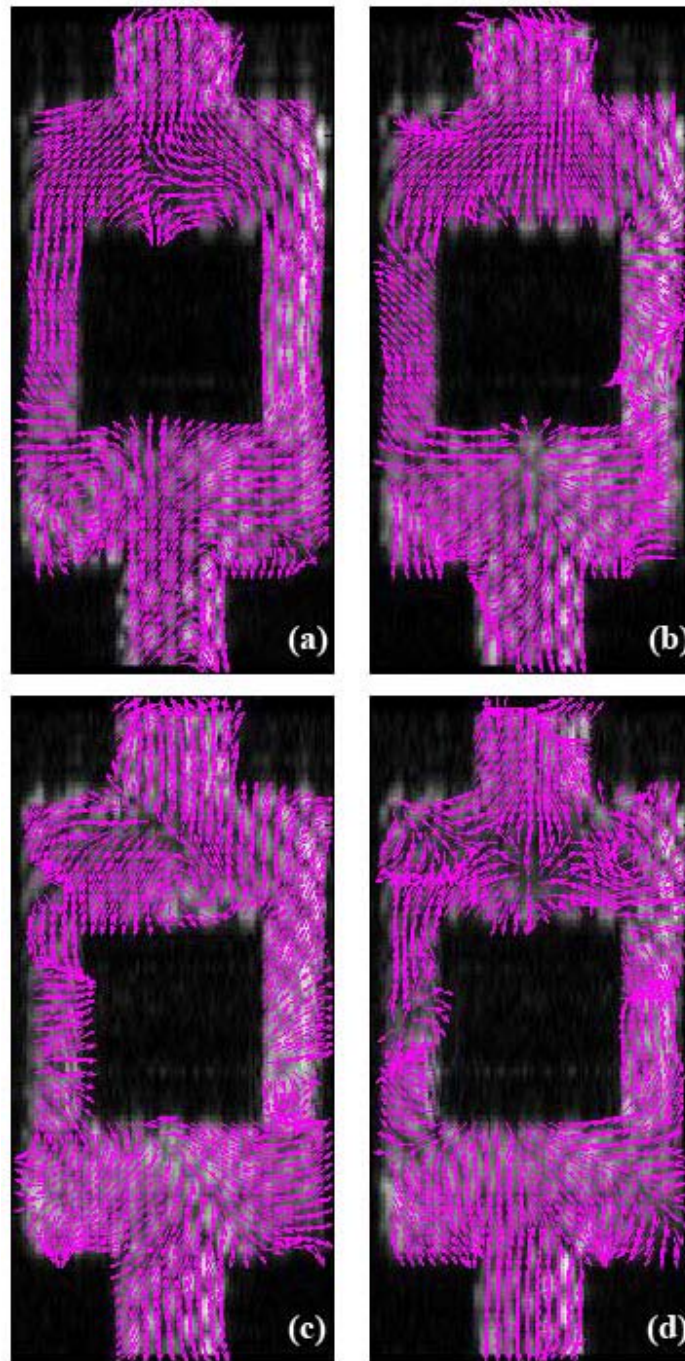


Fig. 11. (a)-(d) Velocity fields at different times in the tagged image sequence, and the zoomed velocity field of (a) at (e) the outlet, (f) the inlet, and (g) the channel separation of the phantom indicated by the green boxes.

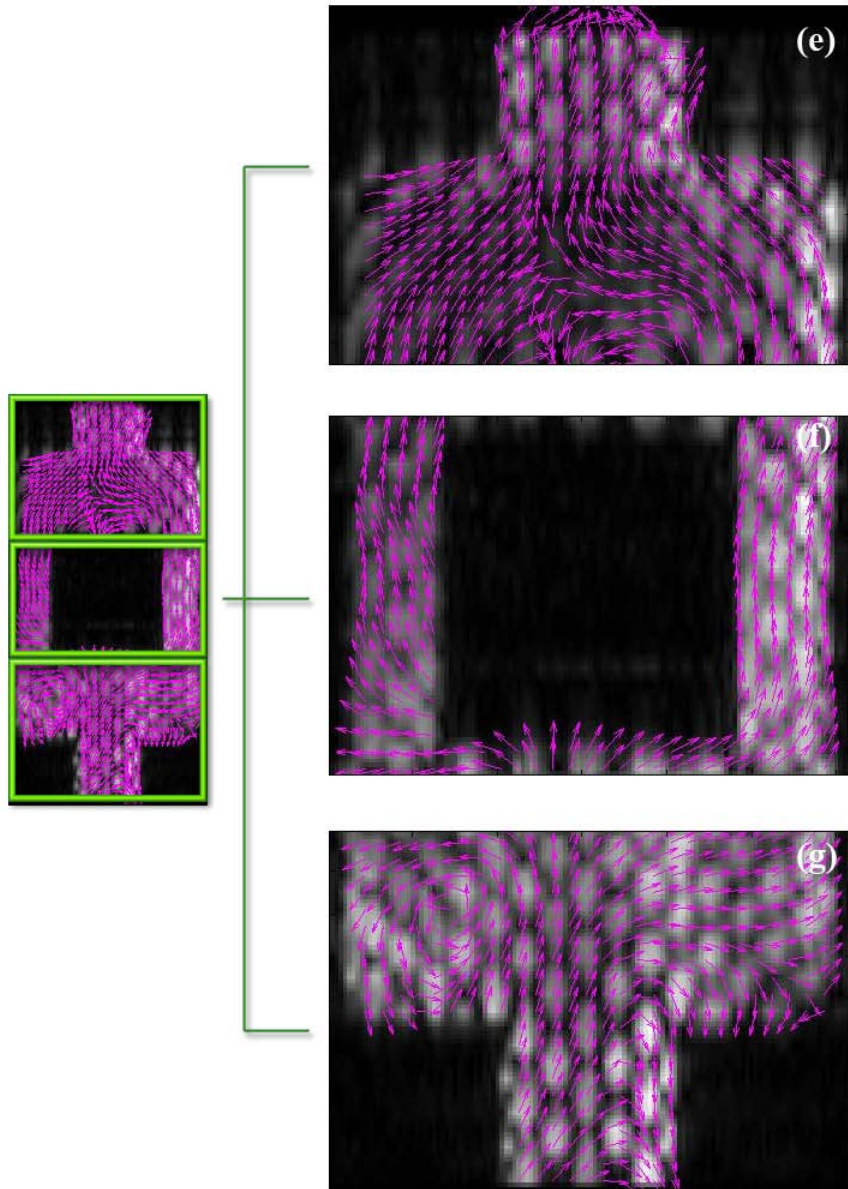


Fig. 11. Continued.

D. Conclusion and Discussions

It can be concluded that the HARP analysis provides promising results for a 2D quantification of rapid flows, yet several improvements are needed as unrealistic velocity fields were demonstrated in Fig. 11b-d. First, the HARP analysis computes a velocity field solely from the harmonic phase images. Image noises during the data acquisition can affect the analysis result. Even though a bandpass filter used for the peak extraction helps reduce the noise to some extent, the persistence of noises in the filtered data can corrupt the encoded flow information. The peak combination method for the HARP analysis [82] can be used to reduce the noise in the k-space data. However, the method might not be helpful when the HARP works on real-valued tagged images because of the symmetry property in Fourier domain.

Moreover, other non-flow factors such as tag fading or field inhomogeneity possibly lead to the phase corruption on the tagged data. The tag fading typically leads to the smearing of the Fourier data among the harmonic peaks. This typically occurs on the images acquired in the later times when the tag spins relax back to the longitudinal axis, but the similar effect possibly occurs when flows at high velocity are imaged. The field inhomogeneity possibly results in the tag distortion and/or the loss of a tag profile at a particular region. These finally lead to a degradation for the phase of the complex tagged data.

In addition to the phase corruption, a velocity field from the HARP analysis has no guarantee that it always follows the real fluid flow. Since the HARP analysis quantifies a velocity solely from the image consistency constraint. The phase invariance condition

does not necessarily represent a true condition for realistic fluid flow behaviors. Therefore, it is motivated to incorporate fluid dynamics constraints into the flow quantification.

Finally, there is no groundtruth velocity field to be compared for the analysis results. Even though the velocity fields from HARP qualitatively demonstrate a good agreement with the flow characteristics reports in [4], a quantitative validation for the work is hardly achieved. It is motivated to have a comparison method to quantitatively verify the usefulness of the HARP analysis for fluid flow studies. This also leads to the experimental comparison of fluid flows between an optical imaging method and MRI in a later chapter.

CHAPTER V
A FLUID REGULARIZATION METHOD
FOR THE MR FLOW QUANTIFICATION

A. Rationale of the Work

As discussed in the previous chapter, it is desirable to take into account the physical constraints for the quantification analysis. The HARP analysis is susceptible to noise and other non-flow factors that degrade the phase of the complex harmonic images. Also, the velocity field from the method has not guaranteed to represent real fluid flow behaviors because it is only computed from the phase invariance assumption. In the theory of Fluid Dynamics, fluid flows can be physically described by the fluid dynamics equations, i.e. the Navier-Stokes equation or the vorticity transport equation. Furthermore, it is legitimate for typical flow studies to assume that the flow is incompressible, i.e. the flows without a change in its density. These physical flow conditions should be incorporated into the quantification of MR flows to obtain reasonable flow fields.

The fluid dynamic equations do not only demonstrate the ability to be used as a regularization method for the flow, but It can also be used to provide flow quantities such as velocity or pressure for the numerical simulation of fluid flows in a geometry of interest. Such a numerical simulation of fluid flows can be achieved by commercial Computational Fluid Dynamics (CFD) software. This can also provide the theoretical ground truth for comparison and validation of our proposed regularization method.

In this work, a flow phantom was designed and built for both simulation and real flow studies of a regularization method for the MR tagging flow quantification. A simulation study of noises for the HARP analysis was introduced to demonstrate that noises possibly make an erroneous or unrealistic velocity field. Then, a regularization method based on fluid dynamic models for incompressible flows [290] was used to improve the velocity field result. Specifically, the method uses a combination of the Navier-Stokes equation, the continuity equation, and the data consistency condition from MR images to regularize the flow analysis. The method is also applied to the real MR tagging images of a flow phantom to test its effectiveness. The results from the new method was demonstrated and compared with the flow field obtained from the original HARP method.

B. Methods

In this section, the velocity field resulted from the novel combination of HARP and fluid regularized models are demonstrated and validated its improvement from that of the original HARP method by the CFD simulation. A noise simulation for the flow quantification using MR tagging was first performed to demonstrate velocity errors possibly resulted from the phase corruption. The flow phantom was designed and used in a CFD simulation of steady and laminar flows to obtain a ground truth velocity field. The velocity field was then used in the MR flow simulation to generate the flow images based on the 1-1 SPAMM MR tagging image equation. Noises were added into the k-

space of the image data, and the velocity field from the noisy tagging images was computed. Then, the regularization was proposed to refine the original velocity field from the HARP to achieve a more reasonable and accurate motion field for fluid flows.

For the real MR data study, MR steady flow images were acquired with the 1-1 SPAMM MR tagging pulse sequence by a volume coil. The MR data was acquired with imaging parameters similarly to the parameters used in the simulation study. Even though the real ground truth cannot be achieved, velocity fields of the regularized method and the original HARP analysis were quantitatively compared with the velocity field from the CFD simulation. It is noted that the method explanation for the HARP analysis was already described in the background chapter and the method section of the previous chapter. Since the same HARP analysis was just used to apply on the real data, it is not described in this method section.

CFD Simulation for a Ground Truth Velocity Field

The flow geometry in Fig. 12 was created in Gambit 2.4 (Fluent, Inc.) and used in the Fluent 6.3, 3D (Fluent, Inc.) to perform the flow simulation. A tetrahedron finite element was utilized, with a node spacing of 1 mm. The properties of the fluid in the simulation were set to the same fluid used for the real MR experiments and were assumed constant throughout the simulation. The mass flow rate of the fluid was set equal to 20 cc per minute, which is also similar to the flow rate used for the real MR experiments. No wall slip and Newtonian, laminar flows were assumed for the CFD simulation. The velocity field solution were derived based on the Navier-Stokes laminar

equation by Implicit-Steady State Solver with which the convergence was set to achieve when the tolerance of the solution is less than $1e^{-5}$. The solution was tested for mesh independency by using several sizes of the node spacing to verify its consistency.

Flow Simulation Using MR Tagging Based on the Ground Truth Velocity Field

A 3D velocity field solution from the CFD simulation was interpolated into 10 different 2D slices throughout the depth of the flow phantom. The 3D velocity field at different phantom depths was averaged to provide a ground truth of an apparent 2D velocity field for the MR experiments.

Based on the ground truth velocity field, the magnitude MR tagging data were generated using the tag pattern equation of the 1-1 SPAMM tag pulse

$$f(\mathbf{x}; \mathbf{v}; t; \mathbf{k}) = \frac{1}{2} + \frac{1}{2} \cos(\mathbf{k} \cdot (\mathbf{x} - \mathbf{v}t))$$

where \mathbf{x} is the spatial coordinates; \mathbf{v} is the velocity field based on the CFD simulation; t is the time interval between the two tagging images; and \mathbf{k} is the spatial frequency of the tags.

In order to simulation a realistic MR tagging data, noises are generated in the k-space of the magnitude data based on the signal-to-noise ratio (*SNR*) of the image that is defined as:

$$SNR = 10 \log_{10} \left(\frac{P_{\text{signal}}}{P_{\text{noise}}} \right)$$

where P_{signal} is the average power of the k-space signal per data point; and P_{noise} is the noise power. Based on the Parseval's relationship, the total energy is preserved in both Fourier and spatial domains. In the case of rectilinear data sampling with $N_x \times N_y$ data points with a sampling interval of Δk_x and Δk_y along x and y directions, respectively. The average power P_{signal} can be calculated by:

$$P_{\text{signal}} = \frac{\int_{\mathbf{x} \in D} |f(\mathbf{x}; \mathbf{v}; t; \mathbf{k})|^2 d\mathbf{x}}{N_x N_y \Delta k_x \Delta k_y}$$

The noises in the k-space are assumed to be independent Gaussian variables. Assume the noise variances of σ_x^2 and σ_y^2 along x and y directions respectively, the noise power P_{noise} is given by:

$$P_{\text{noise}} = \sigma_x^2 + \sigma_y^2$$

Providing the desired SNR and the phantom parameters, the noise variances can be derived straightforwardly.

Flow Phantom and Experiment Setups

A flow phantom with separated channels illustrated in Fig. 12 was used to collect the flow data in an MR tagging experiment. The physical size of the phantom is $7.62 \times 12.7 \times 0.5 \text{ cm}^3$ ($3 \times 5 \times 0.2 \text{ in}^3$), which matches the physical area of the SEA coil's localized sensitivity for flow MR experiments. Note that the channel of the flow phantom is intentionally separated after the inlet to introduce the 2D distribution of a velocity field. The flow setups are also illustrated in Fig. 13. In the study, gravitational flows were used for the experiments by connecting the phantom with two 22.1% g/g glycerol-water reservoirs located at different height h . The density of the fluid mixture is approximately 1.050605 g/cm^3 at the room temperature (25°C). The density is also in the approximate range of the human venous blood density ($1.043 - 1.057 \text{ g/cm}^3$ [291]). Mass flow rates can be adjusted by the valve and an omega FL-213 rotameter (3 – 300 cc/min with $\pm 5\%$ reading accuracy and $\pm 1\%$ reading repeatability) located between just after the reservoir and the phantom's inlet. A 20 cc/min mass flow rate of the mixture flow was performed until the flows reach steady state before imaging acquisition was taken. The maximum velocity at the inlet of the phantom was calculated to be approximately 2 cm/sec ($\text{Re} \approx 86$) at the mass flow rate. The phantom was then fixed into a volume coil designed by Dr. Steven M. Wright. The volume coil used in the experiment is shown in Fig. 14. The phantom with the volume coil was put into the center of the magnet bore of the 40cm/4.7T MR scanner for imaging. The shimming was also performed before the tagging imaging to improve the signals and obtain a good field homogeneity. The phantom length and flow direction was aligned along the magnet bore (z direction),

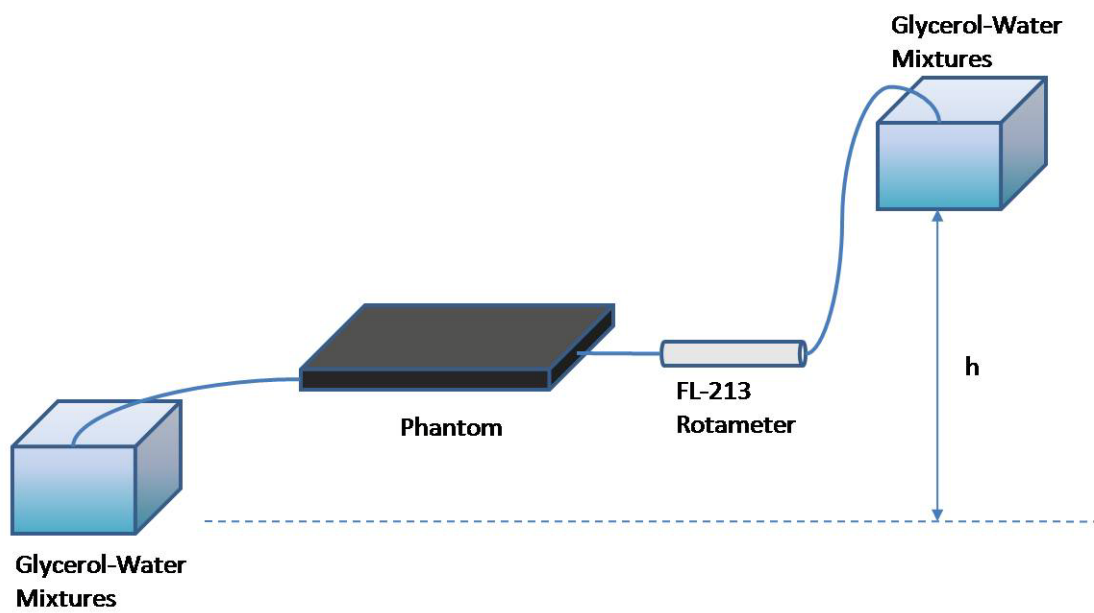


Fig. 13. A sketch of flow experiment setups.

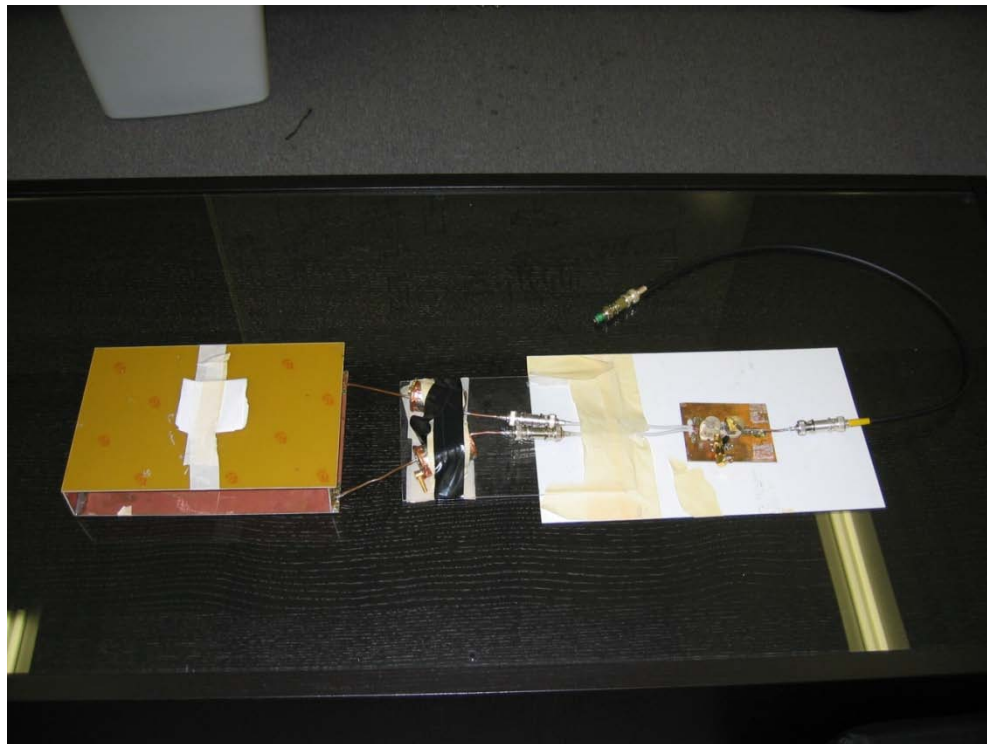


Fig. 14. A volume coil for the MR flow experiment.

Spin Tagging MRI

The spin echo pulse sequence was modified to provide optional tagging preparation before the data acquisition as illustrated in Fig. 15. Two 90° RF pulses and a set of spatial gradients are used to produce 1-1 SPAMM tag orientation. The tagging procedure uses the SPAMM tagging approach with which multi-dimensional spin tagging is easily expandable by multiple applications of the pulse sequence with different combinations of spatial gradients. The crusher gradients were used to spoil the residual of the transverse magnetization when the tag signals are stored along the longitudinal axis.

For convenience, the 1-1 SPAMM tag pulse sequence is repeatedly given from the background chapter by:

$$f(\mathbf{x}; \mathbf{g}) = \frac{1}{2} + \frac{1}{2} \cos(\mathbf{g} \cdot \mathbf{x})$$

Note that the equation is also similar to the image equation used to generate the simulated tagging data, but it offers a different perspective for hardware designs. From the equation, the tag frequency is related to the set of designed spatial gradient, which also determines the SPAMM tag orientation. Assuming a constant gradient g with a duration T is used for a particular direction of the spatial gradient set to simply create a 1D tag orientation along one imaging axis. Again, the spatial gradient should be designed according to the desired spatial frequency k of the tag lines satisfying the relationship provided in the MR background chapter by:

$$2\pi k = \gamma g T$$

Note that the tag frequency should be chosen such that the maximum tag deformation from fluid flows is covered by half of the tag period. If the maximum flow velocity of a flow study v_{max} is imaged with the time duration of t , a chosen tag frequency is required to satisfy the condition:

$$k \leq \frac{1}{2v_{max}t}$$

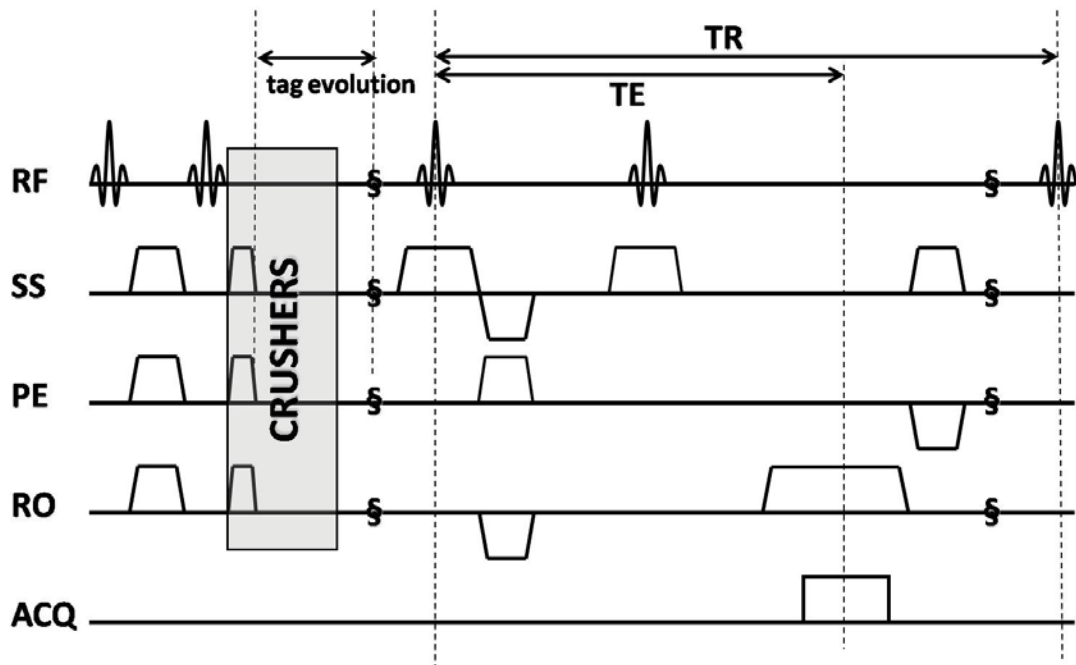


Fig. 15. A 1-1 SPAMM tagging pulse sequence with a spin-echo data acquisition used in the flow experiment.

A Regularization Method with Fluid Dynamics Constraints for MR Flow Quantification

The proposed regularization method for the MR flow quantification imposes a velocity field to satisfy certain smoothness and mass conservation constraints corresponding to the real flows. The idea is motivated from [290]. Specifically, the method is formulated as an optimization with multi-objective functions: 1) the Navier-Stokes equation, 2) the continuity equation, and 3) the data consistency constraint. The minimum residual of these constraints is heuristically found and provided as a solution of the method.

Constraints for the Optimization Formulation

In the proposed regularization method, a reasonable flow field should also satisfy both the principles of fluid dynamics and the data consistency condition. For incompressible fluids (a constant fluid density), 2D flows are governed by the Navier-Stokes equation:

$$\frac{\partial \mathbf{v}}{\partial t} + (\mathbf{v} \cdot \nabla) \mathbf{v} = -\nabla p + \frac{1}{\text{Re}} \nabla^2 \mathbf{v}$$

or the vorticity equation:

$$\frac{D\omega}{Dt} - (\omega \cdot \nabla) \mathbf{v} = \frac{1}{\text{Re}} \nabla^2 \omega$$

where \mathbf{v} is the velocity; p is the pressure; $\omega = \nabla \times \mathbf{v}$ is the vorticity; and Re is the Reynolds number. The Reynolds number is a dimensionless number that defines the characteristic of the flows. It is dependent on the fluid density, viscosity, and the flow geometry. The Navier-Stokes equation should be generalized for a flow study that the constant fluid density assumption holds. Therefore, it is reasonable to assume the incompressible flows for biological flows, e.g. blood flows. Furthermore, it is worth to note that the vorticity equation might be more useful for 2D flows since it does not require knowledge of pressure information to satisfy the fluid dynamics.

Furthermore, incompressible flows should satisfy the continuity equation. In the other words, the rate at which the mass of the flows enters into a system is equal to the rate at which the mass of the flows leaves the system. This is considered as a conservation of the flow mass. In the incompressible flow case, the mass continuity is equivalent to the volume continuity, which can be mathematically written as:

$$\text{div } \mathbf{v} = 0$$

Finally, the velocity field from the flow has to be satisfied the data consistency condition from which the initial velocity field is extracted. That is, for an image pair I_m, I_n where m, n are data acquisition time indices ($m < n$), the interpolation of I_m by its associated velocity field \mathbf{v} should ideally result in I_n .

$$I_n = g(I_m, \mathbf{v})$$

where $g(\cdot, \cdot)$ is the image interpolation function.

Optimization Formulation and Algorithm

The new velocity field is desired to be refined by the fluid dynamic and data consistency conditions described in the previous section. Therefore, we define residual functions for those conditions given an image pair I_m, I_n and its associated velocity field \mathbf{v} as:

$$\begin{aligned} e_1 &= \left(\frac{\partial \mathbf{v}}{\partial t} + (\mathbf{v} \cdot \nabla) \mathbf{v} + \nabla p - \frac{1}{\text{Re}} \nabla^2 \mathbf{v} \right)^2 \\ e_2 &= (\text{div } \mathbf{v})^2 \\ e_3 &= c(I_n, \tilde{I}_n) \end{aligned}$$

where $c(\cdot, \cdot)$ is an absolute difference function, $\tilde{I}_n = g(I_m, \mathbf{v})$ is an estimated image based on the motion vector \mathbf{v} and a previous image I_m .

Therefore, it is desired to obtain a velocity field that minimizes the residuals of the Navier-Stokes equation, the continuity equation, and the absolute difference of the data consistency from the associated velocity field. That is, we want the velocity field that minimizes:

$$E = \lambda_1 e_1 + \lambda_2 e_2 + \lambda_3 e_3$$

where $\lambda_1, \lambda_2, \lambda_3$ are weight coefficients. Ideally, we want the velocity field that provides no residual. However, the conditions are hardly achieved. The solution needs to compromise these non-linear constraints that form a multi-objective function. The solution to those conditions is usually obtained by an optimization algorithm. Several optimization algorithms can be used to provide the ‘optimal’ solution, such as the Newton-Gauss method, gradient-based method, simulated annealing, etc. Even though those methods provide intuitive understanding how they approach to the solutions, they mostly suffer from the local Pareto optimal problem due to the complexity of the cost function.

However, genetic algorithm/ evolution programming (GA/EP) has shown its advantage on the non-linear, multi-objective function. It can heuristically find the optimum solution; therefore, it can prevent the ‘optimal’ solution to be stuck in local Pareto optimal solutions. In brief, the algorithm approaches to the optimal solution by simulating the natural of selection in genetic evolution, i.e. the survival of fittest.

It iteratively chooses the fittest solutions as parents for the next solution generation. The new solutions are randomly reproduced and mutated from the parents. These new solutions, or so called children, are evaluated for their fitness that is defined as the residual function E in this study. Therefore, children with good fitness will have their total residual values decreased as the number of generations increase. The algorithm proceeds until the optimization criteria are met.

The implementation of GA/EP is given as follows:

- 1) *Encoding*. Instead of using a binary bit string, EP defines a possible solution (chromosome) to be consisted of individual velocity components. Let define the i^{th} possible solution vectors for each velocity component $\mathbf{V}_i^x, \mathbf{V}_i^y$ as:

$$\begin{aligned}\mathbf{V}_i^x &= \{v_i^x(0,0), \dots, v_i^x(m,n), \dots, v_i^x(M-1, N-1)\} \quad i = 1, \dots, N_s \\ \mathbf{V}_i^y &= \{v_i^y(0,0), \dots, v_i^y(m,n), \dots, v_i^y(M-1, N-1)\} \quad i = 1, \dots, N_s\end{aligned}$$

where v_i^x, v_i^y are the velocity components (chromosome) on the first and second dimension respectively; m, n are the row and column indices of the velocity component in the region of interest $M \times N$ ($0 \leq m < M, 0 \leq n < N$); and N_s is the total number of possible solution vectors for GA/EP at each generation iteration (the population size). Without loss of generality, the first velocity component chromosomes \mathbf{V}_i^x are used to demonstrate the rest of the algorithm.

- 2) *Creation*. After encoding the suitable gene type for the flow study, the GA/EP starts the program by creating the initial population of chromosomes based on the velocity field resulted from the HARP analysis. Then, N_s chromosomes of each velocity component are generated using a Gaussian random function. Therefore, the velocity component chromosomes can be mathematically described by:

$$\mathbf{V}_i^x = \mathbf{V}_i^{x,HARP} + a \cdot \mathbf{N}(0,1)$$

where $\mathbf{V}_i^{x,HARP}$ is the velocity component obtained from HARP analysis; a is an arbitrary coefficient; and $N(0,1)$ is the zero-mean Gaussian random function with a unit variance.

- 3) *Fitness scaling*. After the population at each generation is generated, each individual gene will be evaluated for its fitness. As the objective for the regularized flows, the fitness function is defined as the sum of total residuals inside the region of interest (ROI):

$$f = \sum_{(x,y) \in ROI} E(x,y)$$

$$E(x,y) = \lambda_1 e_1(x,y) + \lambda_2 e_2(x,y) + \lambda_3 e_3(x,y)$$

In this study, we define the ROI to be all flow channel area inside the phantom.

- 4) *Selection*. For each population generation, the algorithm selects parent chromosomes that will be used to reproduce children of the next generation. The selection is uniformly sampling on a unit probability line that is partitioned based on the reciprocal of individual's fitness $f_i, i = 1, \dots, N_s$. Therefore, the lower the fitness value, the more frequency to be selected as a parent by the algorithm. This selection method is called stochastic universal sampling (SUS).
- 5) *Recombination*. Population of the next generation is reproduced from the selected parents. The next generation population of the constant size N_s are replicated by the following genetic operators:

- a) Elite Children. The M individual chromosomes with best fitness are kept for the population of the next generation. With the operator, the algorithm can pursue the ‘optimal’ solution when the correct searching is obtained.
- b) Crossover. The operator utilizes two distinct parent chromosomes to randomly generate the offspring chromosomes by arithmetic crossover. For example, let the parent chromosomes be $\mathbf{V}_i^x, \mathbf{V}_j^x (i \neq j)$. Two new offspring chromosomes $\mathbf{V}_i^{x,cross}, \mathbf{V}_j^{x,cross}$ can be possibly reproduced as:

$$\mathbf{V}_i^{x,cross} = \alpha \mathbf{V}_i^x + (1 - \alpha) \mathbf{V}_j^x \quad \mathbf{V}_j^{x,cross} = (1 - \alpha) \mathbf{V}_i^x + \alpha \mathbf{V}_j^x$$

where α is the uniform random variable ($0 \leq \alpha \leq 1$). This operator imitates the mating among the same species for survival. By the selection procedure, the individuals with good fitness will have better chance to reproduce children with ‘better’ fitness for the next generation. Other crossover methods can also be utilized.

- c) Mutation. The operator produces a new gene $v_i^{x,mult}$ by randomly changing a parent gene v_i^x . Mathematically, the new gene is created by:

$$v_i^{x,mult} = v_i^x + (\zeta |v_i^x| + \Delta) \sqrt{E(x, y)} \mathbf{N}(0,1)$$

where $\Delta = |v_i^x - \bar{v}_i^x|$; \bar{v}_i^x is the local mean (3×3) velocity of the velocity chromosome \mathbf{V}_i^x ; ζ is a scaling factor that will decrease to zero as the number of generations approach its maximum number of generations predetermined by the algorithm. This operator can prevent wrong pursuit for the 'optimal' solution at the beginning of the search. It also prevents the new children from struggling on their similarity, i.e. the algorithm has local optima or has reached a plateau. The mutation will drastically change in its new value at the beginning of the algorithm, but its change will be dwindled from slow change in the scaling factor as the algorithm runs to a certain generation.

To allocate the number of population for crossover and mutation, the algorithm utilizes the crossover fraction c and the number of elite children M . The algorithm first determines the number of crossover children by:

$$N_{cross} = ROUND[c(N_s - M)]$$

Then, the rest of the population is allocated to mutated children:

$$N_{mut} = N_s - M - N_{cross}$$

- 6) *Stopping criteria.* The algorithm is terminated when
- a) One of the chromosomes reaches the global minimum, or

- b) No improvement on the best solution's fitness value is obtained at certain successive iterations, or
- c) Fixed number of generations is reached.

A summary of the GA/EP algorithm is shown as a flow chart in Fig. 16.

C. Results

The effectiveness of the proposed method was tested on both the MR flow simulated data and the real MR data, with a comparison to the original velocity fields from the HARP analysis. In the simulation study, the velocity 'ground truth' from the CFD simulation was used for the improvement evaluation of the regularized method over the original HARP. In the MR real data study, the actual ground truth velocity field was not obtained. However, the velocity field from the CFD simulation was used as a theoretical basis for the comparison between the regularized method and the original HARP analysis.

MR Flow Simulation

HARP Analysis on the Simulated Data

A 3D velocity field for the flow simulation at the mass flow rate of 20 cc per minute was initially obtained from the CFD simulation by the Fluent software. The averaged flow field from the 3D velocity field throughout the phantom's depth dimension was used at the 'ground truth' for a 2D velocity field in the MR simulation.

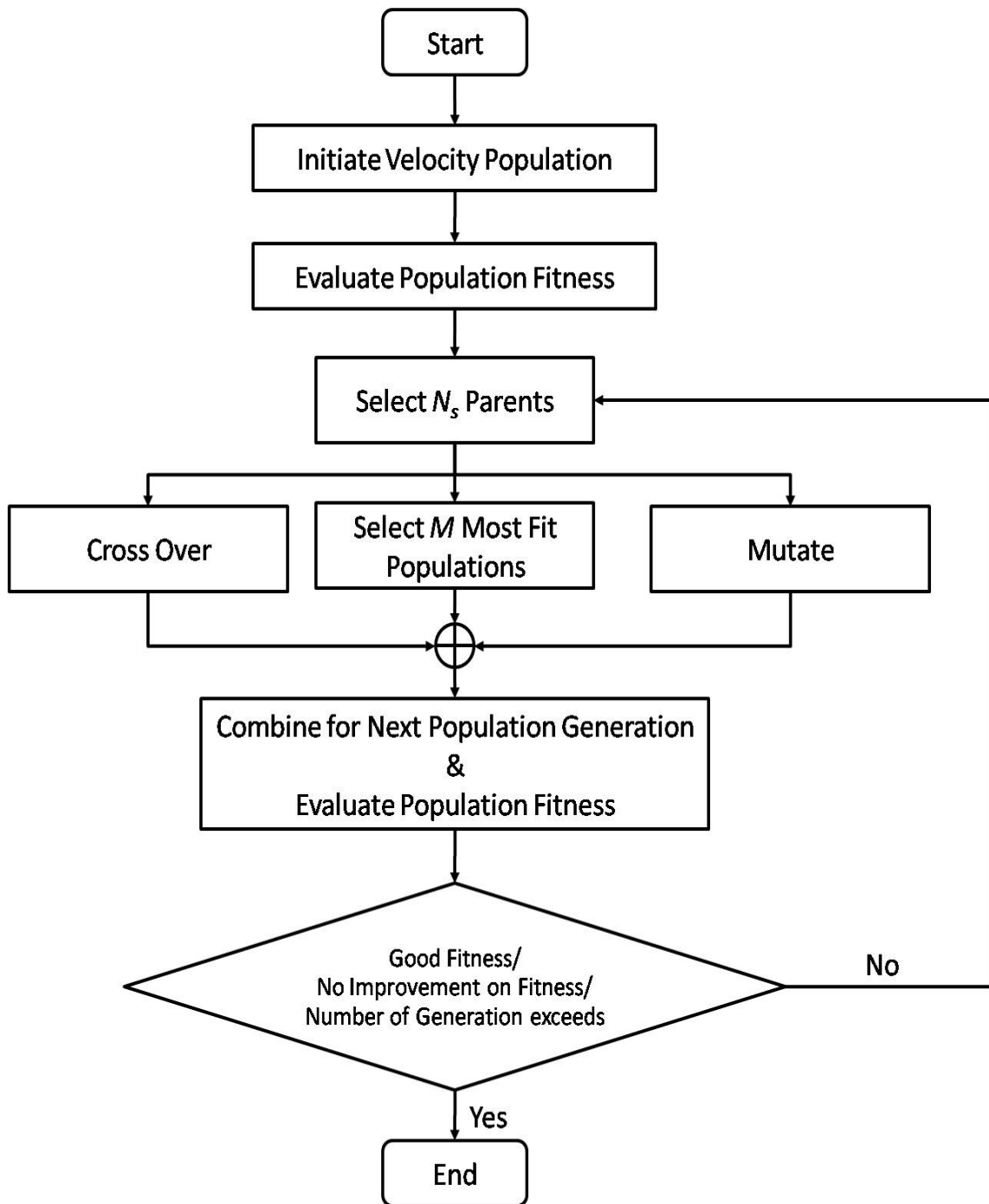


Fig. 16. A flow chart of the Genetic Algorithm/ Evolutionary Programming (GA/EP).

MR tagging images were generated based on the ‘true’ velocity field using the 1-1 SPAMM tagging image equation, with the data matrix size of $N_x \times N_y = 128 \times 128$ pixels; FOV = 137×137 mm²; $k = 2.4$ cm⁻¹; and $t = 0.1$ sec. Noises were added into the k-space data of the simulated magnitude images at SNR = 25 dB. These imaging parameters were similar to the parameters in the real MR experiment. To obtain a good separation of the spectral peaks in the k-space domain, two tagging images with orthogonal tag orientations were generated separately at each time frame. The simulated MR tagging images are shown in Fig. 17. The Fourier transform of the vertical and horizontal tagging images (no flow) is also shown in Fig. 18 respectively. Fig. 18 confirmed that the spectral separation is sufficient for the HARP analysis.

The original HARP was applied on the simulated MR tagging images. Two orthogonal spectral peaks of tagging images were extracted by an elliptic bandpass filter [7], with $r_A = r_B = 5.5035$ rad/cm and $\sigma = 0.2$. Due to the tag alignment, the central frequencies of the bandpass filters were set to the two first harmonic peaks at 0° for a vertical tagging and 90° for a horizontal tagging. The parameters for the bandpass filter were fixed throughout the analysis. This is a reasonable approach since the motion usually occurs for the water flow inside the phantom, and the spectral peaks will not drastically shift off from their original locations. Fig. 19 shows the ground truth velocity

field used to generate the MR tagging images with flows in Fig. 17 (upper right and lower right). Note that the velocity field was truncated out 2% outliers on its magnitudes to improved visualization.

Then, the velocity field was extracted from the tagging images. Since the images provides a motion in two orthogonal directions, it is sufficient to construct an apparent 2D velocity field from the HARP. Fig. 20 shows the velocity field resulted from the HARP analysis. Again, the similar truncation was performed for visualization. By visual comparison, the effect of noise obviously demonstrated in the velocity field resulted from the HARP. It caused the erroneous velocity vectors on the boundary of the phantom. The velocity vectors inside the separation channel of the phantom were also changed in both magnitude and direction. The velocity vectors at the inlet and outlet regions were slightly changed. Furthermore, there were velocity vectors at the very end of the outlet of which their direction was totally opposite to the true velocity field.

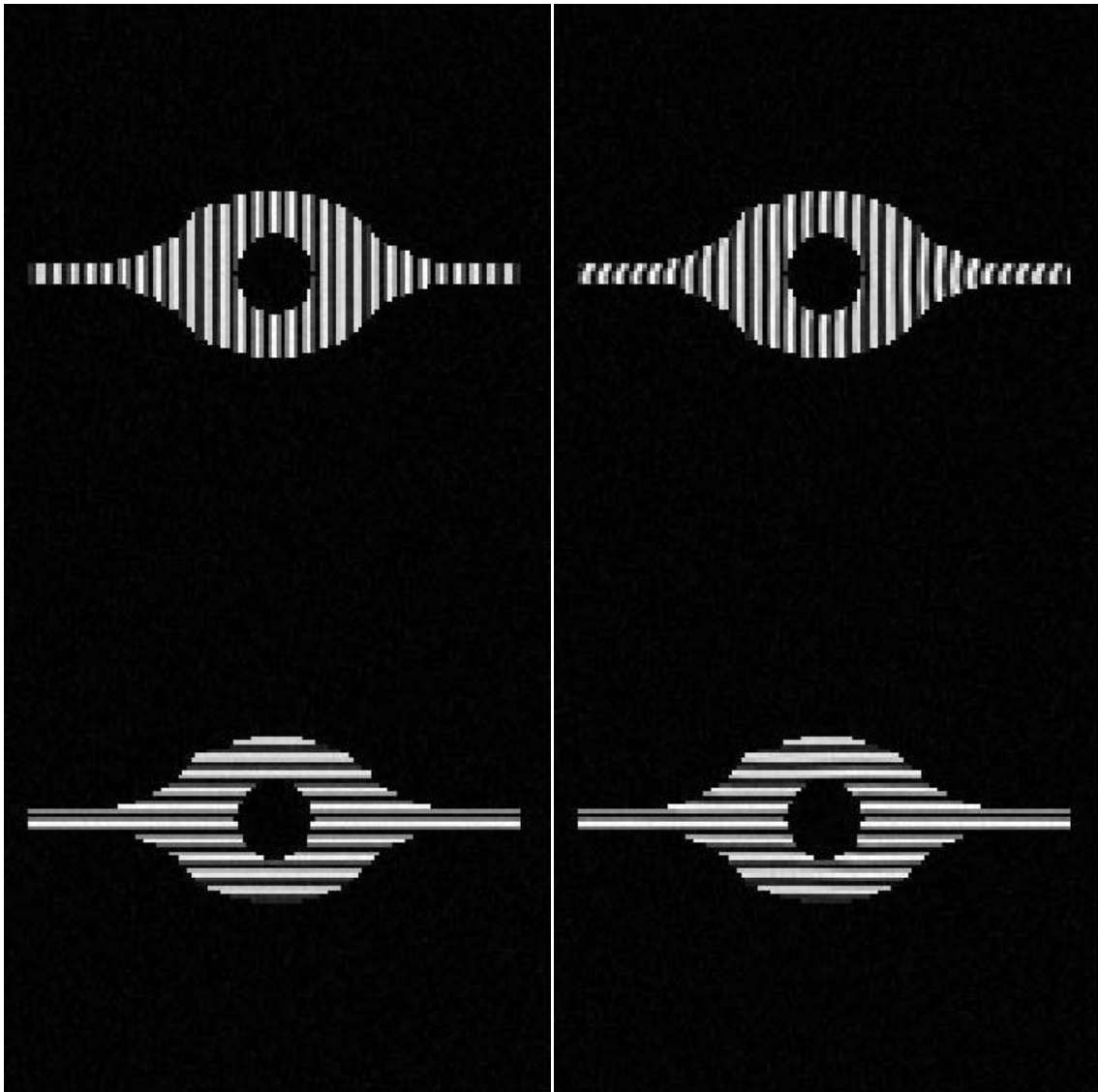


Fig. 17. Simulated MR images using the 1-1 SPAMM tagging pulse with the velocity field obtained from the CFD simulation. (up, left) vertical tagging with no flow; (up, right) vertical tagging with flow; (down, left) horizontal tagging with no flow (down, right) horizontal tagging with flow.

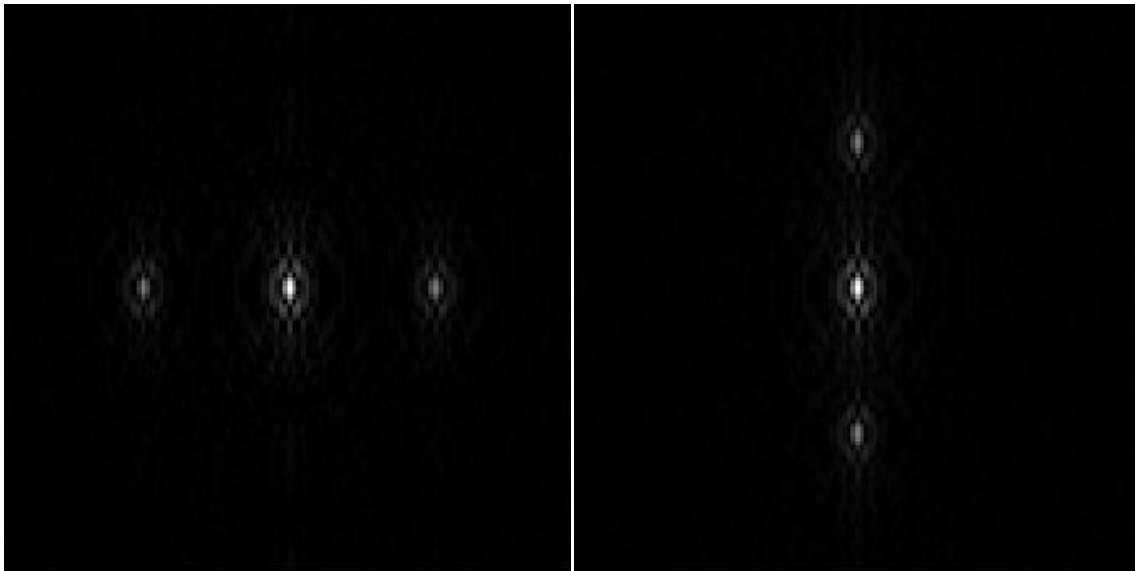


Fig. 18. The Fourier transform of the (left) vertical tagging and (right) horizontal tagging in Fig. 17 (upper, left) and (upper, right) respectively.

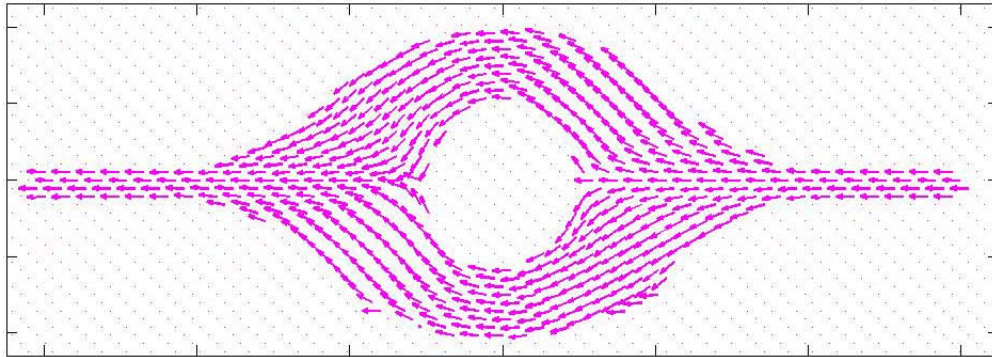


Fig. 19. A ground truth velocity field from the CFD simulation.

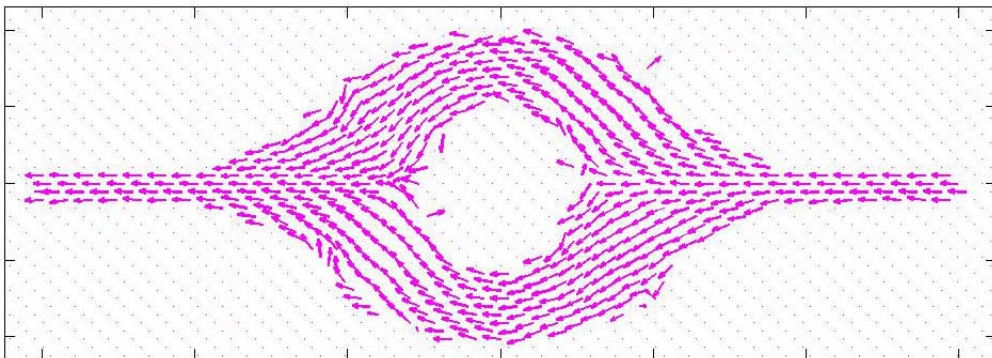


Fig. 20. A velocity field from the HARP analysis from the tagging images in Fig. 17.

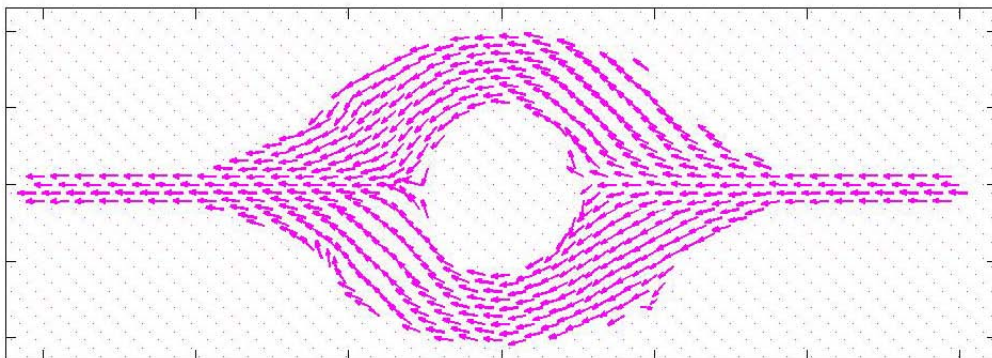


Fig. 21. A regularized velocity field from the velocity field in Fig. 20.

The Proposed Flow Regularization Method for Refinements

The GA/EP algorithm was implemented on MATLAB (The MathWorks, Inc.). Since the study only consider the 2D flow, the vorticity transport equation was used as the fluid governing equation, instead of the Navier-Stokes equation. The algorithm initiated a number of the populations from the smoothed version of the HARP result with the zero mean Gaussian random function and a variance $\sigma^2 = a^2$. The variance was chosen proportional to the maximum velocity at the inlet of the phantom. For reasonable computation time, the population size for the optimization of the 2D velocity components was limited to $N_s = 20$. Furthermore, all the velocity populations were ensured to satisfy the no slip boundary condition, i.e. only the tangential velocity component at the boundary was allowed. The size of each velocity component was set equal to the image size of 128×128 . Weighted coefficients used in the algorithm were 0.1, 1, and 0.0001 respectively. The coefficients have their least weight on the data consistency constraint because of the noise presence in the images. The weighted coefficients were arbitrarily chosen based on the residuals from each constraint of the original velocity field from the HARP analysis. To prevent the velocity field solution that is dominated by the residual from the continuity equation, the program cycled the weighted coefficients of the incompressible flow and the continuity equations when no improvement from the initial weighted coefficient reached at a certain number of generations.

At each generation, the population distribution for elite children, crossover children, and mutation children was portioned according to the number of elite children and

crossover fraction predetermined in the algorithm. In this study, the number of elite children was set to $M = 3$. The crossover fraction was set to $c = 0.8$. Therefore, the number of mutation children was set to $N_{mut} = 3$. The maximum number of generations was set to 500 iterations.

The velocity field was regularized by the fluid dynamics equations and the data consistency condition until the residuals were minimized. The minimum value of the residuals for termination criteria was set to zero (or no error), but it was never reached in the analysis. The program only exited when it has no improvement for a certain number of iterations, with the tolerance set to $5e^{-5}$. In practice, the algorithm therefore provides the solution that compromises the residual function because the minimum error is difficult to achieve. The 2D velocity field resulted from the HARP with the proposed algorithm is shown in Fig. 21.

The result from the proposed method shows a visual improvement from that of the original HARP in Fig. 20 even though not all of the velocity vectors are perfectly corrected. The magnitude plots of the velocity fields from the CFD, original HARP, and the proposed regularized method were shown in Fig. 22-24 respectively. It was observed that the magnitude of the velocity field from the original HARP was generally in an agreement with that from the true velocity field at the inlet and outlet regions, but there were higher magnitudes at the separation channel inside the phantom. However, the

velocity magnitudes inside the separation channel from the regularization method were improved and in better agreement with the true velocity field. Yet, its velocity magnitudes at the inlet and outlet were slightly underestimated the true velocity magnitudes. This could be possible for the original HARP to outperform the regularization method when a simple flow profile (only straightforward flows) is studied. The velocity estimate from the regularization method still needs to compromise the overall data consistency condition.

The zoomed-in velocity fields of the CFD simulation, the original HARP analysis, and the regularization method are shown in Fig. 25 – 27 for the separation channel, the outlet, and the inlet, respectively. An obvious improvement from the regularization method as described above is visually observed. The wrong velocity direction at the outlet from the original HARP method in Fig. 26 was also clearly observed.

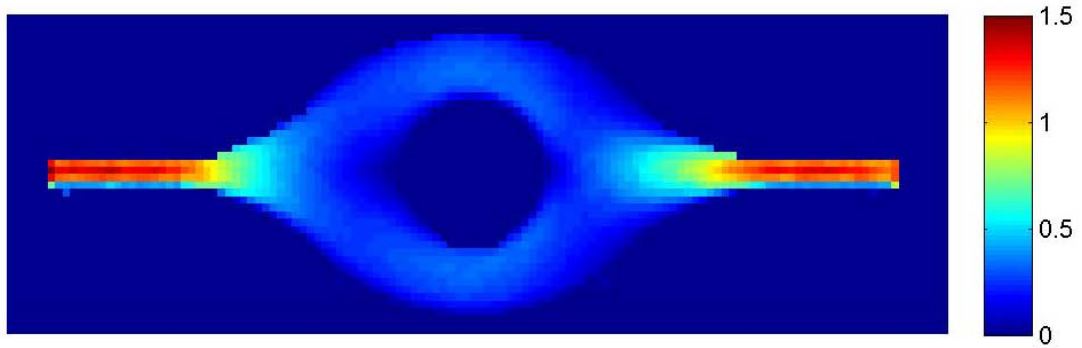


Fig. 22. A magnitude plot of the CFD velocity field in Fig. 19.

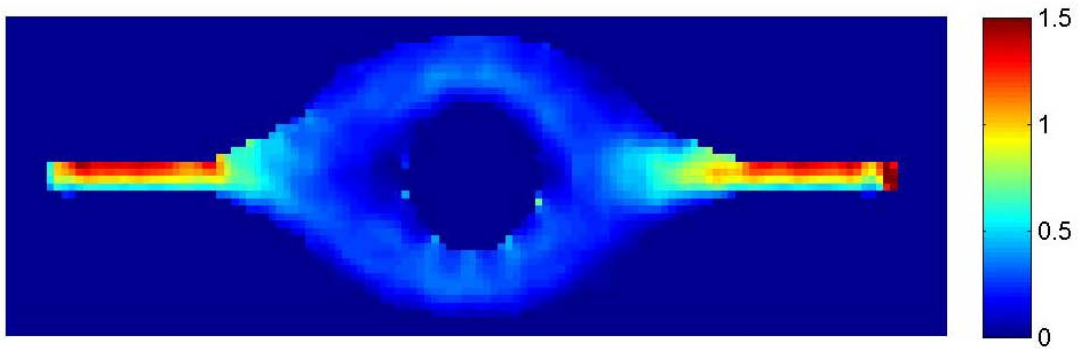


Fig. 23. A magnitude plot of the original HARP velocity field in Fig. 20.

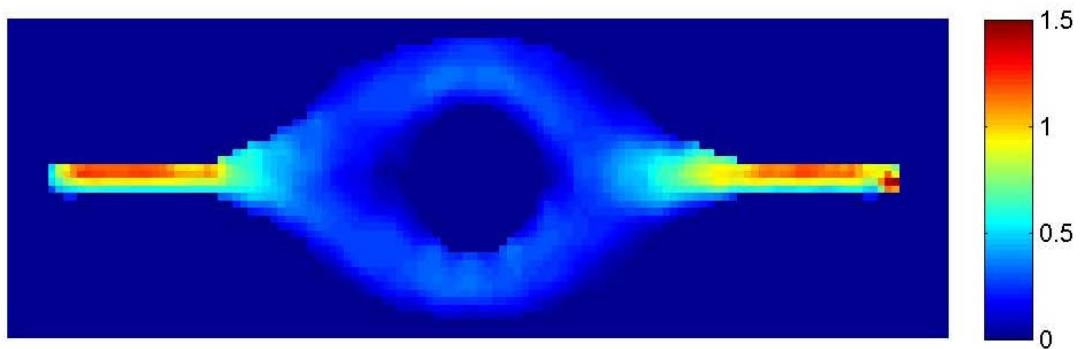


Fig. 24. A magnitude plot of the regularized HARP velocity field in Fig. 21.

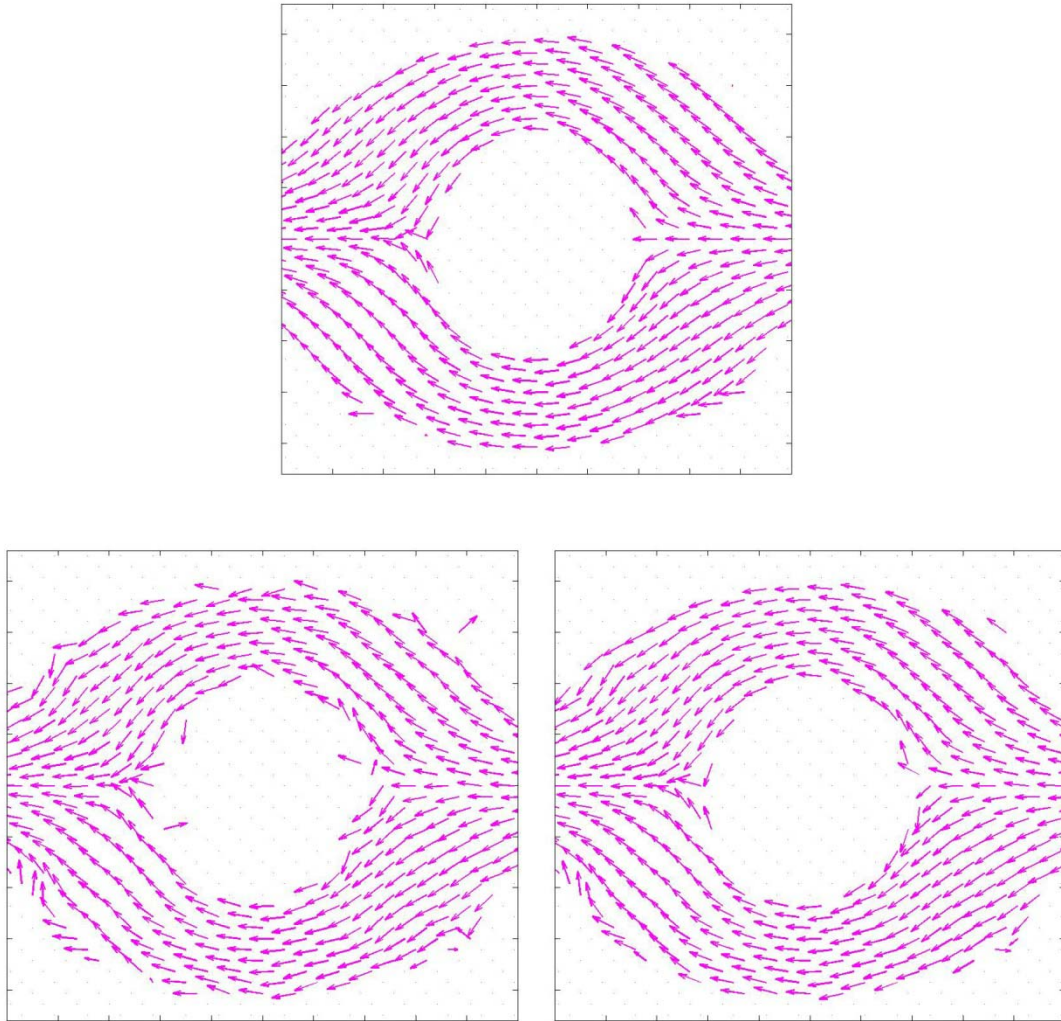


Fig. 25. A velocity field comparison at the separation channel among (up) the CFD simulation, (left) the original HARP, and (right) the HARP-GA.

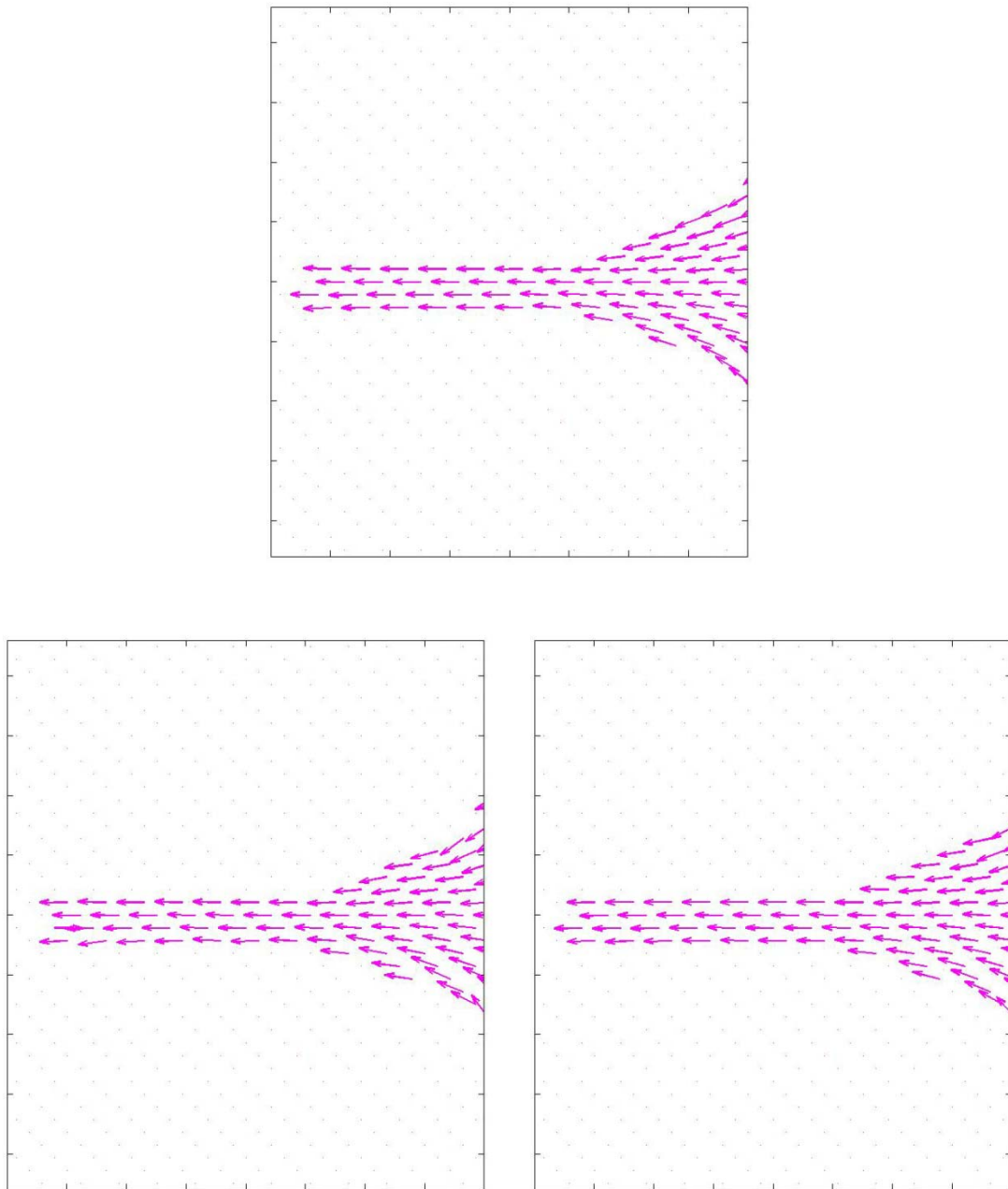


Fig. 26. A velocity field comparison at the outlet among (up) the CFD simulation, (left) the original HARP, and (right) the HARP-GA.

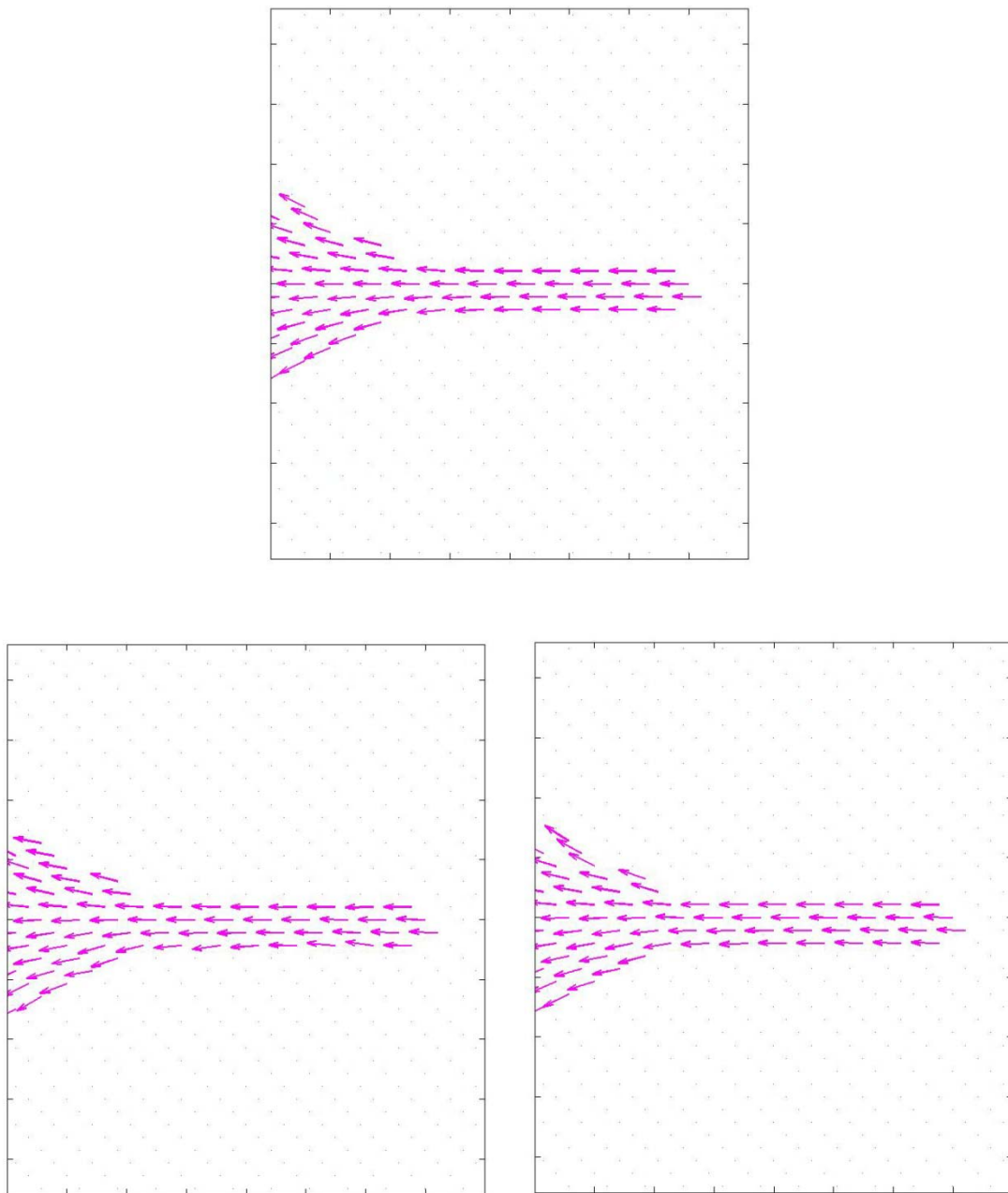


Fig. 27. A velocity field comparison at the inlet among (up) the CFD simulation, (left) the original HARP, and (right) the HARP-GA.

Quantitative Comparison for the Proposed Regularization Method

The mean absolute error (*MAE*) over the entire phantom was used to quantify the improvement by the proposed method. The metric is mathematically given by:

$$MAE = \frac{\sum_{\epsilon \in D} |\mathbf{u}_{\text{method}} - \mathbf{u}_{\text{CFD}}|}{N}$$

where $\mathbf{u}_{\text{method}}$ is the velocity field of the original HARP or the proposed method; \mathbf{u}_{CFD} is the true velocity field from the CFD simulation; D is the region of interest (the entire phantom in this case); and N is the total number of velocity vectors inside the region of interest. The MAE is summarized in the Table 1. The mean absolute difference is 0.0558 cm/sec and 0.0424 cm/sec for the original HARP method and the proposed regularization method respectively. This is approximately a 24% improvement from the original method.

Real MR Flow Experiments

The HARP Analysis on the Real Data

MR tagging images were acquired from the flow phantom using a 1-1 SPAMM pulse sequence with the spin echo acquisition by a volume coil in the 40cm/4.7T MR scanner as described in the method section. 22.1% g/g glycerol-water mixture was used in the experiments that can prolong the signal decay of the spin-tags in an order of T_1 . The

gravitational flow was used at the mass flow rate of 20 cc per minute. The MR tagging pulse sequence was prescribed with the following imaging parameters: TR = 650 msec; TE = 30 msec; FOV = 137×137 mm²; Matrix size (FE×PE) = 128×128. The SPAMM tagging pulse was performed with the 12.6 msec duration, and the tag frequency was set to 2.4 cm⁻¹ on each orientation. 100 and 300 msec delays were used to allow the tag evolution before the data sampling. Because a steady flow was imaged, this finally resulted in the 200 msec time resolution between the acquired images. Two orthogonal tag orientations (vertical and horizontal) were used to provide 2D tag motion information similarly to the MR simulation. The imaging was performed with a single average for the data acquisition.

TABLE 1

THE MEAN ABSOLUTE ERROR COMPARISON BETWEEN THE ORIGINAL
HARP AND THE REGULARIZED METHOD

Analysis Methods	Mean Absolute Error	
	Simulated MR Data	Real MR Data
HARP	0.055789	0.317565
Regularized HARP	0.042416	0.283379

The acquired tagging images with are shown in Fig. 28. The noise presence is clearly observed from the data, however, there were tag distortion and blurring observed at the phantom boundaries and also inside the phantom channel. The tag distortion inside the phantom channel was possibly due to the field inhomogeneity. The tag blurring was possibly due to the relaxation of the tag spins and the signal cancellation from the new flow spins. The tag blurring existed at the later acquisition even though the tag delay was kept short.

The HARP algorithm was applied to the acquired MR tagging data similarly to the analysis used in the previous MR simulation. However, two orthogonal spectral peaks of tagging images were extracted by an elliptic bandpass filter [7], with $r_A = r_B = 6.8794$ rad/cm and $\sigma = 0.2$. The velocity field and its magnitude plot resulted from the original HARP are shown in Fig. 29. The magnitude truncation was applied on the velocity field plot for better visualization.

The velocity field resulted from the original HARP shows velocity errors at the boundaries, and its magnitude plot inside the flow channel was not smoothly changed. This is quite different from the error results observed in the simulation study where the noise is only the possible source of errors. Therefore, this possibly indicates that other factors, such as the field inhomogeneity and the tag blurring, than noises in the real data also adversely affect the HARP analysis. The inflow toward the boundary of the circle at center might indicate the flow in the third dimension that has not been taken into account. The misdirection of the flow at the inlet is possibly resulted from the relatively

high flows to the chosen tag period, and also the signal destruction from the new flow spins that are not tagged during the tag preparation.

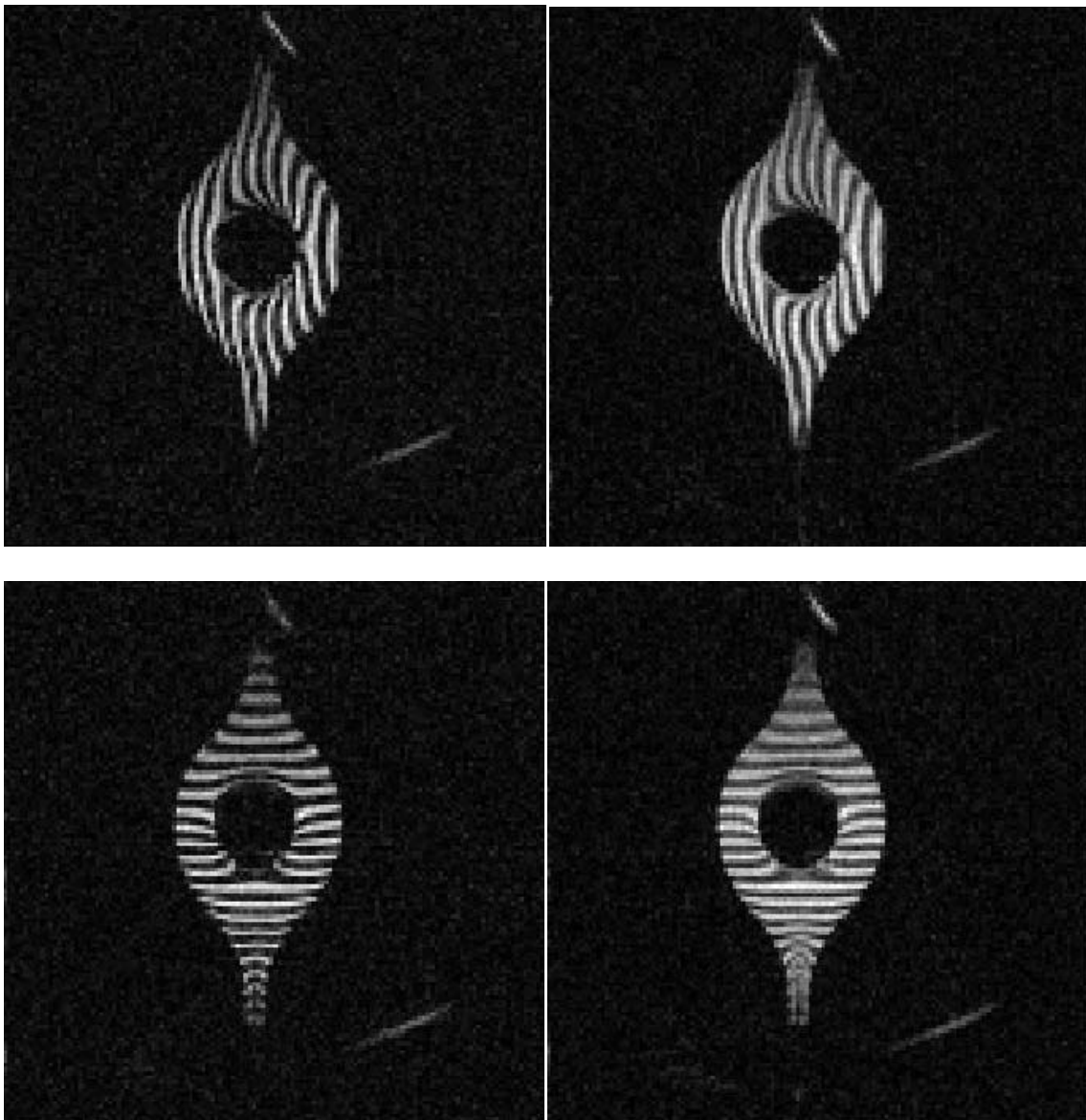


Fig. 28. Two orthogonal tagging orientation images (1 average) acquired with (left) 100 msec and (right) 300 msec tag evolution delay.

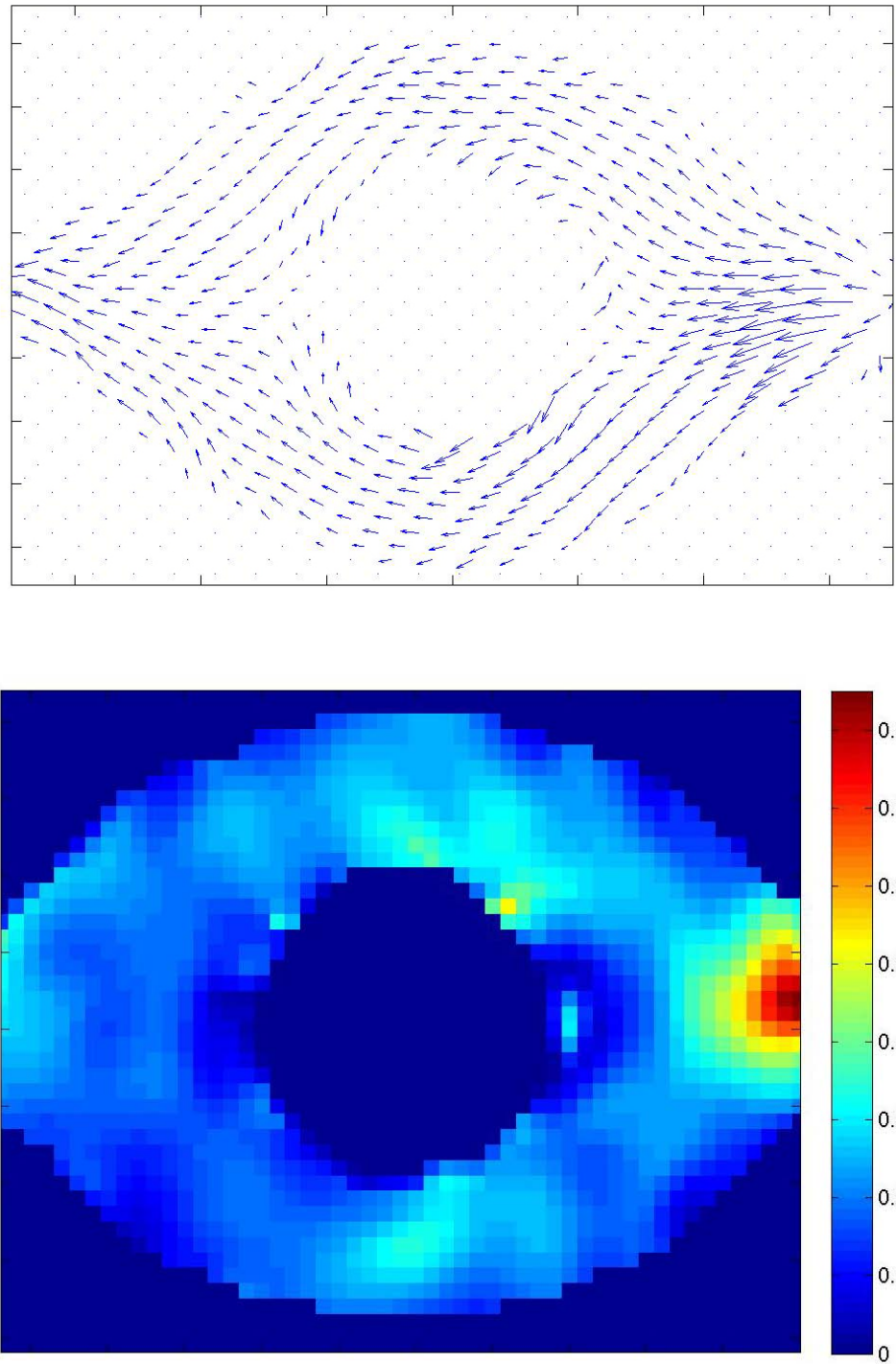


Fig. 29. The velocity field and its magnitude plot from the original HARP analysis on the real MR data.

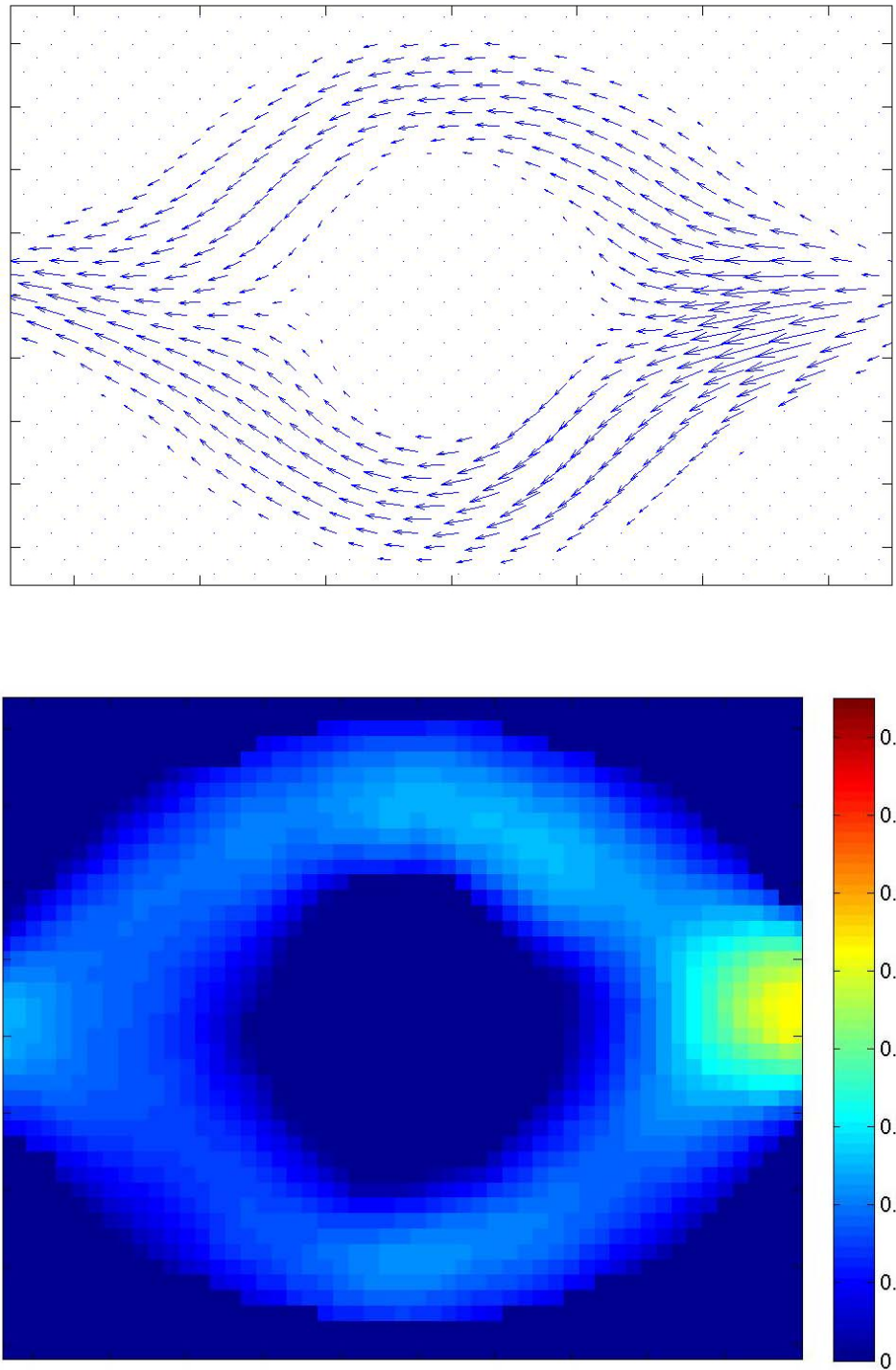


Fig. 30. The regularized velocity field and its magnitude plot from the original HARP analysis on the real MR data.

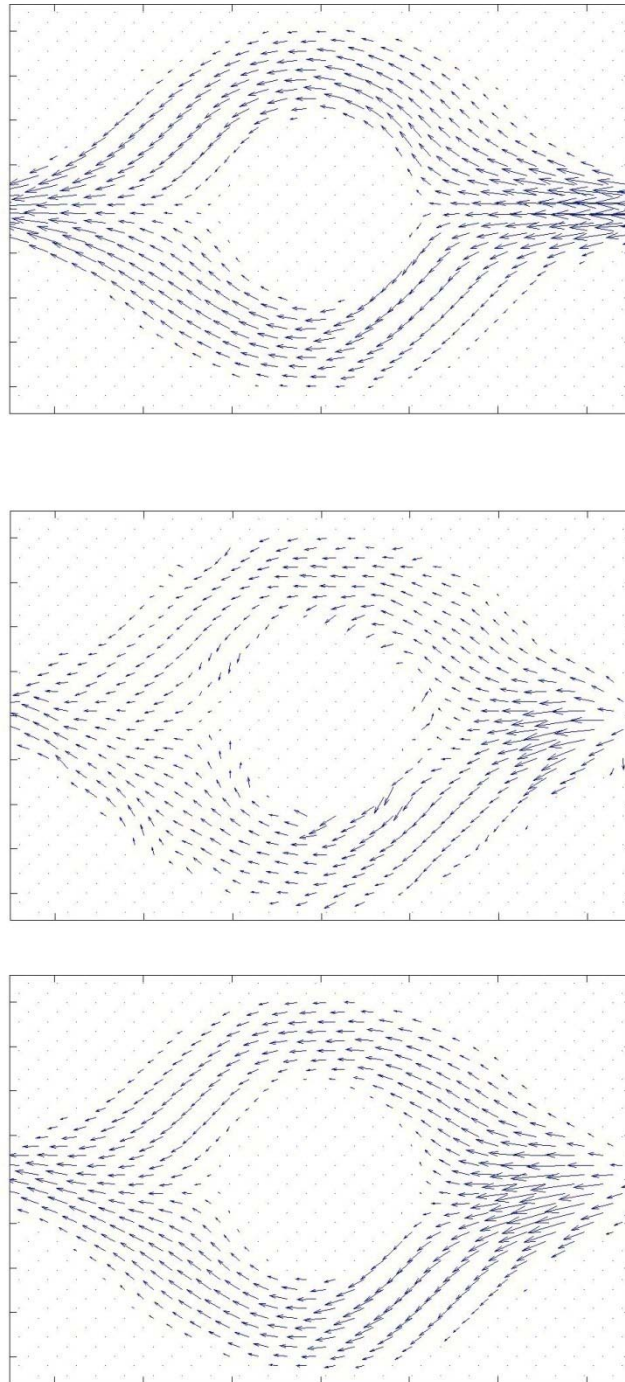


Fig. 31. A velocity field comparison among (top) the CFD simulation, (middle) the original HARP, and (bottom) the regularized HARP.

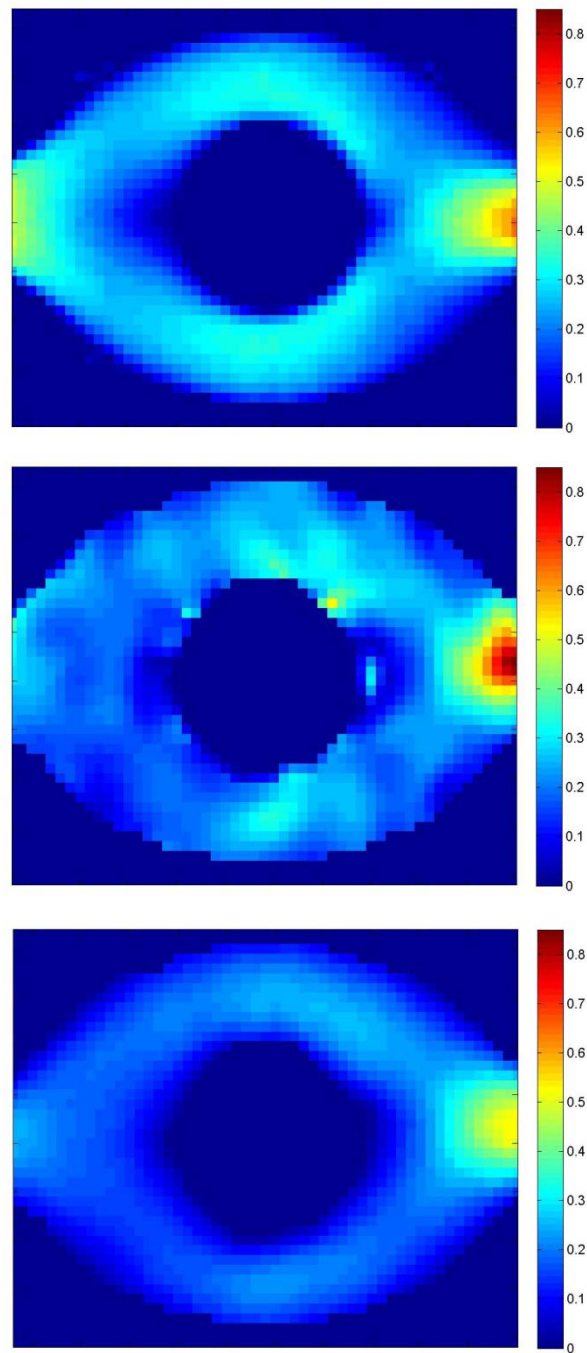


Fig. 32. Magnitude plots of the velocity fields among (top) the CFD simulation, (middle) the original HARP, and (bottom) the regularized HARP.

The Proposed Flow Regularization Method for Refinements

Similarly to the flow simulation, the HARP result of the real MR data was used in the proposed regularization method. All the analysis parameters for the regularized method were kept the same as used in the simulation study. The velocity field and its magnitude plot resulted from the regularized method were shown in Fig. 30. Fig. 31 shows the velocity field comparison between the original HARP and the regularized method on the same data. The velocity field from the CFD simulation was also put as the theoretical basis for the quantitative comparison. The magnitude plots corresponding to Fig. 31 are shown in Fig. 32.

Qualitatively, the velocity field obtained from the regularized method provides improved velocity fields than those of the original HARP. In the other words, the method demonstrates more continuity and reasonable velocity field. The magnitude plot also shows the more smoothness in the velocity change. It was also noticed that velocity magnitudes on both side of the separated channel are not totally symmetric. This is because the slight off-symmetry of the flow phantom from the hand manufacturing. It is also noted that the proposed method obviously correct the velocity result at the boundary areas due to the no slip boundary condition incorporated into the regularization.

A quantitative comparison between the two velocity fields using the CFD velocity field as a reference demonstrated the improvement of the regularized method. As shown in the Table 1, the MAE of the regularized method has approximately 11% improvement over that of the original HARP. The MAEs of the real MR data are relatively large compared to those of the simulation study. This could possibly be due to the asymmetry

flow from the real phantom and the experimental error from the mass flow rate control during the flow setup.

D. Conclusion and Discussions

The proposed regularization method for the MR flow quantification, specifically the HARP analysis, has demonstrated its usefulness to improve the velocity field both quantitatively and qualitatively. The flow simulation might be proven to be useful since the velocity ground truth can be used for the comparison.

The flow simulation demonstrates that the proposed method can improve the velocity field from the noisy data by approximately 24% in the MAE sense. The original HARP method can result in velocity errors for both magnitude and direction due to the noise data. The original HARP seems to work well when the flow has well-defined characteristics, i.e. laminar, slow, and straightforward flows as observed from the velocity field at the inlet and outlet of the phantom. However, the improvement is expected to be higher if the velocity vectors are more distributed as shown in the separation channel of the phantom. In fact, the flow situation in the separation channel is more likely to happen in the real flows study. This then shows the major advantage of the proposed method.

In the real MR data, the proposed method also demonstrates the qualitative improvement over the original HARP method. More flow continuity and magnitude change on the velocity field were achieved. Even though the actual ground truth was not

achieved, the quantitative comparison between the two methods with the CFD simulation also showed the improvement of the proposed method over the original HARP by approximately 11% in the MAE sense. This still indicates that the proposed regularization method is useful to a flow study.

Nevertheless, there are still many challenges for possible future research directions that can improve the proposed method. First, all parameters used in the optimization procedure are ad-hoc and dependent on the flow settings such as the flow geometry, the boundary conditions, and the type of flows. All of these affect the selection of ‘optimal’ parameters in the optimization such as the weight coefficients for the residual function, random methods at each generation step in the optimization algorithm, and the suitable number of population, etc. Improper selection of these parameters can lead to long processing time to find the optimal solution or even result in an incorrect solution. At this stage, the method is expected to be performed by off-line processing due to the parameter selection. Second, a method to reduce the processing time is also desired. It is clearly understandable that the genetic algorithm heuristically searches for the optimal solution in a very large searching space for the flow study. An approach to reduce the search domain for the algorithm such as local area optimization or parallel processing might help improve the running time and allows faster analysis. Finally, the analysis should be extended for a 3D flow study to fully account for the out-of-plane flow, which will complete the study of a real flow.

CHAPTER VI
A VALIDATION OF THE HARP METHOD
FOR THE MR FLOW QUANTIFICATION

A. Rationale of the Work

A quantification using the HARP analysis for fluid flow studies has been rarely validated although it has been widely used for cardiac motion. In the past, the MR flow quantification by MR tagging was performed to track those markers by the time-of-flight or optical flow methods [70, 72, 292-294]. However, the HARP analysis is more promising than the time-of-flight methods because it can provide dense displacement from the images [6, 7, 74] with the rapid processing time and minimal manual intervention. Our fluid flow studies [295, 296] are relatively new for the HARP analysis to quantify the fluid flows. Also, no ground truth was obtained for validation in the works. Therefore, it is needed to validate the HARP analysis for its usefulness with other flow quantification methods.

Besides MRI, the optical imaging based on particle flows can be used to provide a flow data with a very good temporal resolution and also allows an experimental comparison with MRI for flow quantification at a similar resolution. For example, it was used to quantitatively compare cross-modality with PCMRI for a steady flow in an extracardiac total cavopulmonary connection (TCPC) [297]. In addition, it has been widely accepted and utilized for numerous applications in fluid mechanics [232-237],

aerodynamic industries [238, 239], jet industries [242, 245], microfluidics [254, 255, 257], and drug mixing [256, 298, 299]. The method uses a statistical approach, specifically the cross-correlation, to quantify a displacement within a small interrogation window of the flow image. A presence of special features like particles on the image is required for the method to estimate the displacement. The method is then referred as the Particle Image Velocimetry (PIV).

Furthermore, the CFD simulation can provide a general idea for the ‘ground truth’ of a velocity field inside an interested geometry. This helps relax a major problem of the flow quantification work, i.e. a lack of the true velocity field. For instance, the CFD was used to compare with PCMRI for the laminar flow in a expansion-contraction-expansion-contraction pipe system [118]. The velocity field from the CFD simulation will allow the study to quantitatively compare the experimental results obtained from both MRI and PIV.

B. Methods

The MR flow quantification method using the HARP analysis was validated its result with the conventional optical flow imaging based on PIV and the CFD. The validation was performed experimentally by quantifying the velocity fields of steady flow experiments at 20 cc per minute mass flow rate using both the HARP and PIV. The results from both methods were used to compare with the CFD velocity field qualitatively and quantitatively. Since the methodology for the CFD simulation and MR

tagging used in this study was previously described in the previous chapter when both of the simulated and real MR tagging data were used for the proposed regularization method. The explanation for their analysis and procedure are referred to the method section in the previous chapter.

Flow Phantom and Experiment Setups for PIV

A flow phantom with separated channels as illustrated in Fig. 33 was used to collect the flow data for the PIV and MRI experiments. The phantom was actually built from the design in Fig. 12. The background of the phantom was painted in black to provide the best contrast with the particle color for the PIV experiments. A scale unit (in mm) was attached to the top of the phantom for the actual coordinate reference in the analysis. The top of the phantom was covered with the transparency in order to allow an optical imaging from the top view. The physical size of the phantom is $7.62 \times 12.7 \times 0.5 \text{ cm}^3$ ($3 \times 5 \times 0.2 \text{ in}^3$), which is the same as the design in Fig. 12.

The flow setups similarly to Fig. 13 in the previous chapter were set and controlled for the same conditions as close as possible for the cross modality comparison. Gravitational flows with a steady flow of a 20 cc per minute mass flow rate were controlled by the valve and an omega FL-213 rotameter (3 – 300 cc/min with $\pm 5\%$ reading accuracy and $\pm 1\%$ reading repeatability). Due to a need of the particles for the PIV, micro-particles were suspended in the mixture reservoirs. However, the particles were removed from the mixtures and not used for MR flow experiments.

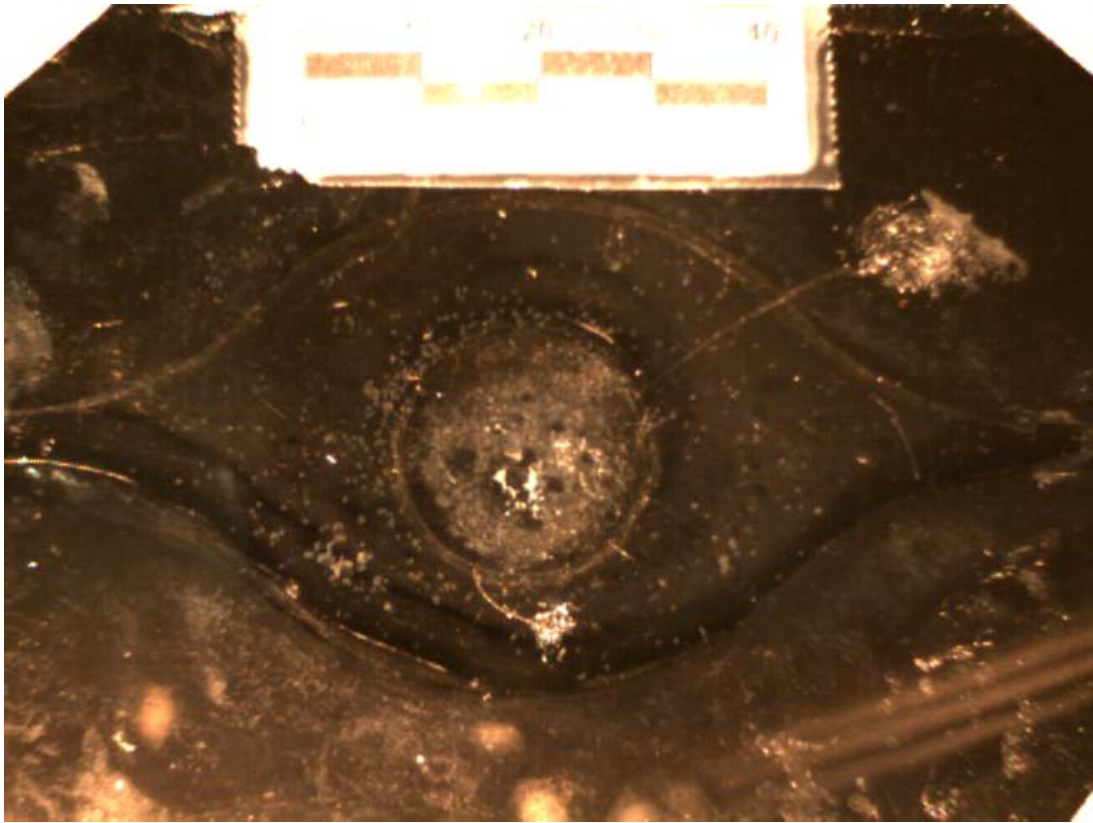


Fig. 33. A flow phantom for PIV and MRI experiments.

Particle Image Velocimetry

The method captures and quantifies fluid flows from suspended particles flowing along the fluids using a high-speed CCD camera. Therefore, the method assumes that the particles do not affect the property of the real fluid flows, and its motion can be used to refer the flow displacement. Displacement of particles between two PIV images can be calculated using pattern matching algorithms, specifically a cross-correlation [249-253, 263-267, 300].

The cross-correlation method quantifies a displacement between two images by dividing the images into sub-regions, also called interrogation windows. Each sub-region of the first image is matched with the corresponding sub-window of the other image by finding the minimum Euclidean distance within the possible overlaps [300]. Let us define a pair of images I_1, I_2 acquired at the time separation of Δt . The images are divided into several sub-windows $I_1^{i,j}, I_2^{i,j}$ of size $M \times N$. $I_1^{i,j}$ and $I_2^{i,j}$ denote the i^{th} row and j^{th} column sub-windows of the images I_1, I_2 respectively. The Euclidean distance between the two sub-windows over an overlap (d_x, d_y) is defined as:

$$\begin{aligned} D_e(d_x, d_y) &= \sum_{m=0}^{M-1} \sum_{n=0}^{N-1} \left[I_1^{i,j}(m, n) - I_2^{i,j}(m - d_x, n - d_y) \right]^2 \\ &= \sum_{m=0}^{M-1} \sum_{n=0}^{N-1} I_1^{i,j}(m, n)^2 - 2I_1^{i,j}(m, n)I_2^{i,j}(m - d_x, n - d_y) + I_2^{i,j}(m - d_x, n - d_y)^2 \end{aligned}$$

The second line of the equation expands the Euclidean distance to obtain the alternative to the minimization. Assume I_2 is uniformly distributed, it is reduced to minimize only the middle term, which is the cross-correlation between the two sub-windows. Therefore, the algorithm finds the overlap (d_x, d_y) that maximizes:

$$C(d_x, d_y) = \sum_{m=0}^{M-1} \sum_{n=0}^{N-1} I_1^{i,j}(m, n)I_2^{i,j}(m - d_x, n - d_y)$$

The matching algorithm using this correlation function is preferable because it can be implemented by the FFTs for fast processing. In general, the two sub-windows can be chosen in an overlap fashion. The method can also be used multiple times (so called multi-pass) with different sub-window sizes to improve the displacement calculation.

Affine Registration for Cross Modality Comparison

Images obtained from different imaging modalities can be in different perspectives. Therefore, the images are required to be registered before a comparison. For simplicity, the images from different modalities are assumed to hold for the perspective transformation, i.e. a line is still preserved as a line in different imaging modalities. Then, the affine transformation can be used to register the two images from different imaging modalities by:

$$\begin{bmatrix} \dot{x} \\ \dot{y} \end{bmatrix} = \begin{bmatrix} a & b \\ c & d \end{bmatrix} \begin{bmatrix} x \\ y \end{bmatrix} + \begin{bmatrix} e \\ f \end{bmatrix}$$

where a, b, c, d, e, f are the affine transformation coefficients; x, y are the spatial coordinates of the first imaging modality; and \dot{x}, \dot{y} are the spatial coordinates of the other imaging modality.

C. Results

The data from both the PIV and the HARP analysis were analyzed for a comparison of their velocity fields. Since the true velocity distribution inside the flow phantom was unknown, the velocity field from the CFD simulation at the same mass flow rate was provided for the quantitative comparison. Since all the experiments were performed with the same liquid mixture at the 20 cc per minute mass flow rate, the velocity fields from the CFD simulation and the HARP analysis in the previous chapter can be used for this validation.

Particle Image Velocimetry

355 – 425 micron diameter plain polystyrene particles (Polysciences, Inc., Warrington, PA) were suspended in the glycerol–water mixtures to produce particle flow images. During imaging, the flowing particles at all depths inside the phantom were illuminated from the top angle with 26 Watts GE CFL light bulbs. The particle flows were captured by a high speed Prosilica GC640C CCD camera with the imaging speed of 99.562 frames per second and an exposure time of 10,000 microseconds. Due to the physical design of the phantom, the CCD camera was vertically placed approximately 3 cm above the phantom. Ten consecutive 493×659 color images of the particle flows with the image area of $4.22 \times 6.24 \text{ cm}^2$ were acquired by the NI Vision Assistant (National Instruments Corporation, Austin, TX) software interface to the CCD camera.

Due to the small field of view for the PIV, the imaging was taken at the separation channel. Fig. 34 shows an example of the 35th PIV image from the PIV data. Dense

particle flows were observed on the PIV image. This is to ensure a sufficient number of particles for the displacement estimation by the correlation approach. It was also observed that particles does not flow throughout the phantom channel, especially particle flows at the inlet and boundary areas. Occlusion was observed at the bottom of the center circle and the boundary near the inlet. The velocity fields of two data sets were extracted by the correlation algorithm, with the window size of 32×32 pixels and 75% window overlap. Masks for the image data were manually generated for the correlation computation. The velocity fields from adjacent PIV images were extracted for the entire PIV data. Because of the steady flow, the final velocity field was averaged and illustrated in Fig. 35, with the corresponding magnitude plot. The velocity filed from the PIV can provide reasonable direction since its vector directions matched to the real flows observed during the optical imaging experiments. The magnitude plot shows irregularity and has higher velocities around the phantom boundaries. A sudden drop in the velocity magnitude just below the center circle of the separation channel was observed. This is possibly due to the occlusion on the PIV images.

Affine Registration for Velocity Field Comparison

Fig. 36 shows the velocity field and its magnitude plot extracted from the MR image data using the HARP analysis. The plots are on the coordinates of the MR measurement. It is easy to see that the velocity field was calculated at different image orientations and sizes than that of the PIV. This prevents a direct comparison of the velocity fields between the two methods. Therefore, it is required to register the velocity fields from the

different spatial coordinates before the comparison. In this study, there were three possible velocity fields to be compared: 1) the CFD velocity field; 2) the PIV velocity field; and 3) the HARP velocity field. The velocity field from the CFD was also used as a theoretical ground truth to provide a quantitative comparison. The spatial coordinate of the PIV method was used as the reference for the affine registration to the other two methods. The study assumed that the affine transformation relationship holds for all quantification methods.

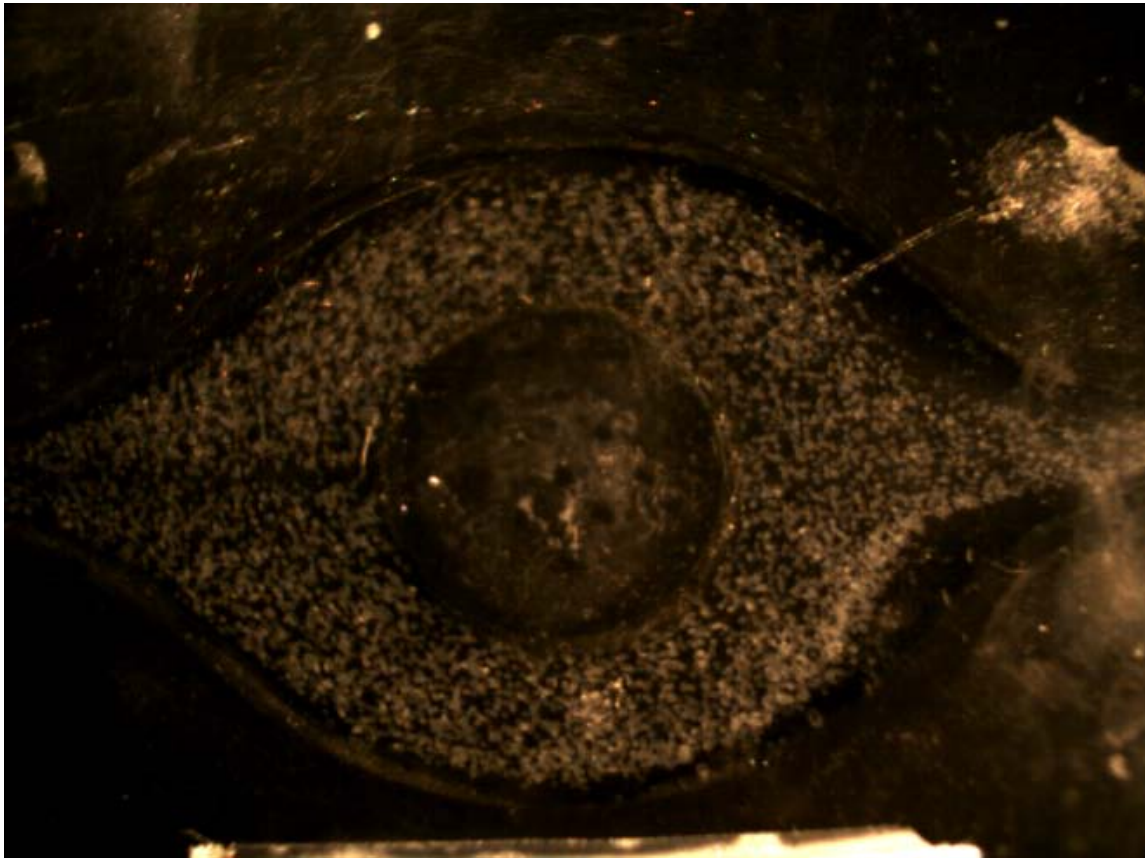


Fig. 34. An example of a PIV image.

The registration was achieved by matching the same marker points among these spatial coordinates. In an error-free case, at least three points are required to find the mapping between two different coordinates. In this study, four marker points with 90° separation were selected from the perimeter of the center circle since they were well present on the images. All of these four marker points were used in the affine registration to provide the 6 affine transformation coefficients (or the mapping coefficients). The registration was formulated as an optimization problem as:

$$\arg \min_{a,b,c,d,e,f} \|\dot{\mathbf{x}} - A(\mathbf{x}, a, b, c, d, e, f)\|^2$$

where $\dot{\mathbf{x}}$ is the spatial coordinates of the velocity field from the CFD or the HARP analysis; \mathbf{x} is the spatial coordinates of the velocity field from the PIV; $A(\mathbf{x}, a, b, c, d, e, f)$ is the affine transformation on the spatial coordinates being registered with the affine transformation coefficients a, b, c, d, e, f as defined in the method section. The optimization was solved by a sequential quadratic programming (SQP) method [301-304] provided by MATLAB (MathWorks, Inc.). The initial guess for the mapping coefficients were computed from the average of the mapping coefficients from different combinations of three point selection out of the four point markers. The mapping coefficients for the HARP-PIV and the CFD-PIV are summarized in the Table 2.

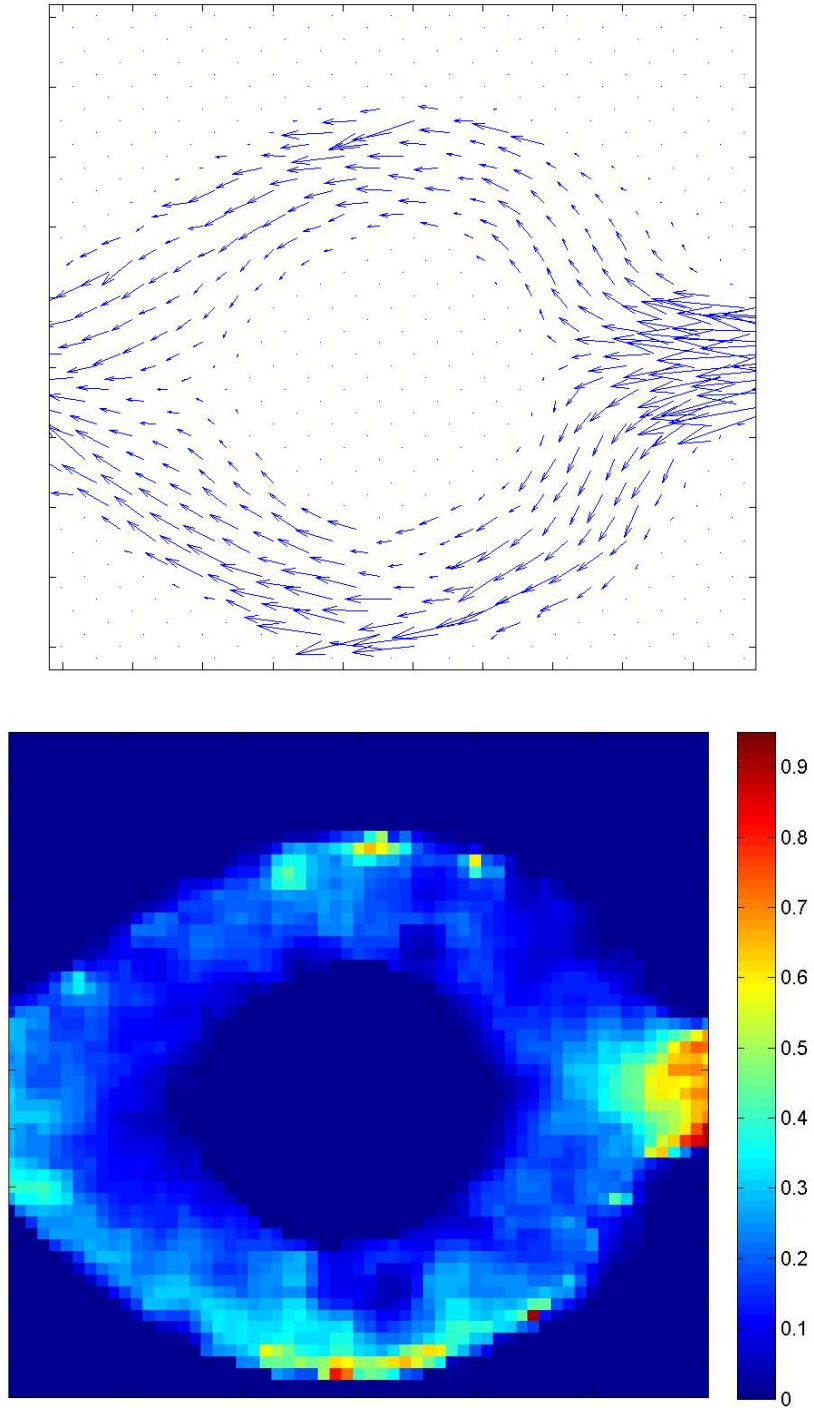


Fig. 35. Extracted velocity fields from the correlation method (PIV) at the separation channel of the phantom.

TABLE 2

AFFINE TRANSFORMATION COEFFICIENTS FROM THE MINIMUM SQUARE
ERROR OPTIMIZATION

Imaging Modalities	<i>a</i>	<i>b</i>	<i>c</i>	<i>d</i>	<i>e</i>	<i>f</i>
HARP – PIV	-1.0510	-0.0547	-0.0494	1.0231	-0.5702	1.2740
CFD – PIV	-0.0157	1.0844	1.1051	-0.0001	0.9588	-0.1819

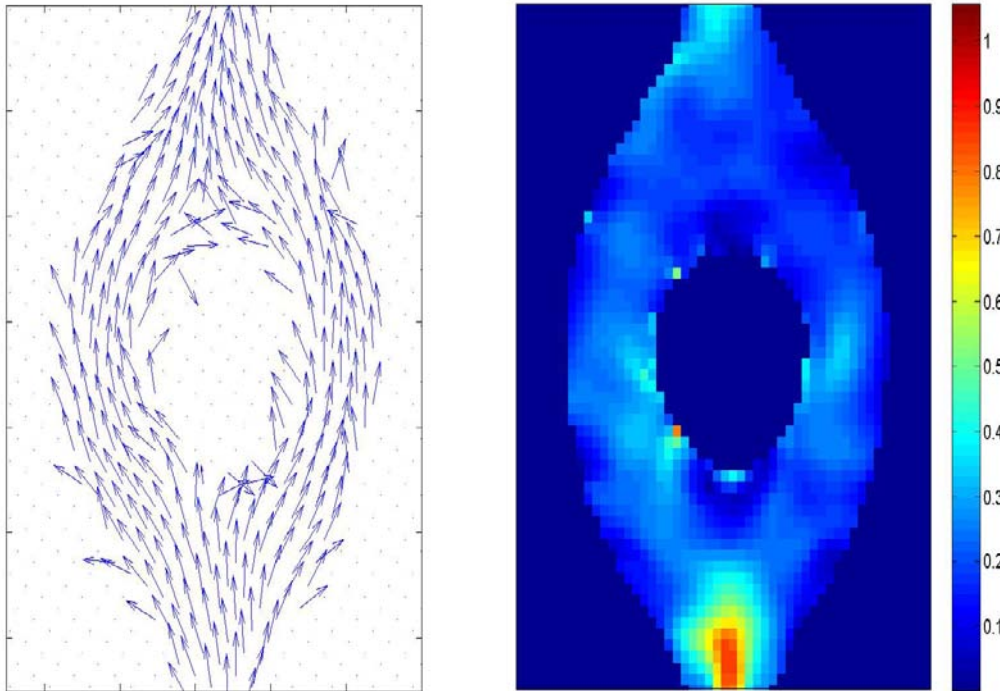


Fig. 36. (left) A velocity field and (right) its magnitude plot on the original coordinates of the original HARP analysis.

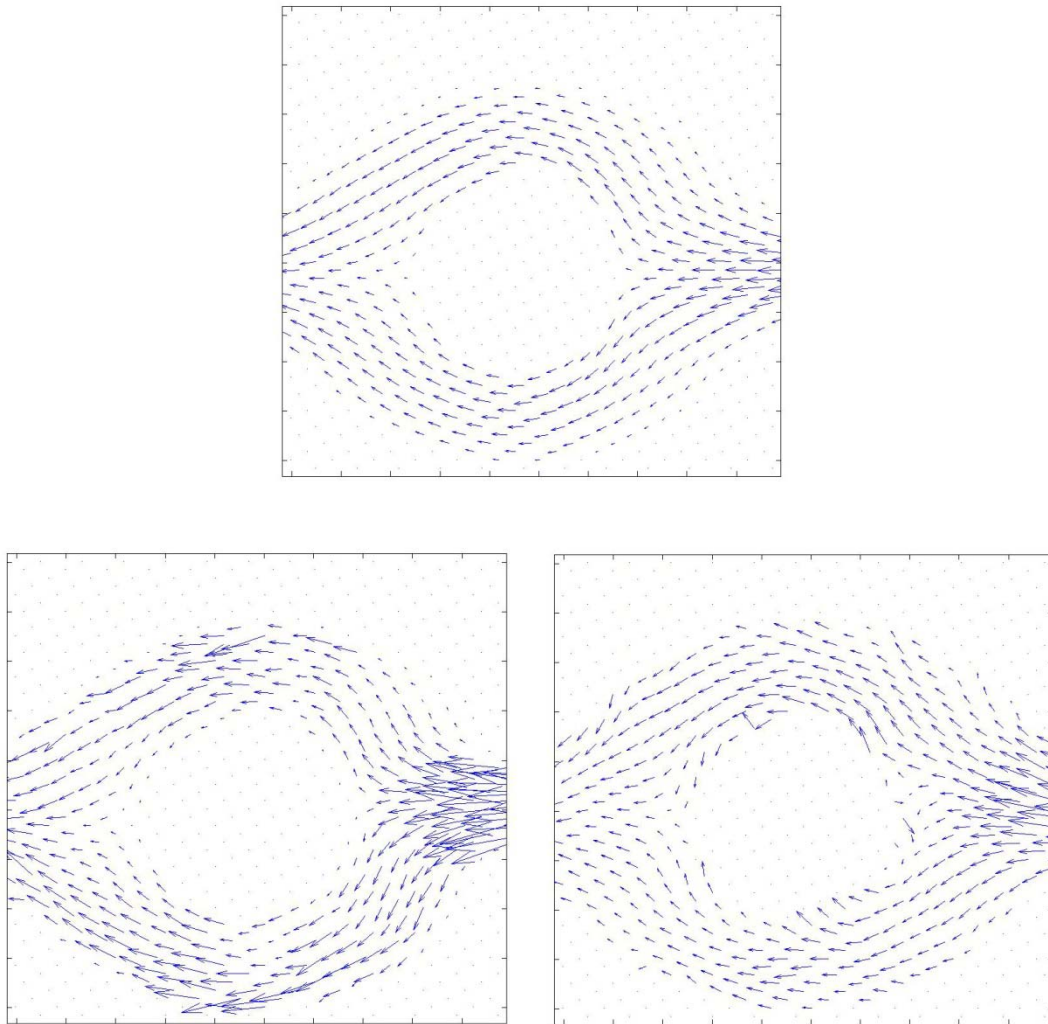


Fig. 37. A velocity field comparison among (top) CFD, (left) PIV, and (right) HARP.

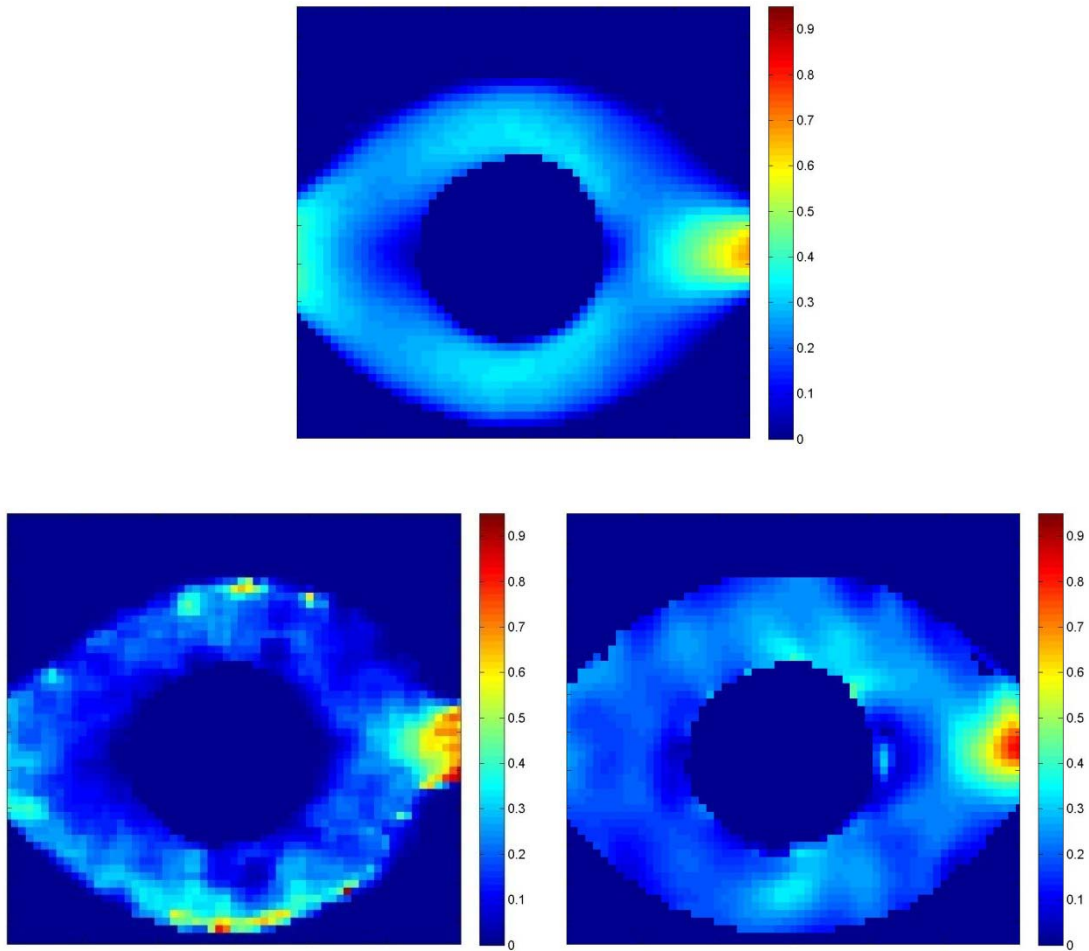


Fig. 38. A velocity magnitude comparison among (top) CFD, (left) PIV, and (right) HARP. corresponding to Fig. 37.

Velocity Field Comparison

After the registration, the spatial coordinate of the velocity fields of the CFD and HARP were transformed onto the PIV's coordinates. All the coordinate points after the affine transformation might not be exactly on the grids. Therefore, a linear interpolation of the velocity magnitude was utilized for an estimation of the 2D velocity components.

The velocity fields at the separation channel of the flow phantom after the interpolation are shown in Fig. 37. The corresponding magnitude plots are also shown in Fig. 38. Qualitatively, it was observed that the directional information of the velocity fields from both the PIV and the HARP methods is consistent with the CFD's. This also corresponds to the particle flows observed during the real optical imaging experiments. However, the PIV velocity field is more irregular and overestimated on the magnitude at the boundaries, while under-estimated inside the separation channel, compared to the CFD velocity field.

The problem is possibly from the relatively higher intensity of the particles at the areas where the velocity was overestimated. The relatively high intensity underlying at the areas could be resulted from the non-uniform light sheet during the imaging. When the particle flowed across the areas, it can result in a change of the static lights. The change was possibly interpreted as particle flows inside the sub-window by the correlation method. The problem is evident at the inlet and boundaries. Furthermore, the frequency of the light sources used in the optical imaging experiments also caused the change in the particle intensity taken at different times. This change will be accumulated in the displacement estimate in the correlation method as well. Finally, an occlusion

from the top surface of the phantom also caused the under-estimation of the particle flows at the areas below the center circle of the flow phantom as described previously. The correlation method was unable to differentiate the change from the particle flow under the occlusion. Such those problems are difficult to solve experimentally.

The velocity field of the HARP method has smoother magnitude change than the velocity field of the PIV method. However, the velocity field of the HARP method obviously shows more errors on its direction at the boundary of the center circle. This might be due to the field inhomogeneity of different tag spin materials that affects the phase of the MR complex data. Such a problem does not exist in the optical imaging experiments.

TABLE 3

THE MEAN ABSOLUTE ERROR (MAE) FROM THE PIV AND HARP METHODS
COMPARED WITH THE CFD AS A GROUND TRUTH

Imaging Modalities (vs. CFD)	Mean Absolute Error (cm/sec)
PIV	0.292933
HARP	0.327141

A quantitative comparison between the PIV and HARP methods was performed by the mean absolute error (MAE) fashion similarly to the comparison in the previous chapter. The velocity field of the CFD simulation was used as a ‘ground truth’ to point-by-point in the evaluation. The MAEs of the two methods within the separation channel are summarized in the Table 3.

From the Table 3, it shows that the velocity fields of both methods provide the similar magnitude of errors compared to the CFD velocity field. The HARP method has an overall averaged error of 0.327141 cm/sec while the PIV has an overall averaged error of 0.292933 cm/sec. This is because the irregularities from both velocity fields that have been previously described. Also, the asymmetry of the real flow phantom and imperfection during manufacturing the phantom possibly causes significant difference from the CFD velocity field that was used as the reference for this study.

D. Conclusion and Discussions

Even though the velocity fields from both methods shows a difference from the velocity field from the CFD simulation, it still demonstrated in this study that both methods provide the errors with the consistent magnitude. For qualitative comparison, the velocity fields showed the similarity of their velocity directions inside the separation channel of the flow phantom.

Beside the validation analysis, both imaging methods have their own advantages, and vice versa. The displacement estimation from the optical imaging method can be obtained by a simple correlation algorithm. However, it requires good experimental setups and procedures such as sufficient number of particles in a correlation window, uniform light sources, and optical transparency on the desired imaging plan, etc. This was difficult to achieve during the imaging experiments.

A flow quantification using MRI is more flexible in term of expanding our study for a higher dimension of the flow. Mainly, a modification of the imaging pulse sequence is required to acquire the flow data of different dimensions. In optical imaging, it involves modifications on imaging hardware setups that can introduce human errors. Furthermore, the flow phantom is required to be transparent in all of its geometry. This is a major disadvantage on the optical imaging to be used for biomedical flow applications such as blood flow or tissue quantification. Multiple cameras at different views are also required for data acquisition to differentiate the velocity components. Uniform light sources are required such that the PIV does not treat an oscillation from the illumination as the 'motion' in the analysis. This makes the PIV experiments difficult to achieve the repeatability of the same imaging conditions every time.

CHAPTER VII

CONCLUSIONS

In this study, two new MR quantification methods for very rapid flows has been developed and validated. First, the integration of HARP with a fast SEA imaging demonstrated the ability to be used as a tool to image and analyze high velocity flows. The method provides a visualization of an instantaneous fluid motion from the texture movement of the tagging lines. The method analyzes the velocity field from tagging data with a rapid processing and minimal manual intervention. The analysis result of the method demonstrated its consistency with the visualization of the imaged data.

Second, an improved HARP method was developed to deal with the errors from non-flow factors that can degrade the original HARP method. The factors are such as tag fading/ blurring, field inhomogeneity, and data noise in the raw MRI data. Specifically, the original HARP was improved by incorporating a regularization method to refine spurious velocity vectors. The regularization method includes physical flow constraints and the image constraint. Therefore, the result of the improved HARP method demonstrated a reasonable velocity field with more continuity than the quantification using only the HARP method. The quantitative comparison with the CFD simulation also demonstrated the improvement on its overall velocity field. In the real MR data, the regularization method also showed its improvement over the original HARP method. The quantitative improvement was performed based on the simulated velocity field from the CFD, which is only the theoretical reference due to no actual ground truth velocity

field. This indicates that the regularization method can help address the errors from other non-flow factors that degrade the original HARP analysis.

Finally, the two new methods were validated with the velocity fields from the computational fluid dynamics (CFD) and the conventional optimal flow imaging based on particle image velocimetry (PIV). Qualitatively, the velocity fields obtained from both methods provided consistent velocity direction inside the region of interest of the flow phantom, except for the velocities at the boundaries. Quantitatively, the quantification methods with the steady flow provided velocity fields with the similar error magnitude compared to the CFD velocity field. This possibly demonstrates the usefulness of the new methods for quantifying fluid flows based on MR tagging. Furthermore, these flow quantification methods can be useful especially when the quantification based on phase-contrast MRI is difficult to achieve [4, 5].

A. Future Research Directions

There are number of challenges for the HARP and the improved HARP methods from this work. First, a tunable bandpass filter approach might possibly improve the velocity field output. Conventionally, the filter parameters used in the HARP analysis are manually tuned for a reasonable initial outcome, and these parameters are used fixed filter parameters for the peak extraction of all flow data. For a quantification of a steady flow, this is acceptable since the time interval between each image can be chosen such that a good tagging data can still be obtained. However, when an instantaneous velocity

field is desired, tagging data at the later time will experience the signal void of the new flow spins and the tag fading from the relatively long imaging. This leads to a loss of good tagging profiles on the image. In Fourier domain, the data on each harmonic peak will expand and possibly smear with adjacent harmonic peaks in the worse case. Therefore, a tunable filter possibly helps compensate the problem of an expansion of the harmonic data.

Second, the work only used a simple 1-1 SPAMM pulse sequence to produce a tagging image. The data in the Fourier domain from this tagging pulse contains the original data of the tag magnitude image. This original data is usually undesired and not used in the HARP method. It should improve the choice of the bandpass filter parameters if the original peak is eliminated. This is possibly done by applying two 1-1 SPAMM pulses with a -90° flip angle RF pulse at the second SPAMM pulse. The pulse sequence is actually referred to the conjugated SPAMM (CSPAMM) pulse sequence [47, 83]. Furthermore, the DANTE tagging pulse sequence can also be used to improve the tag profile, e.g. more sharp transition on the tag lines. This potentially improves the field inhomogeneity problem that was experienced from the use of the SPAMM pulse sequence in the MR flow experiments.

Third, a peak combination approach [82] can be used to improve the velocity field outcome of the HARP method. It was shown that the combination of a peak and its conjugate can correct the phase errors statistically in Fourier domain. The approach can be applied to improve the velocity field as well. Furthermore, the harmonic peak and its

conjugate can provide separate velocity field outputs. These outputs can be averaged to obtain a velocity field with improved statistics.

Four, the HARP method for fluid flow quantification should be extended to a 3D study. Even though the HARP method can provide a dense 2D apparent velocity field in a rapid fashion, the extension to obtain a dense 3D velocity field is not trivial. Typically, 3D MRI data will provide sparse information along the slice direction. This is also the same issue for the 3D MR tagging, and it finally results in only a few points in the 3D MR tagging data that can provide the three-component velocity field. However, the advanced HARP imaging called zHARP [88] could possibly provide a dense 3D velocity field on a single image slice. This opens an opportunity to use MR tagging for a real flow study since the three velocity components can be obtained.

Five, the improved HARP method should tailor its ad-hoc optimization parameters and settings as fit to a flow study as possible. This includes the selection of ‘optimal’ parameters for the optimization algorithm such as the weight coefficients for the residual function, random methods at each generation step in the optimization algorithm, and the suitable number of population, the proper boundary conditions for a specific geometry of the flow phantom, and also the fluid properties, etc. Even though this issue has not been taken care of in this research work, the velocity field of the GA/EP algorithm still demonstrated its improvement over the original HARP method. A method that can provide general guidelines for the suitable selection of these settings is expected to an even-better improved velocity field result.

Six, the computation time for the improved HARP method is very long relatively to the original HARP method. This is because the improved method uses the GA/EP algorithm to search for the optimal solution. In this study, the GA/EP algorithm heuristically searches an optimal solution from a very large searching space, i.e. twice of the number of pixels in the flow phantom. This somewhat lessens the major advantage of the original HARP that can provide a velocity field within seconds. Therefore, a method to reduce the processing time is also desired. An approach to reduce the search domain for the algorithm such as local area optimization or parallel processing might help improve the running time and allow faster analysis.

Finally, the improved HARP method should be extended for a 3D flow study. Similarly to the HARP method, the improved 3D flow quantification is also required. In the implementation point of view, the improved method can be easily extended to account for the third dimension since the Navier-Stokes equation also holds. In real analysis, this might be impractical from the long search processing of an extremely large searching space. Parallel processing or reduced searching space approaches from the previous discussion is possibly a most likely solution for this future work. Furthermore, additional assumptions imposed on the analysis method can help improve the convergence of the analysis and reduce the computation times. This will depend on a specific type of flows in the study. For example, the Reynolds-averaged turbulent model or the $k - \varepsilon$ model can be used in the improved HARP method for a turbulent flow study.

REFERENCES

- [1] M. P. McDougall, and S. M. Wright, "Phase Compensation in Single Echo Acquisition Imaging," *IEEE-MEMB*, vol. 24, no. 6, pp. 17-22, 2005.
- [2] M. P. McDougall, and S. M. Wright, "64-Channel Array Coil for Single Echo Acquisition Magnetic Resonance Imaging," *ISMRM*, vol. 54, no. 2, pp. 386 – 392, 2005.
- [3] M. P. McDougall, "Single Echo Acquisition Magnetic Resonance Imaging," Ph.D. Dissertation, Electrical and Computer Engineering, Texas A&M University, College Station, 2004.
- [4] S. M. Wright, M. P. McDougall, and J. C. Bosshard, "Progress in Visualizing Turbulent Flow Using Single-Echo Acquisition Imaging," *IEEE-EMBS*, vol. 1, pp. 4877-4880, 2006.
- [5] S. M. Wright, M. P. McDougall, and N. Yallapragada, "Rapid Flow Imaging Using Single Echo Acquisition MRI," *ISMRM*, vol. 13, p. 289, 2005.
- [6] N. F. Osman, W. S. Kerwin, E. R. McVeigh, and J. L. Prince, "Cardiac Motion Tracking Using CINE Harmonic Phase (HARP) Magnetic Resonance Imaging," *Magnetic Resonance in Medicine*, vol. 42, no. 6, pp. 1048–1060, 1999.
- [7] N. F. Osman, and J. L. Prince, "Visualizing Myocardial Function Using HARP MRI," *Phys. Med. Biol.*, vol. 45, no. 6, pp. 1665–1682, 2000.

- [8] N. F. Osman, S. Sampath, and J. L. Prince, "Imaging Longitudinal Cardiac Strain on Short-Axis Images Using 3D-HARP," *SPIE Proceedings Series*, vol. 3978, pp. 206-216, 2000.
- [9] C. C. Moore, C. H. Lugo-Olivieri, E. R. McVeigh, and E. A. Zerhouni, "Three-Dimensional Systolic Strain Patterns in the Normal Human Left Ventricle: Characterization with Tagged MR Imaging," *Radiology*, vol. 214, pp. 453-466, 2000.
- [10] C. C. Moore, E. R. McVeigh, and E. A. Zerhouni, "Noninvasive Measurement of Three-Dimensional Myocardial Deformation with Tagged Magnetic Resonance Imaging During Graded Local Ischemia," *J. Cardiovasc. Magn. Reson.*, vol. 1, no. 3, pp. 207-222, 1999.
- [11] L. C. Palmon, N. Reichek, S. B. Yeon, N. R. Clark, D. Brownson *et al.*, "Intramural Myocardial Shortening in Hypertensive Left Ventricular Hypertrophy with Normal Pump Function," *Circulation*, vol. 89, no. 1, pp. 122-131, 1994.
- [12] A. S. Blom, J. J. Pilla, S. V. Pusca, H. J. Patel, L. Dougherty *et al.*, "Dynamic Cardiomyoplasty Decreases Myocardial Workload as Assessed by Tissue Tagged MRI," *ASAIO Journal*, vol. 46, no. 5, pp. 556-562, 2000.
- [13] R. Mankad, C. J. McCreery, W. J. Rogers. Jr., R. J. Weichmann, E. B. Savage *et al.*, "Regional Myocardial Strain Before and After Mitral Valve Repair for Severe Mitral Regurgitation," *J. Cardiovasc. Magn. Reson.*, vol. 3, no. 3, pp. 257-266, 2001.

- [14] P. Dubach, J. Myers, P. Bonetti, T Schertler, V Froelicher *et al.*, “Effects of Bisoprolol Fumarate on Left Ventricular Size, Function, and Exercise Capacity in Patients with Heart Failure: Analysis with Magnetic Resonance Myocardial Tagging,” *Amer. Heart J.*, vol. 143, no. 4, pp. 676-683, 2002.
- [15] M. Schiemann, F. Bakhtiary, V. Hietschold, A. Koch, A. Esmaeili *et al.*, “MR-based Coronary Artery Blood Velocity Measurements in Patients without Coronary Artery Disease,” *Eur. Radiol.*, vol. 16, no. 5, pp. 1124-1130, 2006.
- [16] S. A. Berger, “Flows in Stenotic Vessels,” *Annual Review of Fluid Mechanics*, vol. 32, pp. 347-382, 2000.
- [17] H. M. Gach, and I. J. Lowe, “Characterization of Flow Emerging from A Stenosis Using MRI,” *Magn. Reson. Med.*, vol. 40, pp. 559-570, 1998.
- [18] B. H. Weigl, R. L. Bardell, and C. R. Cabrera, “Lab-On-A-Chip for Drug Development,” *Advanced Drug Delivery Reviews*, vol. 55, pp. 349-377, 2003.
- [19] H. A. Stone, A. D. Stroock, and A. Ajdari, “Engineering Flows in Small Devices: Microfluidics toward A Lab-On-A-Chip,” *Annual Review of Fluid Mechanics*, vol. 36, pp. 381-411, 2004.
- [20] H. Song, and R. F. Ismagilov, “Millisecond Kinetics on A Microfluidic Chip Using Nanoliters of Reagents,” *Journal of the American Chemical Society*, vol. 125, pp. 14613-14619, 2003.
- [21] K. D. Jensen, “Flow Measurements,” *J. of the Braz. Soc. of Mech. Sci. & Eng.*, vol. 26, no. 4, pp. 400-419, 2004.

- [22] P. R. Hoskins, A. Fleming, P. Stonebridge, P. L. Allan, and D. Cameron, "Scan-plane Vector Maps and Secondary Flow Motions," *European Journal Ultrasound*, vol. 1, pp. 159-169, 1994.
- [23] J. R. Overbeck, K. W. Beach, and D. Strandness Jr., "Vector Doppler: Accurate Measurements of Blood Velocity in Two Dimensions," *Ultrasound Medicine Biology*, vol. 18, pp. 19-31, 1992.
- [24] T. A. Maniatis, R. S. C. Cobbold, and K. W. Johnston, "Flow Imaging in An End to Side Anastomosis Model Using Two-Dimensional Velocity Vectors," *Ultrasound Medicine Biology*, vol. 20, pp. 559-569, 1994.
- [25] D. Y. Fei, C. T. Fu, W. H. Brewer, and K. A. Kraft, "Angle Independent Doppler Colour Imaging: Determination of Accuracy and A Method of Display," *Ultrasound Medicine Biology*, vol. 20, pp. 147-155, 1994.
- [26] M. D. Fox, and W. M. Gardiner, "Three-Dimensional Doppler Velocimetry of Flow Jets," *IEEE Trans. On Biomedical Engineering*, vol. 35, no. 10, pp. 834-841, 1988.
- [27] H. F. Routh, "Doppler Ultrasound: The Ability to Measure and Image Blood Flow," *IEEE Engineering in Medicine and Biology*, vol. 15, no. 6, pp. 31-40, 1996.
- [28] P. R. Hoskins, "A Review of the Measurement of Blood Velocity and Related Quantities Using Doppler Ultrasound," *Proc IMechE, Path H: Journal of Engineering in Medicine*, vol. 213, no. 5, pp. 391-400, 1999.

- [29] P. N. T. Wells, "Ultrasonic Colour Flow Imaging," *Phys. Med. Biol.*, vol. 39, pp. 2113-2145, 1994.
- [30] C. Ozturk, J. A. Derbyshire, and E. R. McVeigh, "Estimating Motion From MRI Data," in *Proceeding of The IEEE*, pp. 1627-1648, 2003.
- [31] R. Muthupillai, D. J. Lomas, P. J. Rossman, J. F. Greeleaf, A. Manduca *et al.*, "Magnetic Resonance Elastography by Direct Visualization of Propagating Acoustic Strain Waves," *Science*, vol. 269, no. 5232, pp. 1854-1857, 1995.
- [32] P. J. Basser, and D. K. Jones, "Diffusion-Tensor MRI: Theory, Experimental Design and Data Analysis - A Technical Review," *NMR Biomed.*, vol. 15, no. 7-8, pp. 456-467, 2002.
- [33] C. J. Elkins, and M. T. Alley, "Magnetic Resonance Velocimetry: Applications of Magnetic Resonance Imaging in the Measurement of Fluid Motion," *Experiments in Fluids*, vol. 43, no. 6, pp. 823-858, December, 2007.
- [34] E. Fukushima, "Nuclear Magnetic Resonance as A Tool to Study Flow," *Annual Review of Fluid Mechanics*, vol. 31, pp. 95-123, 1999.
- [35] Q. Long, X. Y. Xu, M. W. Collins, T. M. Griffith, and M. Bourne, "The Combination of Magnetic Resonance Angiography and Computational Fluid Dynamics: A Critical Review," *Critical Reviews in Biomedical Engineering*, vol. 26, no. 4, pp. 227-274, 1998.
- [36] E. Zerhouni, D. Parish, W. Rogers, A. Yang, and E. P. Shapiro, "Human Heart: Tagging with MR Imaging—A Method for Noninvasive Assessment of Myocardial Motion," *Radiology*, vol. 169, pp. 59-63, 1988.

- [37] T. J. Mosher, and M. B. Smith, "A DANTE Tagging Sequence for The Evaluation of Translational Sample Motion," *Magn. Reson. Med.*, vol. 15, no. 2, pp. 334–339, 1990.
- [38] L. Axel, and L. Dougherty, "MR Imaging of Motion with Spatial Modulation of Magnetization," *Radiology*, vol. 171, pp. 841–845, 1989.
- [39] L. Axel, and L. Dougherty, "Heart Wall Motion: Improved Method of Spatial Modulation of Magnetization for MR Imaging," *Radiology*, vol. 172, no. 2, pp. 349-350, 1989.
- [40] E. R. McVeigh, and B. D. Bolster Jr., "Improved Sampling of Myocardial Motion with Variable Separation Tagging," *Magn. Reson. Med.*, vol. 39, no. 4, pp. 657–661, 1998.
- [41] A. J. de Crespigny, T. A. H. Carpenter, and L. D. Hall, "Cardiac Tagging in The Rat Using A DANTE Sequence," *Magn. Reson. Med.*, vol. 21, pp. 151-156, 1991.
- [42] J. G. Proakis, and D. G. Manolakis, *Digital Signal Processing: Principles, Algorithms, and Applications*, 4th ed., Upper Saddle River, N.J.: Pearson Prentice Hall, 2006.
- [43] S. E. Fischer, G. C. McKinnon, S. E. Maier, and P. Boesiger., "Improved Myocardial Tagging Contrast," *Magn. Reson. Med.*, vol. 30, no. 2, pp. 191-200, 1993.
- [44] P. A. Bottomley, T. H. Foster, R. E. Argersinger, and L. M. Pfeifer, "A Review of Normal Tissue Hydrogen NMR Relaxation Times and Relaxation Mechanisms

- from 1-100 MHz: Dependence on Tissue Type, NMR Frequency, Temperature, Species, Excision, and Age,” *Med. Phys.*, vol. 11, no. 4, pp. 425-448, 1984.
- [45] S. E. Fischer, G. C. McKinnon, M. B. Scheidegger, W. Prins, D. Meier *et al.*, “True Myocardial Motion Tracking,” *Magn. Reson. Med.*, vol. 31, no. 4, pp. 401-413, 1994.
- [46] M. NessAiver, and J. L. Prince, “Magnitude Image CSPAMM Reconstruction (MICSAR),” *Magn. Reson. Med.*, vol. 50, pp. 331–342, 2003.
- [47] M. K. Ivancevic, J.-L. Daire, J.-N. Hyacinthe, G. Crelier, S. Kozerke *et al.*, “High-Resolution Complementary Spatial Modulation of Magnetization (CSPAMM) Rat Heart Tagging on A 1.5 Tesla Clinical Magnetic Resonance System,” *Investigative Radiology*, vol. 42, no. 3, pp. 204-210, 2007.
- [48] G. Shechter, C. Ozturk, and E. R. McVeigh, "Interactive Four-Dimensional Segmentation of Multiple Image Sets," in *Proceedings of SPIE*, vol. 3976, pp. 165-173, 2000.
- [49] M. A. Guttman, J. L. Prince, and E. R. McVeigh, “Tag and Contour-Detection in Tagged MR Images of The Left Ventricle,” *IEEE Trans. on Medical Images*, vol. 13, no. 1, pp. 74-88, 1994.
- [50] T. S. Denney Jr., “Estimation and Detection of Myocardial Tags in MR Image Without User-Defined Myocardial Contours,” *IEEE Trans. On Medical Imaging*, vol. 18, no. 4, pp. 330-344, 1999.

- [51] E. R. McVeigh, and E. Zerhouni, "Noninvasive Measurement of Transmural Gradients in Myocardial Strain with MR Imaging," *Radiology*, vol. 180, no. 3, pp. 677-683, 1991.
- [52] M. A. Guttman, E. A. Zerhouni, and E. R. McVeigh, "Analysis of Cardiac Function from MR Images," *IEEE Computer Graphics and Applications*, vol. 17, pp. 30-38, Jan - Feb 1997.
- [53] A. Amini, R. Curwen, R. T. Constable, and J. C. Gore, "MR Physics-Based Snake Tracking and Dense Deformation from Tagged Cardiac Images," *AAAI Int. Symposium on Applications of Computer Vision to Medical Image Processing*, Stanford University, Stanford, California, March 1994.
- [54] A. A. Young, and L. Axel, "Three-Dimensional Motion and Deformation of The Heart Wall: Estimation with Spatial Modulation of Magnetization-A Model Based Approach," *Radiology*, vol. 185, no. 1, pp. 241-247, 1992.
- [55] A. A. Young, D. L. Kraitchman, L. Dougherty, and L. Axel, "Tracking and Finite Element Analysis of Stripe Deformation in Magnetic Resonance Tagging," *IEEE Trans. On Medical Imaging*, vol. 14, no. 3, pp. 413-421, 1995.
- [56] J. Declerck, T. S. Denney, C. Ozturk, W. G. O' Dell, and E. R. McVeigh, "Left Ventricular Motion Reconstruction from Planar Tagged MR Images: A Comparison," *Phys. Med. Biol.*, vol. 45, pp. 1611-1632, 2000.
- [57] W. G. O' Dell, C. C. Moore, W. C. Hunter, E. A. Zerhouni, and E. R. McVeigh, "Three-dimensional Myocardial Deformations: Calculation with Displacement

- Field Fitting to Tagged MR Images,” *Radiology*, vol. 195, no. 3, pp. 829-835, 1995.
- [58] J. Declerck, N. Ayache, and E. R. McVeigh, "Use of A 4D Planispheric Transformation for The Tracking and The Analysis of LV Motion with Tagged MR Images," *Rapport de Recherche - Institut National de Recherche en Informatique et en Automatique*, vol. 3535, pp. 1-37, 1998.
- [59] T. O' Donnell, T. Boult, and A. Gupta, "Global Models with Parametric Offsets As Applied to Cardiac Motion Recovery," in *Proc. IEEE Comput. Soc. Conf. Computer Vision Pattern Recognition*, pp. 293-299, 1996.
- [60] J. Park, D. Metaxas, and L. Axel, "Analysis of Left Ventricular Motion Based on Volumetric Deformable Models and MRI-SPAMM," *Med. Image Anal.*, vol. 1, pp. 53-71, 1996.
- [61] T. S. Denney Jr, and J. L. Prince, "Reconstruction of 3D Left Ventricular Motion from Planar Tagged Cardiac MR Images: An Estimation Theoretic Approach," *IEEE Trans. On Medical Imaging*, vol. 14, no. 4, pp. 625-635, 1995.
- [62] T. S. Denney Jr, and E. R. McVeigh, "Model-Free Reconstruction of Three-Dimensional Myocardial Strain From Planar Tagged MR Images," *Journal of Magnetic Resonance Imaging*, vol. 7, no. 5, pp. 799-810, 1997.
- [63] T. S. Denney Jr, B. L. Gerber, and L. Yan, "Unsupervised Reconstruction of A Three-Dimensional Left Ventricular Strain from Parallel Tagged Cardiac Images," *Magn. Reson. Med.*, vol. 49, no. 4, pp. 743-754, 2003.

- [64] P. Clarysse, C. Basset, L. Khouas, P. Croisille, D. Friboulet *et al.*, “Two-Dimensional Spatial and Temporal Displacement and Deformation Field Fitting from Cardiac Magnetic Resonance Tagging,” *Med. Image Anal.*, vol. 4, pp. 253-268, 2000.
- [65] M. Daniel, “Data Fitting with B-Spline Curves,” in *Modeling and Graphics in Science and Technology*, Springer Verlag, pp. 99-104, 1996.
- [66] C. Ozturk, and E. R. McVeigh, “Four Dimensional B-Spline Based Motion Analysis of Tagged Cardiac MR Images,” in *Proc. SPIE, Medical Imaging 1999: Physiology and Function from Multi-Dimensional Images*, pp. 46-56, 1999.
- [67] J. Declerck, J. Feldmar, and N. Ayache, “Definition of A Four-Dimensional Continuous Planispheric Transformation for The Tracking and The Analysis of Left-Ventricle Motion,” *Med. Image Anal.*, vol. 2, pp. 197-213, 1998.
- [68] K. Kose, “Visualization of Turbulent Motion Using Echo-Planar Imaging with A Spatial Tagging Sequence,” *Journal of Magnetic Resonance*, vol. 98, pp. 599-603, 1992.
- [69] R. R. Edelman, D. Chien, D. J. Atkinson, and J. Sandstrom, “Fast Time-of-Flight MR Angiography with Improved Background Suppression,” *Radiology*, vol. 179, no. 3, pp. 867-870, 1991.
- [70] K. W. Moser, E. C. Kutter, J. G. Georgiadis, R. O. Buckius, H. D. Morris *et al.*, “Velocity Measurement of Flow Through a Step Stenosis Using Magnetic Resonance Imaging,” *Experiments in Fluids*, vol. 29, no. 5, pp. 438-447, 2000.

- [71] M. J. Black, and P. Anandan, "The Robust Estimation of Multiple Motions: Parametric and Piece-Wise Smooth Flow Fields," *Comput. Visi. Image Understanding*, vol. 63, pp. 75-104, 1996.
- [72] K. W. Moser, J. G. Georgiadis, and R. O. Buckius, "On the Use of Optical Flow Methods with Spin-Tagging Magnetic Resonance Imaging," *Annals of Biomedical Engineering*, vol. 29, pp. 9-17, 2001.
- [73] C. K. Macgowan, and M. L. Wood, "Fast Measurements of the Motion and Velocity Spectrum of Blood Using MR Tagging," *Magn. Reson. Med.*, vol. 45, no. 3, pp. 461-469, 2001.
- [74] N. F. Osman, E. R. McVeigh, and J. L. Prince, "Imaging Heart Motion Using Harmonic Phase MRI," *IEEE Trans. On Medical Imaging*, vol. 19, no. 3, pp. 186-202, 2000.
- [75] N. F. Osman, and J. L. Prince, "Harmonic phase MRI," in *Measurement of Cardiac Deformation from MRI: Physical and Mathematical Models*, A. A. Amini and J. L. Prince, Eds. pp. 119-150: Norwell, MA : Kluwer Academic Publishers, pp. 119-150, 2001.
- [76] V. Parthasarathy, J. L. Prince, M. Stone, E. Z. Murano, and M. NessAiver, "Measuring Tongue Motion from Tagged Cine-MRI Using Harmonic Phase (HARP) Processing," *J. Acoust. Soc. Am.*, vol. 121, no. 1, pp. 491-504, 2007.
- [77] S. R. R. Tecelao, J. J. M. Zwanenburg, J. P. A. Kuijer, and J. T. Marcus, "Extended Harmonic Phase Tracking of Myocardial Motion: Improved Coverage

- of Myocardium and Its Effect on Strain Results," *Journal of Magnetic Resonance Imaging*, vol. 23, pp. 682-690, 2006.
- [78] S. Sampath, J. A. Derbyshire, N. F. Osman, E. Atalar, and J. L. Prince, "Real-Time Imaging of Cardiac Strain Using Ultra fastHARP Sequence," in *Proc. Intl. Soc. Mag. Reson. Med.*, vol. 9, p. 111, 2001.
- [79] K. Z. Abd-Elmoniem, and J. L. Prince, "Algorithms for Real-Time FastHARP Cardiac Function Analysis," *Lecture Notes in Computer Science, Medical Image Computing and Computer-Assisted Intervention - MICCAI 2003* pp. 516-523: Springer Berlin / Heidelberg, 2003.
- [80] J. P. A. Kuijjer, M. B. M. Hofman, J. J. M. Zwanenburg, J. T. Marcus, A. C. van Rossum *et al.*, "DENSE and HARP: Two Views on the Same Technique of Phase-Based Strain Imaging," *Journal of Magnetic Resonance Imaging*, vol. 24, pp. 1432-1438, 2006.
- [81] K. Z. Abd-Elmoniem, S. Sampath, N. F. Osman, and J. L. Prince., "Real-Time Monitoring of Cardiac Regional Function Using FastHARP MRI and Region-of-Interest Reconstruction," *IEEE Trans. on Biomedical Engineering*, vol. 54, no. 9, pp. 1650-1656, September, 2007.
- [82] S. Ryf, J. Tsao, J. Schwitter, A. Stuessi, and P. Boesiger, "Peak-Combination HARP: A Method to Correct for Phase Errors in HARP," *Journal of Magnetic Resonance Imaging*, vol. 20, pp. 874-880, 2004.

- [83] S. Ryf, M. A. Spiegel, M. Gerber, and P. Boesiger, "Myocardial Tagging With 3D-CSPAMM," *Journal of Magnetic Resonance Imaging*, vol. 16, pp. 320–325, 2002.
- [84] I. Haber, and C. F. Westin, "Model-Based 3D Tracking of Cardiac Motion in HARP Images," in *Proc. Intl. Soc. Mag. Reson. Med.* 10th Meeting, p. 1672, 2002
- [85] L. Pan, J. L. Prince, J. A. C. Lima, and N. F. Osman, "Fast Tracking of Cardiac Motion Using 3D-HARP," *IEEE Trans. On Biomedical Engineering*, vol. 52, no. 8, pp. 1425-1435, 2005.
- [86] L. Pan, J. A. C. Lima, and N. F. Osman, "Fast Tracking of Cardiac Motion Using 3D-HARP," *LNCS IPMI*, C. J. Taylor and J. A. Noble, eds., pp. 611-622, 2003.
- [87] S. Sampath, and J. L. Prince, "Automatic 3D Tracking of Cardiac Material Markers Using Slice-Following and Harmonic-Phase MRI," *Journal of Magnetic Resonance Imaging*, vol. 25, pp. 197-208, 2007.
- [88] K. Z. Abd-Elmoniem, M. Stuber, N. F. Osman, and J. L. Prince, "ZHARP: Three-Dimensional Motion Tracking from a Single Image Plane," *IPMI*, no. LNCS 3565, pp. 639–651, 2005.
- [89] Y. Zhu, and N. J. Pelc, "Three-Dimensional Motion Tracking with Volumetric Phase Contrast MR Velocity Imaging," *Journal of Magnetic Resonance Imaging*, vol. 9, no. 1, pp. 111-118, 1999.
- [90] E. Bergvall, P. Cain, H. Arheden, and G. Sparr, "A Fast and Highly Automated Approach to Myocardial Motion Analysis Using Phase Contrast Magnetic

- Resonance Imaging,” *Journal of Magnetic Resonance Imaging*, vol. 23, pp. 652-661, 2006.
- [91] S. Ringgaard, S. A. Oyre, and E. M. Pedersen, “Arterial MR Imaging Phase-Contrast Flow Measurement: Improvements with Varying Velocity Sensitivity during Cardiac Cycle,” *Radiology*, vol. 232, no. 1, pp. 289-294, 2004.
- [92] N. J. Pelc, M. A. Bernstein, A. Shimakawa, and G. H. Glover, “Encoding Strategies for Three-Direction Phase-Contrast MR Imaging of Flow,” *Journal of Magnetic Resonance Imaging*, vol. 1, no. 4, pp. 405-413, 1991.
- [93] N. J. Pelc, F. G. Sommer, K. C. P. Li, T. J. Brosnan, R. J. Herfkens *et al.*, “Quantitative Magnetic Resonance Flow Imaging,” *Magnetic Resonance Quarterly*, vol. 10, no. 3, pp. 125-147, 1994.
- [94] M. Markl, F. P. Chan, M. T. Alley, K. L. Wedding, and M. T. Draney *et al.*, “Time-Resolved Three-Dimensional Phase-Contrast MRI,” *Journal of Magnetic Resonance Imaging*, vol. 17, no. 4, pp. 499-506, 2003.
- [95] M. Markl, F. P. Chan, M. T. Alley, K. L. Wedding, and M. T. Draney *et al.*, “Erratum: Markl M, et al. Time Resolved Three Dimensional Phase Contrast MRI. *Journal of Magn Reson Imaging* 2003;17:499-506,” *Journal of Magnetic Resonance Imaging*, vol. 18, no. 3, pp. 396-396, 2003.
- [96] R. Bammer, T. A. Hope, M. Aksoy, and M. T. Alley, “Time-Resolved 3D Quantitative Flow MRI of the Major Intracranial Vessels: Initial Experience and Comparative Evaluation at 1.5T and 3.0T in Combination With Parallel Imaging,” *Magn. Reson. Med.*, vol. 57, no. 1, pp. 127-140, 2007.

- [97] L. R. Pelc, N. J. Pelc, S. C. Rayhill, L. J. Castro, G. H. Glover *et al.*, “Arterial and Venous Blood Flow: Noninvasive Quantitation with MR Imaging,” *Radiology*, vol. 185, no. 3, pp. 809-812, 1992.
- [98] G. R. Caputo, C. Kondo, T. Masui, S. J. Geraci, E. Foster *et al.*, “Right and Left Lung Perfusion: In Vitro and In Vivo Validation with Oblique-Angle, Velocity-Encoded CINE MR Imaging,” *Radiology*, vol. 180, no. 3, pp. 693-698, 1991.
- [99] C. Kondo, G. R. Caputo, T. Masui, E. Foster, M. O' Sullivan *et al.*, “Pulmonary Hypertension: Pulmonary Flow Quantification and Flow Profile Analysis with Velocity-Encoded CINE MR Imaging,” vol. 183, no. 3, pp. 751-758, 1992.
- [100] F. G. Sommer, B. Noorbehesht, N. J. Pelc, R. Jamison, A. J. Pinevich *et al.*, “Normal Renal Blood Flow Measurement Using Phase-Contrast CINE Magnetic Resonance Imaging,” *Investigative Radiology*, vol. 27, no. 6, pp. 465-470, 1992.
- [101] B. D. Myers, F. G. Sommer, K. Li, S. Tomlanovich, N. R. Pelc *et al.*, “Determination of Blood-Flow to The Transplanted Kidney: A Novel Application of Phase-Contrast CINE Magnetic Resonance Imaging,” *Transplantation*, vol. 57, no. 10, pp. 1445-1450, 1994.
- [102] D. R. Enzmann, M. P. Marks, and N. J. Pelc, “Comparison of Cerebral Artery Blood Flow Measurements with Gated CINE and Ungated Phase-Contrast Techniques,” *Journal of Magnetic Resonance Imaging*, vol. 3, pp. 703-712, 1993.

- [103] D. R. Enzmann, M. R. Ross, M. P. Marks, and N. J. Pelc, "Blood Flow in Major Cerebral Arteries Measured by Phase-Contrast CINE MR," *AJNR*, vol. 15, pp. 123-129, 1994.
- [104] M. P. Marks, N. J. Pelc, M. R. Ross, and D. R. Enzmann, "Determination of Cerebral Blood Flow with A Phase-Contrast CINE MR Technique: Evaluation of Normal and AVM Patients," *Radiology*, vol. 182, pp. 467-476, 1992.
- [105] M. C. Dulce, G. H. Mostbeck, M. O' Sullivan, M. Cheitlin, G. R. Caputo *et al.*, "Severity of Aortic Regurgitation: Interstudy Reproducibility of Measurements with Velocity-Encoded CINE MR Imaging," *Radiology*, vol. 185, pp. 235-240, 1992.
- [106] A. C. Eichenberger, R. Jenni, and G. K. von Schulthess, "Aortic Valve Pressure Gradients in Patients with Aortic Valve Stenosis: Quantification with Velocity-Encoded CINE MR Imaging," *AJR*, vol. 160, pp. 971-977, 1993.
- [107] J. J. M. Westenberg, M. G. Danilouchkine, J. Doornbos, J. J. Bax, R. J. van der Geest *et al.*, "Accurate and Reproducible Mitral Valvular Blood Flow Measurement with Three-Directional Velocity-Encoded Magnetic Resonance Imaging," *Journal of Cardiovascular Magnetic Resonance*, vol. 6, no. 4, pp. 767-776, 2004.
- [108] J. Lotz, C. Meier, A. Leppert, and M. Galanski, "Cardiovascular Flow Measurement with Phase-Contrast MR Imaging: Basic Facts and Implementation," *RadioGraphics*, vol. 22, pp. 651-671, 2002.

- [109] H. Wegmuller, J. O. Fredrickson, T. J. Brosnan, , N. J. Pelc, J. F. Debatin *et al.*, "CINE Phase Contrast versus Respiratory Resolved TRIADS in the Portal Vein," in *Proc Soc Mag Res Med: Flow Quantification and Flow Profile Analysis*, p. 674, 1993.
- [110] D. J. Burkart, C. D. Johnson, R. L. Ehman, A. L. Weaver, and D. M. Ilstrup, "Evaluation of Portal Venous Hypertension with CINE Phase-Contrast MR Flow Measurements: High Association of Hyperdynamic Portal Flow with Variceal Hemorrhage," *Radiology*, vol. 188, pp. 643-648, 1993.
- [111] G. P. Chatzimavroudis, H. Zhang, S. S. Halliburton, J. R. Moore, O. P. Simonetti *et al.*, "Clinical Blood Flow Quantification with Segmented k-Space Magnetic Resonance Phase Velocity Mapping," *Journal of Magnetic Resonance Imaging*, vol. 17, no. 1, pp. 65-71, 2003.
- [112] T. Q. Li, J. D. Seymour, R. L. Powell, K. L. McCarthy, L. Odberg *et al.*, "Turbulent Pipe Flow Studied by Time-Averaged NMR Imaging: Measurements of Velocity Profile and Turbulent Intensity," *Magnetic Resonance Imaging*, vol. 12, no. 6, pp. 923-934, 1994.
- [113] J. M. Siegel, J. N. Oshinski, R. I. Pettigrew, and D. N. Ku, "The Accuracy of Magnetic Resonance Phase Velocity Measurements in Stenotic Flow," *J. Biomech*, vol. 29, no. 12, pp. 1665-1672, 1996.
- [114] C. J. Elkins, M. Markl, A. Iyengar, R. Wicker, and J. K. Eaton, "Full-Field Velocity and Temperature Measurements Using Magnetic Resonance Imaging in

- Turbulent Complex Internal Flows,” *Int. J. Heat Fluid Flow*, vol. 25, no. 5, pp. 702-710, 2004.
- [115] C. J. Elkins, M. Markl, N. Pelc, and J. K. Eaton, “4D Magnetic Resonance Velocimetry for Mean Velocity Measurements in Complex Turbulent Flows,” *Experiments in Fluids*, vol. 34, no. 4, pp. 494-503, 2003.
- [116] G. Iaccarino, G. Kalitzin, and C. J. Elkins, "Numerical and Experimental Investigation of The Turbulent Flow in A Ribbed Serpentine Passage", *CTR Center for Turbulence Research Annual Research Briefs 2003*, Department of Mechanical Engineering, Stanford University, Stanford, CA, pp. 379-387, 2004.
- [117] V. S. Lee, C. E. Spritzer, B. A. Carroll, L. G. Pool, M. A. Bernstein *et al.*, “Flow Quantification Using Fast Cine Phase-Contrast MR Imaging, Conventional Cine Phase-Contrast MR Imaging, and Doppler Sonography: In Vitro and In Vivo Validation,” *AJR*, vol. 169, pp. 1125-1131, 1997.
- [118] B. Newling, S. J. Gibbs, J. A. Derbyshire, D. Xing, L. D. Hall *et al.*, “Comparisons of Magnetic Resonance Imaging Velocimetry with Computational Fluid Dynamics,” *Journal of Fluids Engineering*, vol. 119, pp. 103-109, 1997.
- [119] P. J. Kilner, C. C. Manzara, R. H. Mohiaddin, D. J. Pennell, M. G. St. J. Sutton *et al.*, “Magnetic Resonance Jet Velocity Mapping in Mitral and Aortic Valve Stenosis,” *Circulation*, vol. 87, pp. 1239-1248, 1993.
- [120] M. Markl, M. T. Alley, and N. J. Pelc, “Balanced Phase-Contrast Steady-State Free Precession (PC-SSFP): A Novel Technique for Velocity Encoding by Gradient Inversion,” *Magn. Reson. Med.*, vol. 49, no. 5, pp. 945–952, 2003.

- [121] K. Kose, "Instantaneous Flow-Distribution Measurements of The Equilibrium Turbulent Region in A Circular Pipe Using Ultrafast NMR Imaging," *Phys. Rev. A*, vol. 44, no. 4, pp. 2495-2504, 1991.
- [122] J. C. Gatenby, and J. C. Gore, "Echo-Planar-Imaging Studies of Turbulent Flow," *Journal of Magnetic Resonance Series A*, vol. 121, no. 2, pp. 193-200, 1996.
- [123] H. M. Gach, and I. J. Lowe, "Measuring Flow Reattachment Lengths Downstream of A Stenosis Using MRI," *Journal of Magnetic Resonance Imaging*, vol. 12, no. 6, pp. 939-948, 2000.
- [124] A. J. Sederman, M. D. Mantle, C. Buckley, and L. F. Gladden, "MRI Technique for Measurement of Velocity Vectors, Acceleration, and Autocorrelation Functions in Turbulent Flow," *Journal of Magnetic Resonance*, vol. 166, no. 2, pp. 182-189, 2004.
- [125] W. R. Overall, D. G. Nishimura, and B. S. Hu, "Fast Phase-Contrast Velocity Measurement in the Steady State," *Magn. Reson. Med.*, vol. 48, no. 5, pp. 890-898, 2002.
- [126] J.-F. Nielsen, and K. S. Nayak, "Pulse Sequences for Phase-Contrast SSFP Imaging from A Single Steady-State," in *Proc. Int. Soc. Magn. Reson. Med. Sci. Meet. Exhib.*, p. 879, 2006.
- [127] K. S. Nayak, B. S. Hu, and D. G. Nishimura, "Rapid Quantitation of High-Speed Flow Jets," *Magn. Reson. Med.*, vol. 50, no. 2, pp. 366-372, 2003.

- [128] J. H. Gao, and J. C. Gore, "Turbulent Flow Effects on NMR Imaging: Measurement of Turbulent Intensity," *Med. Phys.*, vol. 18, no. 5, pp. 1045-1051, 1991.
- [129] D. O. Kuethe, and J.-H. Gao, "NMR Signal Loss from Turbulence: Models of Time Dependence Compared with Data," *Physical Review E (Statistical Physics, Plasmas, Fluids, and Related Interdisciplinary Topics)*, vol. 51, no. 4, pp. 3252-3262 1995.
- [130] S. D. Beyea, S. A. Altobelli, and L. A. Mondy, "Chemically Selective NMR Imaging of A 3-Component (Solid-Solid-Liquid) Sedimenting System," *Journal of Magnetic Resonance*, vol. 161, no. 2, pp. 198-203, 2003.
- [131] J. Gotz, and K. Zick, "Local Velocity and Concentration of The Single Components in Water/Oil Mixtures Monitored by Means of MRI Flow Experiments in Steady Tube Flow," *Chem. Eng. Technol.*, vol. 26, no. 1, pp. 59-68, 2003.
- [132] T. Moraczewski, H. Y. Tang, and N. C. Shapley, "Flow of a Concentrated Suspension Through an Abrupt Axisymmetric Expansion Measured by Nuclear Magnetic Resonance Imaging," *J. Rheol.*, vol. 49, no. 6, pp. 1409-1428, 2005.
- [133] N. L. Nguyen, R. Reimert, and E. H. Hardy, "Application of Magnetic Resonance Imaging (MRI) to Determine The Influence of Fluid Dynamics on Desulfurization in Bench Scale Reactors," *Chem. Eng. Technol.*, vol. 29, no. 7, pp. 820-827, 2006.

- [134] I. Koptyug, A. A. Lysova, A. Kulikov, V. A. Kirillov, V. N. Parmon *et al.*, “Functional Imaging and NMR Spectroscopy of an Operating Gas-Liquid-Solid Catalytic Reactor,” *Appl. Catal. A Gen.*, vol. 267, no. 1-2, pp. 143-148, 2004.
- [135] M. D. Mantle, and A. J. Sederman, “Dynamic MRI in Chemical Process and Reaction Engineering,” *Proc. Nucl. Magn. Reson. Spectrosc.*, vol. 43, no. 1-2, pp. 3-60, 2003.
- [136] A. H. Aletras, S. Ding, R. S. Balaban, and H. Wen, “DENSE: Displacement Encoding with Stimulated Echoes in Cardiac Functional MRI,” *Journal of Magnetic Resonance*, vol. 137, no. 1, pp. 247-252, 1999.
- [137] T. L. Chenevert, A. R. Skovoroda, M. O’Donnell, and S. Y. Emelianov, “Elasticity Reconstructive Imaging by Means of Stimulated Echo MRI,” *Magn. Reson. Med.*, vol. 39, no. 3, pp. 482-490, 1998.
- [138] A. D. Hanlon, S. J. Gibbs, L. D. Hall, D. E. Haycock, W. J. Frith *et al.*, “Rapid MRI and Velocimetry of Cylindrical Couette Flow,” *Magnetic Resonance Imaging*, vol. 16, no. 8, pp. 953-961, 1998.
- [139] A. Caprihan, R. H. Griffey, and E. Fukushima, “Velocity Imaging of Slow Coherent Flows Using Stimulated Echoes,” *Magn. Reson. Med.*, vol. 15, pp. 327-333, 1990.
- [140] A. H. Aletras, R. S. Balaban, and H. Wen, “High-Resolution Strain Analysis of the Human Heart with Fast-DENSE,” *Journal of Magnetic Resonance*, vol. 140, no. 1, pp. 41-57, 1999.

- [141] A. H. Aletras, and H. Wen, "Mixed Echo Train Acquisition Displacement Encoding With Stimulated Echoes: An Optimized DENSE Method for In Vivo Functional Imaging of the Human Heart," *Magn. Reson. Med.*, vol. 46, no. 3, pp. 523-534, 2001.
- [142] A. H. Aletras, and A. E. Arai, "meta-DENSE Complex Acquisition for Reduced Intravoxel Dephasing," *Journal of Magnetic Resonance*, vol. 169, no. 2, pp. 246-249, 2004.
- [143] B. S. Spottiswoode, X. Zhong, A. T. Hess, C. M. Kramer, E. M. Meintjes *et al.*, "Tracking Myocardial Motion from Cine DENSE Images Using Spatiotemporal Phase Unwrapping and Temporal Fitting," *IEEE Trans. On Medical Imaging*, vol. 26, no. 1, pp. 15-30, 2007.
- [144] W. D. Gilson, Z. F. Yang, Brent A, and F. H. Epstein, "Complementary Displacement-Encoded MRI for Contrast-Enhanced Infarct Detection and Quantification of Myocardial Function in Mice," *Magn. Reson. Med.*, vol. 51, no. 4, pp. 744-752, 2004.
- [145] D. Kim, W. D. Gilson, C. M. Kramer, and F. H. Epstein, "Myocardial Tissue Tracking with Two-Dimensional Cine Displacement-Encoded MR Imaging: Development and Initial Evaluation," *Radiology*, vol. 230, pp. 862-871, 2004.
- [146] X. Zhong, J. Cai, D. Schlesinger, J. Sheehan, J. Larner *et al.*, "Motion Tracking of Brain and Spinal Cord Using Cine DENSE MRI," *International Journal of Radiation Oncology Biology Physics*, vol. 69, no. 3, Supplement 1, pp. S240-S241, 2007.

- [147] F. H. Epstein, and W. D. Gilson, "Displacement-Encoded Cardiac MRI Using Cosine and Sine Modulation to Eliminate (CANSEL) Artifact-Generating Echoes," *Magn. Reson. Med.*, vol. 52, no. 4, pp. 774-781, 2004.
- [148] J. F. Canny, "A Computational Approach to Edge Detection," *IEEE Trans. on Pattern Analysis and Machine Intelligence*, vol. 8, no. 6, pp. 679-698, November, 1986.
- [149] D. Marr, and E. C. Hildreth, "Theory of Edge Detection," *Proc. Roy. Soc. London*, vol. B-207, pp. 187-217, 1980.
- [150] E. C. Hildreth, "Computations Underlying the Measurement of Visual Motion," *Artificial Intelligence*, vol. 23, pp. 309-354, 1984.
- [151] B. F. Buxton, and H. Buxton, *Low Level Edge Detection for The Extraction of Optical Flow Data and Passive Ranging*, Technical Report 3, Wembley, 1983.
- [152] B. F. Buxton, and H. Buxton, "Monocular Depth Perception from Optical Flow by Space Time Signal Processing." *Proceedings of the Royal Society of London. Series B, Biological Sciences*, vol. 218, no. 1210, pp. 27-47, 1983.
- [153] B. F. Buxton, H. Buxton, D. W. Murray, and N. S. Williams, "Machine Perception of Visual Motion," *Technical Report 3*, Wembley, 1985.
- [154] S. Gong, and M. Brady, "Parallel computation of Optic Flow," in *Proc. 1st European Conf. on Computer Vision*, pp. 124-133, 1990.
- [155] S. M. Smith, "Feature Based Image Sequence Understanding," Ph.D. Dissertation, Robotics Research Group, Oxford University, 1992.

- [156] R. C. Bolles, H. H. Baker, and D. H. Marimont, "Epipolar Plane Image Analysis: An Approach to Determining Structure from Motion," *Int. Journal of Computer Vision*, vol. 1, pp. 7-55, 1987.
- [157] A. Blake, and R. Cipolla, "Robust Estimation of Surface Curvature from Deformation of Apparent Contours," *Image and Vision Computing*, vol. 9, no. 2, pp. 107-112, 1991.
- [158] H. H. Chen, and T. S. Huang, "Matching 3-D Line Segments with Applications to Multiple-Object Motion Estimation," *IEEE Trans. on Pattern Analysis and Machine Intelligence*, vol. 12, no. 10, pp. 1002-1008, October, 1990.
- [159] R. Deriche, and O. Faugeras, "Tracking Line Segments," in *Proc. 1st European Conf. on Computer Vision*, pp. 259-268, 1990.
- [160] O. D. Faugeras, "On the Motion of 3-D Curves and Its Relationship to Optical Flow," in *Proc. 1st European Conf. on Computer Vision*, pp. 107-117, 1990.
- [161] G. Sandini, and M. Tistarelli, "Active Tracking Strategy for Monocular Depth Inference over Multiple Frames," *IEEE Trans. on Pattern Analysis and Machine Intelligence*, vol. 12, no. 1, January, 1990.
- [162] C. Tomasi, and T. Kanade, "Shape and Motion without Depth," in *Proc. Image Understanding Workshop*, 1990.
- [163] B. K. P. Horn, and B. G. Shunck, "Determining Optical Flow," *Artificial Intelligence*, vol. 17, pp. 185-203, 1981.
- [164] S. S. Beauchemin, and J. L. Barron, "The Computation of Optical Flow," *ACM Computing Surveys*, vol. 27, no. 3, pp. 433-467, September, 1995.

- [165] S. Ullman, *The Interpretation of Visual Motion*, Cambridge, MA: MIT Press, 1979.
- [166] G. Aubert, R. Deriche, and P. Kornprobst, "Computing optical flow via variational techniques," *SIAM Journal on Applied Mathematics*, vol. 60, no. 1, pp. 156-182, December 21, 1999.
- [167] M. Mesbah, "Gradient-Based Optical Flow : A Critical Review," in *Fifth International Symposium on Signal Processing and its Applications*, pp. 467-470, 1999.
- [168] G. Adiv, "Determining Three-Dimensional Motion and Structure from Optical Flow Generated by Several Moving Objects," *IEEE Trans. on Pattern Analysis and Machine Intelligence*, vol. PAMI-7, no. 4, pp. 384-401, July, 1985.
- [169] B. G. Schunck, "Image Flow Segmentation and Estimation by Constraint Line Clustering," *IEEE PAMI 11*, vol. 10, pp. 1010-1027, 1989.
- [170] H.-H. Nagel, "On a Constraint Equation for the Estimation of Displacement Rates in Image Sequences," *IEEE PAMI 11*, vol. 1, pp. 13-30, 1989.
- [171] S. Negahdaiupour, and C. H. Yu, "A Generalized Brightness Change Model for Computing Optical Flow," in *Proceedings ICCV*, pp. 2-11, 1993.
- [172] J. L. Prince, and E. R. McVeigh, "Motion Estimation from Tagged MR Image Sequences," *IEEE Trans. on Medical Images*, vol. 11, no. 2, pp. 238-249, 1992.
- [173] N. Mukawa, "Estimation of Shape, Reflection Coefficients and Illuminant Direction from Image Sequences," in *Proceedings of ICCV*, pp. 507-512, 1990.

- [174] N. Vasconcelos, and A. Lippman, "Spatiotemporal Model-Based Optical Flow Estimation." pp. 2201-2204.
- [175] B. D. Lucas, "Generalized Image Matching by the Method of Differences", Ph.D. Dissertation, UMI Order Number: AAI8601180., Carnegie Mellon University 1985.
- [176] B. D. Lucas, and T. Kanade, "An Iterative Image-Registration Technique with an Application to Stereo Vision," in *Proceedings of IJCAI*, pp. 674-679, 1981.
- [177] E. P. Simoncelli, E. H. Adelson, and D. J. Heeger, "Probability Distributions of Optical Flow," in *IEEE Proceedings of C'VPR*, pp. 310-315, 1991.
- [178] C. H. Chu, and E. J. Delp, "Estimating Displacement Vectors from an Image Sequence," *J. Opt. Sm. Am.*, vol. A 6, no. 6, pp. 871-878, 1989.
- [179] J. Weber, and J. Malik, "Robust Computation of Optical Flow in a Multi-Scale Differential Framework," in *Proceedings of ICCV*, pp. 12-20, 1993.
- [180] M. Campani, and A. Verri, "Computing Optical Flow from an Overconstrained System of Linear Equations," in *Proceedings of ICCV*, pp. 22-26, 1990.
- [181] R. M. Haralick, and J. S. Lee, "The Facet Approach to Optic Flow," in *DARPA Proceedings of Image Understanding Workshop*, pp. 84-93, 1982.
- [182] H.-H. Nagel, "On the Estimation of Optical Flow: Relations Between Different Approaches and Some New Results," *Artificial Intelligence*, vol. 33, pp. 299-324, 1987.
- [183] H.-H. Nagel, "Constraints for the Estimation of Vector Fields from Image Sequences," in *Proceedings IJCAI*, pp. 945-951, 1983.

- [184] S. Uras, F. Girosi, A. Verri, and V. Torre, "A Computational Approach to Motion Perception," *Biol. Cybern.*, vol. 60, pp. 79–87, 1988.
- [185] O. Tretiak, and L. Pastor, "Velocity Estimation from Image Sequences with Second-Order Differential Operators," in *IEEE Proceedings of ICPR*, pp. 20-22, 1984.
- [186] N. Gupta, S. Raghavan, and L. Kanal, "Robust Recovery of Image Motion," in *Proceedings of Asian Conference on Computer Vision*, pp. 244-247, 1993
- [187] H. Liu, T.-H. Hong, and M. Herman, "A General Motion Model and Spatio-Temporal Filters for Computing Optical Flow," *Int. J. Comput. Vision*, vol. 22, no. 2, pp. 147-172, 1997.
- [188] M. Otte, and H.-H. Nagel, "Estimation of Optical Flow Based on Higher-Order Spatiotemporal Derivatives in Interlaced And Non-Interlaced Image Sequences," *Artificial Intelligence*, vol. 78, pp. 5-43, 1995.
- [189] N. M. Namazi, P. Panafiel, and C. M. Fan, "Nonuniform Image Motion Estimation Using Kalman Filtering," *IEEE Trans. on Image Processing*, vol. 1, no. 5, pp. 678-683, 1994.
- [190] J. Kim, and J. W. Woods, "3-D Kalman Filter for Image Motion Estimation," *IEEE Trans. on Image Processing*, vol. 7, no. 1, pp. 42-52, 1998.
- [191] J. A. Yang, and X. M. Yang, "Robust, Real-Time Motion Estimation from Long Image Sequences Using Kalman Filtering," in *Proceedings of the First IEEE international Workshop on Biologically Motivated Computer Vision*, S. Lee, H.

- H. Bülthoff, and T. Poggio, Eds. Lecture Notes In Computer Science, vol. 1811, London: Springer-Verlag, pp. 602-612, 2000.
- [192] O. Michailovich, and A. Tannenbaum, "A Method for Prediction and Estimation of Large-Amplitude Optical Flows via Extended Kalman Filtering Approach," *Engineering Computations: International Journal for Computer-Aided Engineering and Software*, vol. 23, no. 5, pp. 503-514, 2006.
- [193] H. Liu, and P. Shi, "State-Space Analysis of Cardiac Motion with Biomechanical Constraints," *IEEE Trans. On Image Processing*, vol. 16, no. 4, pp. 901-917, 2007.
- [194] S. Tong, and P. Shi, "Cardiac Motion Recovery: Continuous Dynamics, Discrete Measurements, and Optimal Estimation", *MICCAI 2006*, Lecture Notes In Computer Science, Berlin: Springer-Verlag, vol. 4190, pp. 744-751, 2006.
- [195] M. Shah, K. Rangarajan, and P.-S. Tsai, "Motion Trajectories," *IEEE Trans. on Systems, Man, and Cybernetics*, vol. 23, no. 4, pp. 1138-1150, 1993.
- [196] S. J. Julier, and J. J. La Viola, "On Kalman Filtering with Nonlinear Equality Constraints," *IEEE Trans. On Signal Processing*, vol. 55, no. 6, pp. 2774-2783, 2007.
- [197] P.-C. Liu, and W.-T. Chang, "Recursive Wiener Filter for Motion Parameter Estimation in Three-Parameter Motion Model," *IEEE Trans. on Circuits and Systems for Video Technology*, vol. 8, no. 8, pp. 1001-1014, 1998.

- [198] J. K. Kearney, W. B. Thompson, and D. Boley, "Optical Flow Estimation: An Error Analysis of Gradient-Based Methods with Local Optimization," in *IEEE PAMI* 9, pp. 229-244, 1987.
- [199] F. C. Glazer, "Computation of Optical Flow by Multilevel Relaxation," *Tech. Rep. COINSTR-TR-87-64*, 1987.
- [200] F. C. Glazer, "Hierarchical Gradient-Based Motion Detection," in *DARPA Proceedings of Image Understanding Workshop*, pp. 733-748, 1987.
- [201] P. Anandan, "A Computational Framework and an Algorithm for the Measurement of Visual Motion," *Int. J. Comput. Vision*, vol. 2, pp. 283-310, 1989.
- [202] D. J. Heeger, "Optical Flow Using Spatiotemporal Filters," *Int. J. Comput. Vision*, vol. 1, pp. 279-302, 1988.
- [203] J. R. Bergen, P. Anandan, K. Hanna, and R. Hingorani, "Hierarchical Model-Based Motion Estimation," in *Proceedings of ECCV*, pp. 237-252, 1992.
- [204] T. J. Burns, S. K. Rogers, D. W. Ruck, and M. E. Oxley, "Discrete, Spatiotemporal, Wavelet Multiresolution Analysis Method for Computing Optical Flow," *Optical Engineering*, vol. 33, no. 7, pp. 2236-2247, 1994.
- [205] A. B. Watson, and A. J. Ahumada, Jr, "Model of Human Visual-Motion Sensing," *J. Opt. Soc. Am.*, vol. A/Vol. 2, no. No. 2, pp. 322-342, February, 1985.
- [206] D. J. Fleet, and A. D. Jepson, "Computation of Component Image Velocity from Local Phase Information," *Int. J. Comput. Vision*, vol. 5, no. 1, pp. 77-104, 1990.

- [207] N. M. Grzywacz, and A. L. Yuille, "A Model for the Estimate of Local Velocity by Cells in the Visual Cortex," in *Proc. Royal Society London*, pp. 129-161, 1990.
- [208] J. L. Barron, D. J. Fleet, and S. S. Beauchemin, "Performance of Optic Flow Techniques," *Int. J. Comput. Vision*, vol. 12, no. 1, pp. 43-77, 1994.
- [209] J. J. Little, "Accurate Early Detection of Discontinuities," in *Vision Interface*, pp. 2-7, 1992.
- [210] I. Grant, "Particle Image Velocimetry: A Review," *Proc Instn Mech Engrs*, vol. 211, no. C, pp. 55-76, 1997.
- [211] S.-J. Lee, and G. B. Kim, "Synchrotron Microimaging Technique for Measuring the Velocity Fields of Real Blood Flows," *Journal of Applied Physics*, vol. 97, no. 064701, pp. 1-6, 2005.
- [212] R. J. Adrian, "Particle-Imaging Techniques for Experimental Fluid Mechanics," *Annual Review of Fluid Mechanics*, vol. 23, pp. 261-304, 1991.
- [213] D. W. Robinson, "Automatic Fringe Analysis with a Computer Image-Processing System," *Appl. Optics*, vol. 22, no. 14, pp. 2169-2176, 1983.
- [214] J. W. Goodman, *Introduction to Fourier Optics*, New York: McGraw-Hill, 1968.
- [215] C.-S. Yao, and R. J. Adrian, "Orthogonal Compression and 1-D Analysis Technique for Measurement of 2-D Particle Displacement in Pulsed Laser Velocimetry," *Appl. Optics*, vol. 23, pp. 1687-1689, 1984.
- [216] R. J. Adrian, "Statistical Properties of Particle Image Velocimetry Measurements in Turbulent Flow," *Laser Anemometry in Fluid Mechanics*, R. J. Adrian, D. F.

- G. Durao, F. Durst *et al.*, Eds., pp. 115-129, Lisbon: Lodoan-Instituto Superior Tecnico, 1988.
- [217] C. D. Meinhart, S. T. Wereley, and J. G. Santiago, "A PIV Algorithm for Estimating Time-Averaged Velocity Fields," *Journal of Fluids Engineering*, vol. 122, pp. 285-289, 2000.
- [218] J. Coupland, and N. A. Halliwell, "Particle Image Velocimetry: Rapid Transparency Analysis Using Optical Correlation," *Appl. Optics*, vol. 27, no. 10, pp. 1919-1921, 1988.
- [219] G. Gheen, and L.-J. Chen, "Optical Correlators with Fast Updating Speed Using Photorefractive Semiconductor Materials," *Appl. Optics*, vol. 27, no. 13, pp. 2756-2761, 1988.
- [220] Z. Q. Mao, N. A. Halliwell, and J. Coupland, "Particle Image Velocimetry: High Speed Transparency Scanning and Correlation-Peak Location in Optical Processing Systems," *Appl. Optics*, vol. 32, no. 26, pp. 5089-5091, 1993.
- [221] R. Meynart, "Equal Velocity Fringes in a Rayleigh-Bernard Flow by Speckle Method," *Appl. Optics*, vol. 19, pp. 1385-1386, 1980.
- [222] V. Palero, N. Andres, M. P. Arroya, and M. Quintanilla, "Fast Quantitative Processing of Particle Image Velocimetry Photographs by A Whole-Field Filtering Technique," *Experiments in Fluids*, vol. 19, no. 6, pp. 417-425, 1995.
- [223] J. Westerweel, "Digital Particle Image Velocimetry - Theory and Application," Ph.D. Dissertation, Delft University, Delft, 1993.

- [224] C. E. Willert, and M. Gharib, "Digital Particle Image Velocimetry," *Experiments in Fluids*, vol. 10, pp. 181-193, 1991.
- [225] W. Merzkirch, T. Mrosewski, and H. Wintrich, "Digital Particle Image Velocimetry Applied to A Natural Convective Flow," *Acta Mechanica*, vol. 4 (Suppl. 1), pp. 19-26, 1994.
- [226] J. Westerweel, "Fundamentals of Digital Particle Image Velocimetry," *Meas. Sci. Technol.*, vol. 8, no. 12, pp. 1379-1392, 1997.
- [227] Y. C. Cho, "Digital Image Velocimetry," *Appl. Optics*, vol. 28, pp. 740-748, 1989.
- [228] R. D. Kean, and R. J. Adrian, "Theory of Cross-Correlation Analysis of PIV Images," *App. Sci. Res.*, vol. 49, pp. 191-215, 1992.
- [229] N. J. Lawson, N. A. Halliwell, and J. M. Coupland, "Particle Image Velocimetry: Image Labelling by Use of Adaptive Optics to Modify the Point-Spread Function," *Appl. Optics*, vol. 33, no. 19, pp. 4241-4247, 1994.
- [230] H. Huang, D. Dabiri, and M. Gharib, "On Errors of Digital Particle Image Velocimetry," *Meas. Sci. Technol.*, vol. 8, no. 12, pp. 1427-1440, 1997.
- [231] R. Theunissen, F. Scarano, and M. L. Riethmuller, "An Adaptive Sampling and Windowing Interrogation Method in PIV," *Meas. Sci. Technol.*, vol. 18, pp. 275-287, 2007.
- [232] K. A. Chang, and P. L. F. Liu, "Velocity, Acceleration and Vorticity Under a Breaking Wave," *Phys. Fluids*, vol. 10, no. 1, pp. 327-329, Jan 1998, 1998.

- [233] G. Sridhar, and J. Katz, "Drag and Lift Forces on Microscopic Bubbles Entrained by a Vortex," *Phys. Fluids*, vol. 7, no. 2, pp. 389-399, 1995.
- [234] S. Chu, R. Dong, and J. Katz, "Relationship Between Unsteady Flow, Pressure Fluctuations, and Noise in a Centrifugal Pump - Part A: Use of PDV Data to Compute the Pressure Field," *Trans. ASME*, vol. 117, no. 24-29, 1995.
- [235] M. L. Jakobsen, T. P. Dewhurst, and C. A. Greated, "Particle Image Velocimetry for Predictions of Acceleration Fields and Force Within Fluid Flows," *Meas. Sci. Technol.*, vol. 8, no. 12, pp. 1502-1516, Dec 1997, 1997.
- [236] X. Liu, and J. Katz, "Instantaneous Pressure And Material Acceleration Measurements Using a Four-Exposure PIV," *Experiments in Fluids*, vol. 41, no. 2, pp. 227-240, August 2006, 2006.
- [237] T. A. Kowalewski, "Particle Image Velocimetry and Thermometry for Two-Phase Flow Problems," *Annals New York Academy Of Sciences*, vol. 972, pp. 213-222, 2002.
- [238] H. Hirahara, M. Z. Hossain, M. Kawahashi, and Y. Nonomura, "Testing Basic Performance of a Very Small Wind Turbine Designed for Multi-Purposes," *Renewable Energy*, vol. 30, no. 8, pp. 1279-1297, 2005.
- [239] C. Fureby, F. F. Grinstein, G. Li, and E. J. Gutmark, "An Experimental and Computational Study of A Multi-Swirl Gas Turbine Combustor," in *Proceedings of The Combustion Institute*, vol. 31, no. 2, pp. 3107-3114, 2007.
- [240] A. R. Khopkar, J. Aubin, C. Xuereb, N. Le Sauze, J. Bertrand *et al.*, "Gas-Liquid Flow Generated by A Pitched-Blade Turbine: Particle Image Velocimetry

- Measurements and Computational Fluid Dynamics Simulations,” *Industrial & Engineering Chemistry Research*, vol. 42, no. 21, pp. 5318-5322, 2003.
- [241] D. F. Hill, K. V. Sharp, and R. J. Adrian, “Stereoscopic Particle Image Velocimetry Measurements of the Flow Around a Rushton Turbine,” *Experiments in Fluids*, vol. 29, no. 5, pp. 478-485, 2000.
- [242] B. Patte-Rouland, G. Lalizel, J. Moreau, and E. Rouland, “Flow Analysis of an Annular Jet by Particle Image Velocimetry and Proper Orthogonal Decomposition,” *Meas. Sci. Technol.*, vol. 12, pp. 1404-1412, 2001.
- [243] H. Hu, T. Saga, T. Kobayashi, N. Taniguchi and M. Yasuki, “Dual-Plane Stereoscopic Particle Image Velocimetry: System Set-Up and Its Application on a Lobed Jet Mixing Flow,” *Experiments in Fluids*, vol. 31, pp. 277-293, 2001.
- [244] A. Nahum, and A. Seifert, “On the Application of Confined Twin-Jet Instability to Micro-Mixing Enhancement,” *Phys. Fluids*, vol. 18, no. 6, pp. (064107) 1-14, 2006.
- [245] H. Hu, T. Saga, T. Kobayashi, and N. Taniguchi, “Simultaneous Velocity and Concentration Measurements of a Turbulent Jet Mixing Flow,” *Visualization And Imaging in Transport Phenomena*, vol. 972, pp. 254-259, 2002.
- [246] E. B. Arik, and J. Carr, "Digital Particle Image Velocimetry for Real-Time Wind Tunnel Measurements," in *International Congress on Instrumentation in Aerospace Simulation Facilities*, pp. 267-277, 1997.

- [247] M. V. Ol, and M. Gharib, "Leading-Edge Vortex Structure of Nonslender Delta Wings at Low Reynolds Number," *American Institute of Aeronautics and Astronautics*, vol. 41, no. 1, pp. 16-26, 2003.
- [248] C. Willert, M. Raffel, J. Kompenhans, B. Stasicki and C. Kahler, "Recent Applications of Particle Image Velocimetry in Aerodynamic Research," *Flow Measurement and Instrumentation*, vol. 7, no. 3-4, pp. 247-256, 1996.
- [249] J. G. Santiago, S. T. Wereley, C. D. Meinhart, D. J. Beebe and R. J. Adrian, "A Particle Image Velocimetry System for Microfluidics," *Experiments in Fluids*, vol. 25, no. 4, pp. 316-319, 1998.
- [250] C. D. Meinhart, S. T. Wereley, and J. G. Santiago, "PIV Measurements of A Microchannel Flow," *Experiments in Fluids*, vol. 27, pp. 414-419, 1999.
- [251] C. D. Meinhart, S. T. Wereley, and M. H. B. Gray, "Volume Illumination for Two-Dimensional Particle Image Velocimetry," *Meas. Sci. Technol.*, vol. 11, pp. 809-814, 2000.
- [252] S. Devasenathipathy, J. G. Santiago, S. T. Wereley , C. D. Meinhart and K. Takehara, "Particle Imaging Techniques for Microfabricated Fluidic Systems," *Experiments in Fluids*, vol. 34, pp. 504-514, 2003.
- [253] S. Devasenathipathy, and J. G. Santiago, "Particle Tracking Techniques for Electrokinetic Microchannel Flows," *Anal. Chem.*, vol. 74, pp. 3704-3713, 2002.
- [254] T. Bayraktar, and S. B. Pidugu, "Characterization of Liquid Flows in Microfluidic Systems," *International Journal of Heat and Mass Transfer*, vol. 49, pp. 815-824, 2006.

- [255] D. Sinton, "Microscale Flow Visualization," *Microfluid Nanofluid*, vol. 1, pp. 2–21, 2004.
- [256] N.-T. Nguyen, and Z. Wu, "Micromixers—Z Review," *J. Micromech. Microeng.*, vol. 15, pp. R1–R16, 2005.
- [257] K. Shinohara, Y. Sugii, A. Aota, A. Hibara, M. Tokeshi *et al.*, "High-Speed Micro-PIV Measurements of Transient Flow in Microfluidic Devices," *Meas. Sci. Technol.*, vol. 15, pp. 1965–1970, 2004.
- [258] M. R. Bown, J. M. MacInnes, and R. W. K. Allen, "Micro-PIV Simulation and Measurement in Complex Microchannel Geometries," *Meas. Sci. Technol.*, vol. 16, pp. 619-626, 2005.
- [259] C. D. Meinhart, and H. Zhang, "The Flow Structure Inside A Microfabricated Inkjet Printhead," *Journal of Microelectromechanical Systems*, vol. 9, no. 1, pp. 67-75, 2000.
- [260] M. J. Kim, and K. D. Kihm, "Microscopic PIV Measurements for Electro-osmotic Flows in PDMS Microchannels," *Journal of Visualization*, vol. 7, pp. 111-118, 2004.
- [261] A. D. Stroock, S. K. W. Dertinger, A. Ajdari, I. Mezi, H. A. Stone *et al.*, "Chaotic Mixer for Microchannels," *Science*, vol. 295, pp. 647-651, 2002.
- [262] Y. Sugii, S. Nishio, and K. Okamoto, "Measurement of A Velocity Field in Microvessels Using A High Resolution PIV Technique," *Annals New York Academy Of Sciences*, vol. 972, no. 331-336, 2002.

- [263] I. Grant, S. Fu, X. Pan, and X. Wang, "The Application of An In-Line, Stereoscopic, PIV system to 3-Component Velocity Measurements," *Experiments in Fluids*, vol. 19, pp. 214-221, 1995.
- [264] Y. G. Guezennec, Y. Zhao, and T. J. Gieseke, "High-Speed 3D Scanning Particle Image Velocimetry (3D SPIV) Technique," *Developments in Laser Techniques and Applications to Fluid Mechanics*. Adrian RJ et al, Eds., Lisbon: Proceedings of the 7th international symposium, pp 11–14, 1994.
- [265] T. Hori, and J. Sakakibara, "High-Speed Scanning Stereoscopic PIV for 3D Vorticity Measurement in Liquids," *Meas. Sci. Technol.*, vol. 15, pp. 1067-1078, 2004.
- [266] E. J. Foeth, C. W. H. van Doorne, T. van Terwisga, and B. Wieneke, "Time Resolved PIV and Flow Visualization of 3D Sheet Cavitation," *Experiments in Fluids*, vol. 40, pp. 503-513, 2006.
- [267] S. Y. Yoon, and K. C. Kim, "3D Particle Position and 3D Velocity Field Measurement in a Microvolume via the Defocusing Concept," *Meas. Sci. Technol.*, vol. 17, pp. 2897-2905, 2006.
- [268] J. L. Blackshire, W. M. Humphreys, and S. M. Bartram, "3-Dimensional, 3-Component Velocity Measurements Using Holographic Particle Image Velocimetry (HPIV)," in *Eighteenth AIAA Aerospace Ground Testing Conference*, pp. 94-2645, 1994.

- [269] D. H. Barnhart, R. J. Adrian, and G. C. Papen, "Phase-Conjugate Holographic System for High-Resolution Particle Image Velocimetry," *Appl. Optics*, vol. 33, no. 30, pp. 7159-7170, 1994.
- [270] J. M. Coupland, and N. A. Halliwell, "Particle Image Velocimetry: Three Dimensional Fluid Velocity Measurements Using Holographic Recording and Optical Correlation," *Appl. Optics*, vol. 31, no. 1005-1007, 1992.
- [271] J. Zhang, and J. Katz, "Three Dimensional Velocity Measurements Using Hybrid HPIV," in *Proceedings of Eighth International Symposium on Application of Laser Techniques to Fluid Mechanics*, p. 4.3, 1996.
- [272] B. Skarman, J. Berkert, and K. Wozniak, "Simultaneous 3D-PIV and Temperature Measurements Using a New CCD-Based Holographic Interferometer," *Flow Measurement and Instrumentation*, vol. 7, no. 1, pp. 1-6, 1996.
- [273] R. Di Leonardo, J. Leach, H. Mushfique, J. M. Cooper, G. Ruocco *et al.*, "Multipoint Holographic Optical Velocimetry in Microfluidic Systems," *Physical Review Letters*, vol. 96, no. 134502, pp. 1-4, 2006.
- [274] M. Raffel, M. Gharib, O. Ronnenberger, and J. Kompenhans, "Feasibility Study of Three-Dimensional PIV by Correlating Images of Particles Within Parallel Light Sheet Planes," *Experiments in Fluids*, vol. 19, pp. 69-77, 1995.
- [275] R. Lima, S. Wada, K. Tsubota, and T. Yamaguchi, "Confocal Micro-PIV Measurements of Three-Dimensional Profiles of Cell Suspension Flow in a Square Microchannel," *Meas. Sci. Technol.*, vol. 17, pp. 797-808, 2006.

- [276] J. Park, C. Choi, and K. Kihm, "Optically Sliced Micro-PIV Using Confocal Laser Scanning Microscopy (CLSM)," *Experiments in Fluids*, vol. 37, pp. 105-119, 2004.
- [277] J. Stefanini, G. Cognet, J. C. Vila, B. Merite and Y. A. Brenier, "A Coloured Method for PIV Technique," in *Flow Visualisation and Image Analysis*, 1993, pp. 247-258.
- [278] A. Cenedese, and G. P. Romano, "Comparison between Classical and Three-Colour PIV in a Wake Flow," *J. Flow Visualisation and Image Processing*, vol. 1, pp. 371-384, 1993.
- [279] T. G. Kang, and T. H. Kwon, "Colored Particle Tracking Method for Mixing Analysis of Chaotic Micromixers," *J. Micromech. Microeng.*, vol. 14, pp. 891-899, 2004.
- [280] I. Grant, Y. Zhao, Y. Tan, and J. N. Stewart, "Three Component Flow Mapping: Experiences in Stereoscopic PIV and Holographic Velocimetry," in *Proceedings of Fourth International Conference on Laser Anemometry, Advances and Applications*, pp. 365-371, 1991.
- [281] E. P. Fabry, "3D Holographic PIV with a Forward-Scattering Laser Sheet and Stereoscopic Analysis," *Experiments in Fluids*, vol. 24, pp. 39-46, 1998.
- [282] M. Marassi, P. Castellini, M. Pinotti, and L. Scalise, "Cardiac Valve Prosthesis Flow Performances Measured by 2D and 3D-Stereo Particle Image Velocimetry," *Experiments in Fluids*, vol. 36, pp. 176-186, 2004.

- [283] H. Klank, G. Goranovic, J. P. Kutter, H. Gjelstrup, J. Michelsen *et al.*, "PIV Measurements in a Microfluidic 3D-Sheathing Structure with Three-Dimensional Flow Behaviour," *J. Micromech. Microeng.*, vol. 12, pp. 862-869, 2002.
- [284] Z.-P. Liang, and P. C. Lauterbur, *Principles of Magnetic Resonance Imaging: A Signal Processing Perspective*, Piscataway, NJ: IEEE Press Series in Biomedical Engineering, 1999.
- [285] J. A. Bankson, M. A. Griswold, S. M. Wright, and D. K. Sodickson, "SMASH Imaging with an Eight Element Multiplexed RF Coil Array," *MAGMA*, vol. 10, pp. 93–104, 2000.
- [286] M. Blaimer, J. Ji, M. McDougall, M. Griswold and S. Wright, "Improving Image Quality for Single Echo Acquisitions (SEA): Introducing Two Novel Approaches," in *Proc. of 15th ISMRM/ESMRMB*, p. 3342, 2007.
- [287] N. J. Pelc, "Flow quantification and Analysis Methods," *Magn Reson Imaging Clin North Am*, vol. 3, no. 3, pp. 413-424, 1995.
- [288] E. X. Wu, C. W. Towe, and H. Tang, "MRI Cardiac Tagging Using a Sinc-Modulated RF Pulse Train," *Magnetic Resonance in Medicine*, vol. 48, pp. 389-93, 2002.
- [289] E. Waks, J. L. Prince, and A. S. Douglas, "Cardiac Motion Simulator for Tagged MRI," in *Proc. Workshop Mathematical Methods in Medical Image Analysis*, pp. 182–191, 1996.

- [290] T. Okuno, Y. Sugii, and S. Nishio, "Image Measurement of Flow Field Using Physics-Based Dynamic Model," *Meas. Sci. Technol.*, vol. 11, pp. 667–676, 2000.
- [291] H. G. Hinghofer-Szalkay, and J. E. Greenleaf, "Continuous Monitoring of Blood Volume Changes in Humans," *Journal of Applied Physiology*, vol. 63, pp. 1003-1007, 1987.
- [292] J. Stoitsis, E. Bastouni, D. C. Karampinos, J. C. Bosshard, J. Lu *et al.*, "Velocity Extraction from Spin-Tagging MRI Images Using a Weighted Least-Squares Optical Flow Method," in *IEEE International Workshop on Imaging Systems and Techniques*, pp. 1 - 5, 2007.
- [293] S. Tsushima, A. Hasegawa, T. Suekane, S. Hirai, Y. Tanaka *et al.*, "Velocity Measurement of Clay Intrusion through a Sudden Contraction Step Using a Tagging Pulse Sequence," *Magnetic Resonance Imaging*, vol. 21, no. 6, pp. 673-677, 2003.
- [294] K. W. Moser, L. G. Raguin, and J. G. Georgiadis, "Synchronized EPI Phase Contrast Velocimetry in a Mixing Reactor," *Magnetic Resonance Imaging*, vol. 21, pp. 127–133, 2003.
- [295] Y. Jiraraksopakun, S. M. Wright, and J. X. Ji, "Analyzing Rapid Flow from SEA-Tagged MR Images Using Harmonic Phase (HARP)," in *Joint Annual Meeting ISMRM-ESMRMB*, Berlin, Germany., 19-25 May 2007.
- [296] Y. Jiraraksopakun, S. M. Wright, M. P. McDougall, and J. X. Ji, "A Regularized Quantification Method for Rapid Flow Tagging MRI Imaging Using Single-Echo

- Acquisition," in *IEEE EMBC'08 30th Annual International Conference of the IEEE Engineering in Medicine and Biology Society*, 2008
- [297] H. D. Kitajima, K. S. Sundareswaran, T. Z. Teisseyre, G. W. Astary, W. J. Parks *et al.*, "Comparison of Particle Image Velocimetry and Phase Contrast MRI in a Patient-Specific Extracardiac Total Cavopulmonary Connection," *Journal of Biomechanical Engineering*, vol. 130, no. 4, pp. 041004 (14), August 2008.
- [298] D. P. J. Barz, H. F. Zadeh, and P. Ehrhard, "Measurements and Simulations of the Flow Field in an Electrically Excited Meander Micromixer," *Particle Image Velocimetry: New Developments And Recent Applications*, Topics In Applied Physics, pp. 1-18, 2008.
- [299] F. Bottausci, C. Cardonne, C. Meinhart, and I. Mezic, "An Ultrashort Mixing Length Micromixer: The Shear Superposition Micromixer," *Lab on a Chip*, vol. 7, no. 3, pp. 396-398, 2007.
- [300] J. K. Sveen, "An Introduction to MatPIV v.1.6.1," *Mechanics and Applied Mathematics: Eprint Series*, Dept. of Math. University of Oslo, 2004.
- [301] P. E. Gill, W. Murray, and M. H. Wright, "Practical Optimization," London: Academic Press, 1981.
- [302] S. P. Han, "A Globally Convergent Method for Nonlinear Programming," *Journal of Optimization Theory and Applications*, vol. 22, pp. 297, 1977.
- [303] M. J. D. Powell, "A Fast Algorithm for Nonlinearly Constrained Optimization Calculations," *Numerical Analysis*, G. A. Watson, Ed. Berlin: Lecture Notes in Mathematics, Springer Verlag, vol. 630, pp. 144-157, 1978.

- [304] M. J. D. Powell, "The Convergence of Variable Metric Methods for Nonlinearly Constrained Optimization Calculations," *Nonlinear Programming 3*, O. L. Mangasarian, R. R. Meyer and S. M. Robinson, Eds. New York: Academic Press, pp. 27-63, 1978.

VITA

Yuttapong Jiraraksopakun received the B.E. degree in Electrical Engineering from Chulalongkorn University in 2000, M.Eng. degree in Electrical and Computer Engineering from Texas A&M University in 2004. He graduated with Ph.D. degree in Electrical and Computer Engineering at Texas A&M University in May 2009.

From 2000 to 2002, he worked as a system programmer to develop Windows-based banking systems for Bangkok Bank Public Co, Ltd. In 2002, he received a Royal Thai Scholarship from Thailand to study M.S. – Ph.D. in Electrical Engineering. In 2004, he joined the Magnetic Resonance System Laboratory in the Biomedical Imaging and Genomic Signal Processing group. He has been involved with research of imaging processing for image registration, pharmacokinetic analysis, and motion quantification. His current research interests include image-based flow quantification, image registration algorithms, and optimization problems for image processing.

Mr. Jiraraksopakun may be reached at 3128 TAMU, Department of Electrical and Computer Engineering, College Station, TX, 77843-3128. His email is yuttapong@tamu.edu.